MESHLESS MODELING OF SUBMARINE LANDSLIDE GENERATED FULLY NONLINEAR WAVES AND RUNUP

by

Burhan Turgut Özbar

B.S., Civil Engineering, Boğaziçi University, 2016

Submitted to the Institute for Graduate Studies in
Science and Engineering in partial fulfillment of
the requirements for the degree of
Master of Science

Graduate Program in Civil Engineering

Boğaziçi University

2019

ACKNOWLEDGEMENTS

First of all, I would like to express my immense gratitude to my thesis supervisor Assoc. Prof. Osman S. Börekçi for his persistent help and guidance. He was always there whenever I ran into a trouble spot or had a question about my model or writing.

I would like to thank Assoc. Prof. Emre Otay for his valuable comments on this thesis. I would also like to acknowledge Yavuz Tokmak, Ph.D. as the reader of this thesis.

Finally, I want to express my very deep gratitude to my family for their unfailing support and continuous encouragement throughout my years of study and through the process of researching and writing this thesis.

ABSTRACT

MESHLESS MODELING OF SUBMARINE LANDSLIDE GENERATED FULLY NONLINEAR WAVES AND RUNUP

A two-dimensional numerical model based on fully nonlinear potential flow theory is proposed for the simulation of tsunamis generated by earthquakes and submarine landslides. The boundary value problem of the theory is numerically solved using the method of fundamental solutions which is a boundary only method. Thus, the model can cope with large domains which are required for the modeling of the long distance propagation of tsunamis. Because of the singular nature of the fundamental solution, the approximating functions are defined on the fictitious boundaries located parallel to the physical boundaries. The positions of the fictitious boundaries are updated at each time level to avoid any numerical instability that may be caused by the closeness of the physical and the fictitious boundaries. The tsunami generation mechanism in the model is based on bottom deformation whose motion can be described by a water depth function or by a time dependent velocity field with the initial geometric properties of bottom. Time dependent deformations both on the bottom and on the free surface are easily implemented in the model thanks to the meshless feature of the method. Using the full-Lagrangian description of the deforming free surface, the run-up and the run-down of waves can be accurately modeled by the model without any additional technique. Moreover, three different tsunami generation benchmark problems are simulated using this description. The accuracy of a second description of the free surface which is called semi-Lagrangian is tested for the simulations of earthquake generated tsunamis. The results obtained using the present model are compared with those of other well known models and with experimental measurements. The comparisons demonstrated the accuracy and the reliability of the model for the simulations of tsunami generation, propagation and run-up.

ÖZET

DENİZ TABANINDAKİ HEYELANLAR İLE SÜRÜLEN DOĞRUSALDIŞI DALGALARIN HAREKETLERİNİN VE KIYIYA TIRMANIŞLARININ AĞSIZ SAYISAL YÖNTEMLE MODELLENMESİ

Bu çalışmada deniz tabanında oluşan yer hareketleri sonucunda oluşan tsunamilerin incelenmesi için iki boyutlu, ağsız, sayısal bir model sunulmaktadır. Modelde doğrusaldışı potansiyel dalga probleminin çözümü, Laplace denkleminin temel çözümünü taban fonksiyonu olarak alan ağsız bir eşyerleşim yöntemi ile elde edilmektedir. Kullanılan yöntemde çözüm için sadece çözüm alanının sınırlarındaki eşyerleşim noktaları yeterli olduğundan derin okyanuslar üzerinde uzun mesafeler kateden tsunamilerin modellenmesi etkin bir şekilde yapılabilmektedir. Laplace denkleminin temel çözümü tekil bir fonksiyon olduğundan eşyerleşim noktaları ile taban fonksiyonunun tanımlandığı noktalar farklı olmak zorundadır. Bu noktalar arasındaki uzaklık çözümün doğruluğunu ve hassasiyetini doğrudan etkilemektedir. Model, taban hareketlerini zamana bağlı bir derinlik fonksiyonu veya hız fonksiyonu olarak işleyebilmektedir. Gerek su yüzeyindeki, gerekse de tabandaki hareketler yöntemin ağsız olmasından kolayca modellenebilmektedir. Su yüzeyindeki eşyerleşim noktalarının iki boyutlu hareketleri için tam-Lagrange tanımlaması kullanılmıştır. Bu tanımlama ile tsunamilerin kıyıya tırmanışlarının modellemesinde ilave bir sınır şartına veya yönteme gerek duyulmamıştır. Ek olarak, su yüzeyindeki eşyerleşim noktalarının sadece düşeydeki hareketlerine izin veren yarı-Lagrange tanımlaması tabanın sadece düşey yöndeki harek etleri ile sürülen tsunami modellemesi için kullanılmıştır. Sunulan çalışmanın sonuçları başka araştırmacıların deneysel ve sayısal çalışma sonuçları ile karşılaştırılarak geliştirilen ağsız sayısal model ile tsunamilerin yaratılışlarının, deniz yüzeyindeki hareketlerinin ve kıyıya tırmanışlarının doğru ve hassas bir şekilde modellenebileceği gösterilmiştir.

TABLE OF CONTENTS

LIST OF FIGURES

LIST OF TABLES

LIST OF SYMBOLS

a_0	Initial acceleration
$\mathbf{B}$	A boundary condition operator
B	Length of a semi-ellipse
$\mathbf{b}$	Right hand side vector of boundary condition
b_i	Elements of the vector $\mathbf{b}$ at ith row
b	Length of the deforming bed section
c	Wave celerity
C	Parameter of the $sech^2$ curve
d	Dimension
dh	Step size
dt	Time step
dx	Horizontal nodal spacing
dz	Vertical nodal spacing
F	Function defining a surface
$\mathbf{F}$	Coefficient matrix
f	Approximating function
f_d	First order derivative of a function
g	Gravitational acceleration
H	Wave height
$\mathcal{H}$	Heaviside step function
h	Water depth
h_1	Water depth over shelf
h_0	Undisturbed water depth
k	Wave number
M	Number of sources or RBF centers
$\vec{n}$	Unit normal vector
N	Number of collocation nodes
N_{FS}	Number of the free surface collocation nodes

N_B	Number of the bottom collocation nodes
r	Geometrical distance
R	Maximum run-up
$\mathbf{S}$	System matrix
S_{ij}	Entity of matrix $\mathbf{S}$ at the ith row, the jth column
$S(t)$	Distance taken by a sliding body
S_0	Initial position of a sliding body
T	Thickness
t	Time
t_c	Characteristic time
t_0	Characteristic duration
u	Horizontal velocity
u_t	Terminal velocity
$\vec{V}$	Velocity vector
$\vec{V_b}$	Velocity vector of bottom boundary
w	Vertical velocity
x	Horizontal coordinate component in the Cartesian System
x_0	Initial horizontal position
x_c	Horizontal position of center
x_c	Horizontal position of the midpoint of semi-ellipse on its surface
x_L	Horizontal position of a water particle in the full-Lagrangian description
x_l	Horizontal position of inflection point on the sliding body back
x_{l0}	Parameter of the $sech^2$ curve
x_r	Horizontal position of inflection point on the sliding body front
y_0	Initial value of a function at $x = x_0$
z	Vertical coordinate component in the Cartesian System
z_b	Vertical elevation of the sliding semi-ellipse
z_L	Vertical position of a water particle in the full-Lagrangian description

α	Vector of weighting coefficients
α_j	jth weighting coefficient
β	A constant depending on the characteristic time
Δh	Maximum vertical height of the sliding body
ϵ	Spreading parameter
η	Free Surface Elevation
κ	Parameter of the $sech^2$ curve
ϕ	Velocity Potential
ϕ^*	Numerical value of velocity Potential
ϕ_L	Velocity potential in the full-Lagrangian description
ϕ_S	Velocity potential in the semi-Lagrangian description
σ	Shape parameter
θ	Angle of the sloping bottom
ξ	Perpendicular distance to slope
ζ_0	Amplitude of the deforming bed section
ζ	One of the coordinate directions
$\partial\Omega_B$	Bottom boundary
$\partial\Omega_{FS}$	Free surface boundary
$\partial\Omega_{W1}$	First vertical wall boundary
$\partial\Omega_{W2}$	Second vertical wall boundary

LIST OF ACRONYMS/ABBREVIATIONS

2D	Two Dimensional
3D	Three Dimensional
AB O(4)	Adams-Bashforth 4th Order
BBC	Bottom Boundary Condition
BEM	Boundary Element Method
BVP	Boundary Value Problem
CN	Crank Nicolson
DFSBC	Dynamic Free surface Boundary Condition
FLD	Full-Lagrangian Description
FNLFLD	The model in which the full-Lagrangian description of the fully nonlinear free surface is utilized
FNLSLD	The model in which the semi-Lagrangian description of the fully nonlinear free surface is utilized
FNPF	Fully Nonlinear Potential Flow
FNHDB	Fully Nonlinear, Highly Dispersive Boussinesq
FNDBEM	Fully Nonlinear, Dispersive Boundary Element Model
FNWDB	Fully Nonlinear, Weakly Dispersive Boussinesq
FSBC	Free Surface Boundary Condition
GA	Good Agreement
GE	Governing Equation
KdV	Korteweg-de Vries
KFSBC	Kinematic free surface boundary condition
LBC	Lateral Boundary Condition
MA	Moderate Agreement
MFS	Method of Fundamental Solutions
PA	Perfect Agreement
PBBM	Peregrine Benjamin Bona Mahony
RBF	Radial Basis Function
RBFCM	Radial Basis Function Collocation Method

RHS	Right Hand Side
RK O(4)	Runga-Kutta 4th Order
SLD	Semi-Lagrangian Description
SMF	Submarine Mass Failure

1. INTRODUCTION

Tsunamis are very long and powerful waves that propagate at great speeds over long distances without dissipating energy and evolve into deadly waves at near-shore. These tsunamis are usually generated by sudden seafloor deformation which can occur due to earthquakes or submarine landslides. Volcanic eruption, glacial carving or a large meteorite striking the ocean surface can also cause tsunamis but these events are rarer than seabed deformations that are main focus of this study.

Tsunami hydrodynamics received the attention of scientists after recent tsunami events, because of the destructive impacts of tsunamis on coastal zones. In order to minimize the catastrophic damages of tsunamis, analytical and numerical models are in great demand for predicting behavior of future tsunami events. In addition to these models, experiments are conducted to understand the complicated behavior of tsunamis and to validate models in terms of reliability and accuracy. These developments are crucial to create feasible early warning systems that can mitigate the catastrophic hazards of tsunamis.

In most of the studies, the tsunami phenomenon is divided into three stages to overcome its complexity. The initial stage is the generation in which a massive amount of water is displaced by an impulsive disturbance. The second stage is the propagation of the generated wave or a series of waves towards the shore. The subsequent inundation and run-up of these waves are classified as the final stage. As all of these three stages are complicated, they are usually studied separately.

In this study, a boundary-type meshless method is proposed to develop a numerical model of non-breaking waves that are generated by bottom motion. The proposed model solves the classical wave boundary value problem with fully nonlinear free surface conditions using the method of fundamental solutions. The nonlinear free surface boundary conditions are integrated using two different descriptions of the deforming free surface. Deformations of the free surface and the seabed are efficiently implemented

due to the nature of this mesh-free method.

The model presented in this study is a fully nonlinear, dispersive model which is valid over irregular bathymetry without any constraint on the wave height and wave length. The accuracy of the present numerical model is validated through benchmark problems which have been selected from literature. The results of laboratory experiments in addition to the results of other published models are compared with present results. Comparisons showed that the present method is capable of accurately simulating all of three stages of tsunami event.

In Chapter 2, an overview of the generation, propagation and run-up of tsunamis is given with historical examples. A literature review on tsunami modelling is also included in this chapter. The theoretical formulation of the wave motion and its application by the proposed model is presented in Chapter 3. The numerical method which is utilized to approximate the solution of the boundary value problem are explained in Chapter 4. The details of the time-stepping using the descriptions of the free surface are given in this chapter. The results obtained from the simulations of the benchmark problems using the numerical model are presented in Chapter 5 together with those of other published models and experimental measurements. The concluding remarks and recommendations are given in the Chapter 6.

2. TSUNAMI

2.1. Tsunami Overview

2.1.1. Generation

Earth core forces tectonic plates to move continuously at a very low rate of less than 10 cm per year. At convergent boundaries, where two tectonic plates approach each other, a tectonic plate is driven down or up by its neighboring plate. Since the friction between two forced tectonic plates may be very high, they can stick together instead of moving slowly. When the accumulated energy of the faults on the bottom of the ocean are released through earthquakes, tsunamis may be triggered.

Earthquakes are classified in terms of their faults according to relative motion of neighboring tectonic plates. Three types of faulting are illustrated in Figure 2.1. If one tectonic plate moves upward with respect to its adjacent plate, it is called a thrust fault and lifts the water column which is located above the moving plate [1]. This impulsive bed upthrust produces positive wave that propagates under the impact of restoring gravitational force. An example of thrust faulting caused tsunami occurred in Japan on 11th March, 2011 [2], on the convergent boundaries between the Pacific and North America plates.

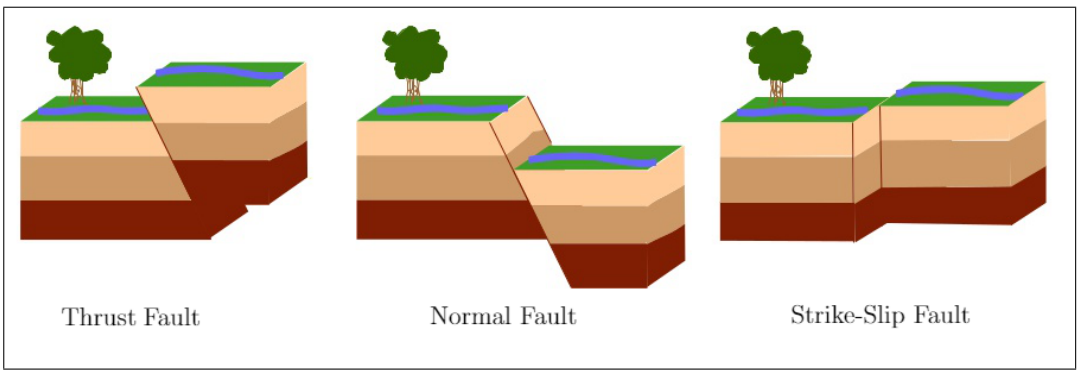

Figure 2.1. Illustration of Faults [3].

Another important fault type that generates tsunami in ocean is normal fault where one tectonic plates slides downward relative to its neighboring plate. This negative bottom movement creates a negative wave followed by a series of smaller waves. As an a example, the source of January 2007 Kuril Island Earthquake was a normal fault that induced tsunamis [4, 5]. Tsunamis may be produced by normal and thrust faults individually as in given examples or by their combination. Combined effect of positive and negative bottom movements at the boundary between the south Asian and India-Australian plates triggered the wave generation in the 2004 Indian Ocean Tsunami [1]. Third type of faulting is the strike-slip fault that allows only lateral motion of plates relative to each other. This type of motion on the seafloor is not directly associated with the generation of tsunamis. Nevertheless, it may have indirect influence on tsunami generation by initiating a submarine mass failure (SMF). Independent of fault type and magnitude, any earthquake can cause SMF that may trigger tsunamis. It should be noted that submarine mass failure is a general term that can be used for any type of underwater mass movement like a submarine landslide or a submarine slump. The present study focuses on submarine landslides on a sloping bottom rather than submarine mass failure albeit their wave generation mechanisms being similar.

Underwater mass movements have received attention in the few decades particularly following the 1998 Papua New Guinea Tsunami. Observations and models proved that the 1998 Papua New Guinea Tsunami resulted from SMF which was brought about by an earthquake [6, 7]. Although detection of the amplitude and location of vertical movement of the plates can be made by today's technology, it is difficult process to specify the exact location and impact zone of submarine mass failure. Analysis showed that a submarine landslide may have contributed to the 2011 Japan Tsunami in addition to the vertical motion of the faults [8]. Inundation and run-up of this tsunami could not be reproduced correctly by simulating only vertical motion despite the fact that vertical motion was the major cause of the tsunami. It was indicated that inundation could have been enhanced by a landslide, but the lack of a detailed bathymetry map of the area complicates the detection of the landslide zone [8].

During the generation of earthquake tsunamis, a huge section of tectonic plate works as a horizontal wave paddle which displaces a large amount of water vertically. This displaced water creates an unstable hump or dip depending on the type of faulting [9]. Once the water column above the moving plate gains potential energy, it is converted to wave energy by the restoring force of gravity so that wave propagation is initiated. Tsunami generation due to earthquakes occurs over very large length scales that are on the order of hundreds of kilometers [10]. Consequently, the generated waves have very long wavelength ($O(100km)$) and they may have very small amplitude ($O(1m)$) near generation zone due to the fact that the vertical motion of the tectonic plates has the length scale on the order of meters [6]. Thus their destructive power may stay undetected with the naked eye at deep water.

The length scales over which the submarine landslides occur are much smaller than the tsunamigenic earthquakes (O(1km) vs O(100km)) [10]. Thus, the landslide generated waves have shorter wave lengths than earthquake tsunamis have [7, 8]. Even so, landslide generated tsunamis may be classified as long waves since experiments and numerical models showed that their horizontal velocity distribution is nearly uniform over depth [11].

The wave generation due to the vertical motion of the submarine landslides is analogous to the wave generation due to the motion of the tectonic plates in normal faults. A dip on the free surface is created just above the mass that is sliding on the sloping bottom. In addition to the dip, horizontal motion of the landslide accelerates the fluid in the horizontal direction like a wave paddle and forms a wave crest. Therefore, the steepness of the sloping bottom is an important parameter that determines the characteristics of the generated waves. On very steeply sloping bottoms, vertical motion of the sliding mass dominates the wave generation process. Whereas on mild slopes the horizontal motion can be dominating factor considering the fact that a submarine landslide may take place even at the slopes lower than 2° due to excess pore water pressure [12].

Another difference between tsunami generation mechanisms of earthquakes and landslides is their durations. Tsunamigenic earthquakes occur generally at deep water and the deformation of the seafloor in deep water has to be rapid so that released energy can be converted to wave energy instantaneously. In the case of slow bed deformation in deep water, tsunamis cannot be created, because equilibrium at the free surface can be maintained during deformation [9]. On the other hand, the duration of a typical tsunamigenic underwater landslide is usually much longer than duration of tsunamigenic earthquakes. The longer duration of tsunamigenic landslides decreases energy transfer from landslide to water [13]. However, amplitudes of waves that are created by landslides can be significantly high at near field region of generation, owing to fact that SMFs generally take place at continental slopes [14] and the required energy to displace the water column in shallow water is less than in deep water.

SMFs are more dangerous when they occur in shallow water because of the limited energy transfer from landslide to the water. Contrary to SMFs, earthquakes are more dangerous in deep water for tsunami generation [13], although their vertical motion is limited to only few meters [6]. Rapid motion of the seabed increases the efficiency of instantaneous energy transfer to tsunamis from moving plates which is capable of displacing a larger amount of water in deeper water.

2.1.2. Propagation

Propagation of earthquake tsunamis has its own distinct and unique characteristics which differs them from climatic waves. This holds true also for SMF induced tsunamis due to the uniqueness of their generation mechanism. Tsunamis propagating over variable bathymetries undergo wave transformations just like wind waves do. The presence of oceanic currents, strong winds and the effects of bottom friction can also transform tsunamis. Such transformations will not be considered in the present study. In this subsection, the propagation of earthquake tsunamis and SMF induced tsunamis are examined separately by addressing their main differences.

The amplitude of earthquake tsunamis in the generation is on the order of meters, thus, the ratio of the wave height to the wavelength and to the water depth for these tsunamis is expected to be much less than unity in deep ocean. Therefore, linear wave theory is applicable for the estimation of the earthquake triggered tsunami behaviour [15]. The wavelengths of these tsunamis can reach hundreds of kilometers which is far greater than observed in most other types of waves. These waves have the characteristics of shallow water waves even in deep oceans and their wave speed is calculated using the equation for shallow water wave celerity [15–17] as in Equation 2.1

$$c = \sqrt{gh} \tag{2.1}$$

where c, h and g stand for the wave celerity,water depth and gravitational acceleration, respectively. Equation 2.1 is useful to gain insight about how earthquake triggered tsunamis can cross oceans. In a 4 km depth of ocean, a tsunami wave propagates with a wave celerity around 198 meters per second ($713kph$). However, all the components that the earthquake generated tsunamis consist of may not propagate with the same phase speed, some of them may be dispersive.

Another important aspect of an earthquake generated tsunami is the rate of energy loss during propagation. While these tsunamis carry a huge amount of energy, they can travel long distances in several hours without dissipating energy which is directly linked to wavelength [17]. Due to very large wavelength, they dissipate very little energy until they reach continental slopes. When they reach continental slopes, they start to shoal and their wave height may increase dramatically because of their very long wavelengths. Shoaling increases the non-linearity and the intensity of the energy that a single tsunami wave carries. Thus, the earthquake generated tsunamis may form very steep shorter waves during shoaling.

As mentioned above, the relatively longer duration of the submarine landslides decreases the rate of energy transfer from motion of sliding mass to water despite large amount of energy release during entire motion of landslide [18]. Therefore less potential

energy is converted to wave energy by submarine landslides [7]. Additionally, landslide generated tsunamis dissipate more energy due to their shorter wavelengths, since energy dissipation of waves during propagation is inversely proportional to wavelength. Consequently, landslide generated tsunamis carry much less energy than earthquake generated tsunamis. Therefore, their far-field effects are much lower.

The nature of the submarine landslides tends to produce high frequency waves [8, 9] which are highly dispersive. Spectral analysis of landslide generated waves confirms that they are short waves of dispersive nature [19]. Thus, their phase speed cannot be estimated by Equation 2.1 which is for non-dispersive waves. Linear dispersion can be used instead

$$c^2 = \frac{g}{k} \tanh kh \tag{2.2}$$

where k is the wave number. Equation 2.2 indicates that waves with different wavelengths propagate with different phase speeds. Dispersion tends to decrease wave heights as waves separate from each other at the far-field due to the differences in their celerities [7]. Due to frequency dispersion and energy dissipation, landslides are not expected to be effective far field tsunami generators [19], although the generated waves are locally very steep.

2.1.3. Run-up and Inundation

Tsunamis have caused widespread devastation in coastal zones while penetrating more than several kilometers inland. Therefore, it is very crucial to understand the run-up and inundation mechanisms of tsunamis to mitigate their potential hazards. Run-up and inundation is mainly dependent on the shoreline topography and the characteristics of the incoming wave. In this subsection, the characteristics of the earthquake and submarine landslide tsunamis during run-up are briefly presented.

A landslide over a sloping bottom generates two series of waves; while one of these propagates in the direction of the landslide the other propagates in the opposite

direction. [9]. Because the waves generated by a landslide propagate along the axis of motion of landslide, they are markedly directional [18], whereas earthquake induced tsunamis may be equidirectional [20] or weakly directional. For this reason, distribution of tsunamis along a coastal is a reliable indicator to distinguish whether a tsunami was generated by an earthquake or a submarine landslide. In Figure 2.2, run-up measurements are given for the 1998 and 2002 Tsunamis at Papua New Guinea [21]. As can be understood from the distribution of run-up measurements in Figure 2.2a, the 1998 Papua New Guinea Tsunami is a directional tsunami, in other words, a landslide induced tsunami. On the other hand, the nearly uniform distribution of run-up measurements for the tsunami of 2002 reflects the characteristics of a earthquake generated tsunami.

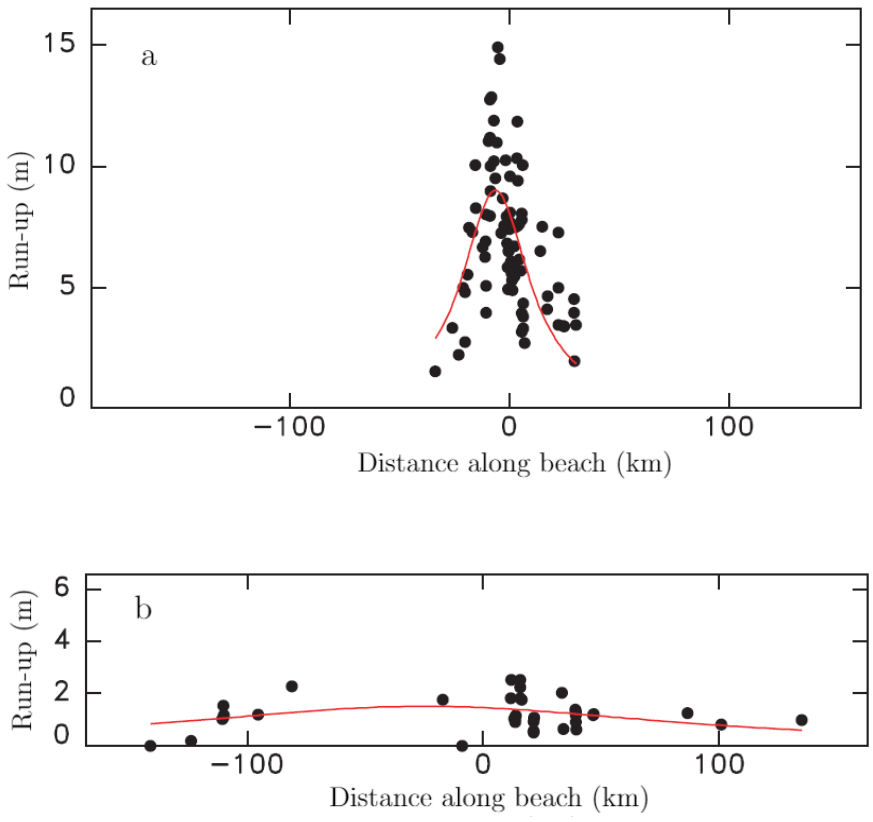

Figure 2.2. Run-up measurements of tsunamis:(a)1998 Papua New Guinea, (b)2002 Papua New Guinea [21]. Dots and solid lines represent measurements and fitted curves, respectively.

Under wind waves, water particles trace closed orbitals and their velocities decrease with increasing depth. Most of the energy of wind waves is concentrated in the vicinity of the surface. Thus, the rate of energy flux is low between water columns of wind waves, even if they are of large amplitude [22]. Contrary to that of wind waves, the kinetic energy of earthquake generated tsunamis is uniformly distributed throughout the entire water column [15]. This uniform distribution results in efficient conversion of kinetic energy to potential energy with little energy loss. Efficient conversion increases the wave height and the availability of energy to drive a larger run-up on a sloping beach [22]. Thus, the earthquake generated tsunamis may produce high run-up heights even in the far-field regions.

For the study of run-up and inundation of tsunamis, different types of long waves are employed especially in the models which are not able to generate water waves by bottom motion. A variety of different wave types which have the features of tsunami during run-up has been suggested by researchers. However, selection of appropriate wave type is a controversial topic in the literature. In this study, a few types of waveforms are presented along with the reasons of why they are commonly used. These waveforms are illustrated in Figure 2.3.

A widely used waveform to investigate the run-up of tsunamis is the solitary wave whose stable shape does not change during propagation over constant depth even after interacting with another solitary wave [23]. In addition, the kinetic energy distribution of a solitary wave is distributed over the entire water column similar to that of a tsunami [22]. Such a uniform distribution heightens availability of potential energy flux [24] which is the important factor behind the larger run-up values of tsunamis [22]. Furthermore, it has been theoretically and experimentally shown that a large positive wave that has been produced by an impulsive upward seabed deformation may evolve into solitary waves after a sufficient propagation distance [25]. Therefore, the use of solitary waves for tsunami run-up predictions or reproductions seems to be appropriate especially when the tsunami is generated by an upward seabed deformation.

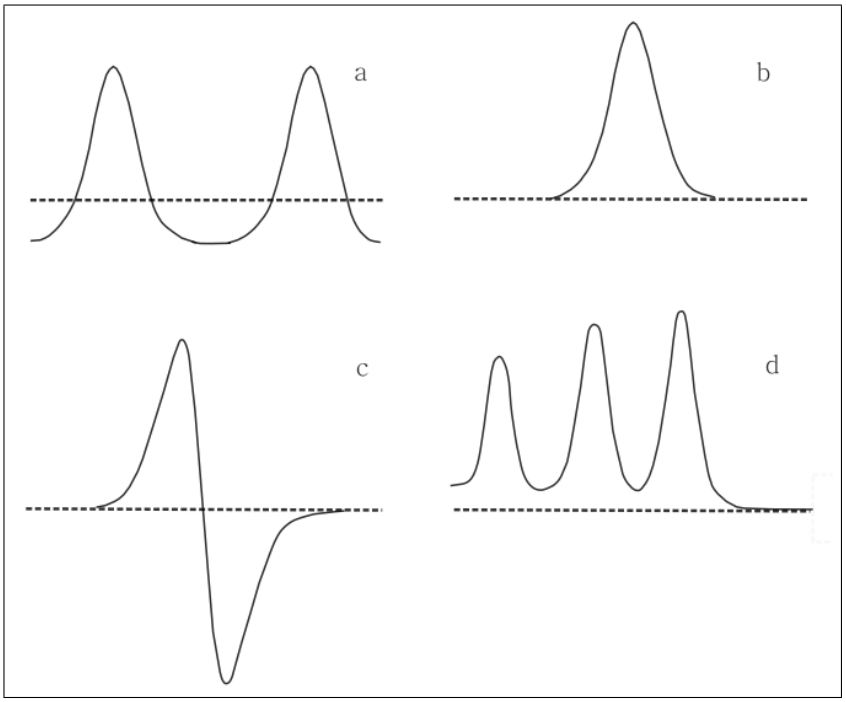

Figure 2.3. Illustration of Waveforms:(a)cnoidal, (b)solitary, (c)N-wave, (d)undular bore.

Cnoidal waves which are periodic long waves are also suggested for tsunami run-up analysis [23] . In addition to their shape being similar to that of a solitary wave, they have troughs below the still water level as shown in Figure 2.3. However, the use of cnoidal and solitary waves is not suitable for tsunami run-up studies especially when tsunamis that are under investigation are generated by motion of normal faults or by submarine landslides where water is displaced dominantly in the downward direction.

Although the evolution of solitary waves or cnoidal waves caused by an upward vertical bottom motion is observed in the far-field in the numerical simulations after considerably long simulations times [25], the evolution of these waves can be questioned in terms of oceanographic scales [26]. The waves of the numerical model and experiments in [25] were steep and highly non-linear whereas tsunamis in deep water do not attain such steepness or nonlinearity. In real tsunami events, an unstable positive hump that is produced by upward vertical motion may evolve into undular bores after sufficient time over constant depth or on a sloping beach [26]. However

the distance, that earthquake-induced tsunamis travel, may not be sufficient for the full evolution of solitary waves or cnoidal waves from this undular bore. Separation of solitary waves may not occur due to the low dispersion of these tsunamis. As tsunamis generated by earthquakes are expected to be non-dispersive, their speed is approximated by Equation 2.1 in which the wavelength does not have any effect on wave celerity unlike Equation 2.2. Therefore, tsunamis tend to propagate as wave packets. But if they become nonlinear enough during shoaling, the amplitude dispersion may enable the full separation.

Another wave type that is suggested for tsunami run-up and inundation investigations is the N-wave [27] that is a combination of a depression and an elevation as shown in Figure 2.3. Depending on the shape of its leading part, it can be named as a leading elevation N-wave or a leading depression N-wave. These waves are very stable and preserve their N-shape even over long propagation distances [28]. Additionally, these waves consist of a large variety of dipolar waveforms which can be used for tsunami run-up predictions [20]. Spreading and amplitudes of the poles, which can vary depending on type of bottom motion and its kinematics, result in different forms of N-waves. It is appropriate to use N-waves instead of solitary waves for examining tsunami run-up and inundation, especially, when generated waves have negative waves below still water level as in the case of normal fault motion or as in the case of submarine landslide. Examples of these types of N-waves have been observed in the Thailand Tsunami in 2004 and 1994 Indonesia Tsunami. [26].

It is found that leading depression N-waves have substantially higher run-up values than identical leading elevation N-waves [27]. The reason behind this run-up difference is the wave steepness that is increased by the reflection of the leading depression. It is also suggested that the run-up of a leading depression N-wave is greater than that of a solitary wave that has same wave height [27]. Thus, submarine landslide tsunamis which carry much less energy than earthquake tsunamis may produce high run-up values in the near field comparable to those of earthquake generated tsunamis. However, since the shape of N-waves is strongly dependent on the steepnes of the bottom slope in the generation zone and the kinematics of the slide, a leading depression

N-wave whose depression is significantly larger than its elevation may be produced. Consequently, greater run-down may be observed rather than run-up.

In the light of the above mentioned facts, it might be concluded that run-up values of different type of waves may differ due to their shape, although their potential energy, wave steepness and wave height are same. So it is crucial to use the proper wave type for analytical and numerical tsunami run-up models that are not capable of simulating tsunami generation due to seabed deformation. Using only one wave for the production of real tsunami run-up data can lead to unreliable results, because incoming tsunamis may consist of a series of successive waves rather than distant N-waves. Thus, the tsunami run-up models should rely on field data or the data generated by the numerical model that is able to generate waves accurately as a result of seafloor deformation [26].

Statistical analysis has shown that only one fourth of tsunamis break during run-up [29]. Although survey reports after tsunami events emphasize breaking of tsunamis, it is suggested that shorter climatic waves traveling on tsunamis are breaking [26]. During breaking, a wave dissipates a large portion of its energy, but the currents driven by the breaking tsunamis still have the capability of running up the beach and inundating dryland.

2.2. Tsunami Modelling

In the recent decades, devastating tsunami events have accelerated the developments in tsunami hydrodynamics. The recent considerable advances in the speed and storage capacity of computers has enabled scientists to simulate tsunami evolution and their possible impacts on coastal zones more efficiently and accurately. In conjunction with computational efforts and developments in tsunami hydrodynamics, laboratory experiments have been conducted to understand the physics of tsunamis and to validate existing mathematical models. In this section, a brief literature review on analytical, numerical and experimental tsunami modelling is given by focusing on the experiments and models that are used to validate present model.

Hammack conducted a series of laboratory experiments [30] to examine the water waves generated by the vertical motion of a bed section in a wave tank that was 31.63 m long, 0.6096 m deep and 0.3937 m wide. Sidewalls of the wave tank were impervious and made of glass. In the experiment, waves were generated by a horizontal wave generator that was placed perpendicular to impervious vertical wall at the upstream region of the wave tank. Except the region of the wave generator, the bed of the wave tank was flat and non-deformable. The generated free surface elevations were measured by electronic gauges at four different locations that were 0,20,180 and 400 water depths away from the wave generator. Normalized time series data of these measurements have been widely used by researchers to validate the accuracy of their models.

Hammack also presented an analytic integral solution based on linear potential theory for the waves generated by a vertical bed deformation. The solution presented is able to describe the free surface profile during the generation and propagation of waves at constant depth. Arbitrary bottom deformations given as a function of time can be easily implemented. It has to be noted that the solution is applicable when the tsunami energy does not spread radially as in the case of laboratory experiment that he conducted in the wave tank having shape of rectangular prism. Hammack examined the validity of his solution by the results of his laboratory experiments.

In the same publication [30], several non-dimensional parameters which determine the characteristics of the generated waves are suggested. Using a time-size ratio, deformations are classified as impulsive, transitional and creeping deformations, since the duration of bed displacement is not always dominant factor for generation of waves by a horizontal wave generator. It is indicated that the duration of impulsive bed deformation which is shorter than a critical time does not affect the characteristics of generated waves. Wave amplitudes reach their maximum value by impulsive bed deformation but do not exceed half of the amplitude of the deformation. However, duration of slower motions as in creeping bed deformation is an important factor that determines the generated wave amplitude. Hammack suggested that the longer duration in creeping deformation decreases the amplitude of the generated waves.

While examining the validity of his solution, Hammack concluded that his solution predicts the free surface elevation of water waves accurately in the generation zone unless the ratio of bed displacement to water depth does not exceed 0.2. However, his solution breaks down with propagation due to the increasing nonlinearity. Therefore, Hammack suggested the use of the PBBM equation to model the propagation of the generated waves [30]. The PBBM equation is a type of Korteweg-de Vries (KdV) equation with improved dispersion characteristics and called after its developers Peregrine, Benjamin, Bona and Mahony. Hammack simulated the laboratory experiment using the PBBM model [30]. His linear solution was used as input in the PBBM model which is not capable of simulating the bottom motion. Their results indicated that in the near-field the PBBM equation modeled the experimental waves quite accurately. However, in the far-field the waves from the experiment were found to have slightly smaller amplitudes and to propagate slower than those predicted by the PBBM equation. The forms of the predicted and experimental waves were found to be in good agreement. The differences in the amplitudes and propagation speeds was attributed by the authors to be due to the side wall friction in the laboratory flume.

Hammack and Segur utilized the asymptotic solution of the KdV equation to predict the far-field behaviour of the wave systems that were produced by displacing the water in the laboratory flume vertically [25]. It was suggested that stable solitons evolve after sufficient propagation if the initial net volume of the water displaced by the horizontal wave generator is positive. For a variety of given initial data, they predicted the amplitude of the leading soliton and the number of the solitons that may evolve during constant depth propagation from the initial data. In addition, they estimated the required separation distance for the evolution of the solitons from the given initial data. The predictions of Hammack and Segur for the far-field wave behavior were compared with the results obtained in the laboratory experiment. The solitons observed in the far-field wave gauges of the laboratory flume were not fully separated and they were ordered such that the wave with the largest wave height leads the wave train.

Hammack and Segur conducted additional experiments to understand the effects of small oscillations that were added to the bed movement, as the motion of earthquake can not be simulated only by a simple piston motion [25]. Three different bed deformations which have same mean motion were examined. Small-amplitude oscillations added to the the bed deformation generated high frequency waves which were observed in the near-field gauges. However, the waves were almost identical to those of the case without the oscillations in the far-field due the fact that dispersive high frequency waves were left behind by the time the waves arrived at the far-field gauges. Thus, it might be concluded that mean motion of the wave generator determines the characteristics of the leading waves and high frequency waves that are the result of minor oscillations of the bed movement can be damped by the effects of viscosity and dispersion.

Hammack and Segur conducted another set of experiments in which the initial net volume of water displaced by the horizontal wave generator is negative as in the case of normal fault motion [31]. In the experiments, a large negative triangular leading wave followed by dispersive oscillatory waves was observed in the far-field gauges. The dominant wave number of the oscillatory waves and the amplitude of the leading wave were predicted by Hammack and Segur using the asymptotic solution of the KdV equation from a wide range of the initial net water volume that was obtained in the laboratory experiments. Thus, the predictions and the measurement in the far-field gauges could be compared.

Synolakis derived a run-up law that relates the maximum run-up of a solitary wave to its wave height, water depth and the angle of the beach slope [32]. He also introduced an integral solution whose evaluation gives the free surface profiles of the climbing solitary waves. To support his findings, he conducted experiments in the same wave tank where Hammack had used to conduct his experiments. A ramp with a smooth surface was added to this tank to model the beach. Instead of a horizontal wave generator, a vertical wave generator was used. The wave generation technique proposed by Goring [23] was modified by Synolakis to produce solitary waves. Modern equipment was obtained for accurate run-up measurements at the ramp. The theory

that he derived for non-breaking solitary waves was found to predict the maximum run-up and the surface profiles accurately. In addition to the run-up law for solitary waves, Tadepalli and Synolakis proposed another run-up law for N-waves [27]. Morevover, an integral solution for cnoidal waves was presented by Synolakis *et al*. [33]. A numerical model that solves the nonlinear shallow water equations using a variable mesh finite difference technique was presented by Titov *et al*. to model the evolution breaking and non-breaking waves on a sloping bottom [34]. The accuracy of the model was confirmed by comparison to the experimental results given in [32].

A detailed study which compares the maximum run-up of different waveforms was established by G.F Carrier *et al*. [35]. Using the Hankel transform, they solved the nonlinear shallow water equations with different initial conditions of waveforms. They investigated the maximum run-up and run-down of various N-waves which may be result from an earthquake or a submarine landslide. An experimental study of the run-up of non-breaking waves as well as that of breaking waves was performed by Klettner *et al*. [36]. They investigated the run-up behaviour of N-waves which were produced by an unique wave-making technique in the laboratory. A mathematical model was proposed to predict the results of the experiments.

Grilli and Watts introduced a 2D numerical model that is capable of simulating of waves induced by a submarine landslide [37]. Their model solves fully non-linear potential flow (FNPF) equations using the boundary element method (BEM). As the implementation of deformable boundaries can readily be implemented and the internal flow field generated submarine landslide can be accurately modeled in BEM models, this technique is suggested as being appropriate for the modeling of tsunami generation due to submarine landslides. Sensitivity analyses verified the accuracy of the model. Watts *et al*. conducted experiment in a 30 m long, 1.8 m deep and 3.6 m wide wave tank having a smooth surface ramp placed at angle of 15° [38]. To simulate the landslide, a submerged semi-elliptic shaped body was slid on the ramp between two additional parallel impervious sidewalls and the time series of free surface elevations were collected at four different locations along the wave tank. The laboratory experiment was also modelled numerically using the BEM as proposed in [37]. Comparisons between results

of the model and the experiment validated the proposed model. Results of a two-layer depth integrated model were also included in the comparisons to investigate the advantages of the FNPF model. Grilli *et al*. developed their FNPF model further and obtained a 3D numerical model for water waves generated by submarine landslides [39]. Sensitivity analyses were made by the 3D numerical model for parameters that effect generated water waves. They suggested new criteria for the applicability of 2D numerical models in terms of width and length of the sliding mass. This 3D FNPF model was validated through the new laboratory experiments [11]. They found that the horizontal velocity distribution of the submarine landslide generated wave landslide is almost uniform over the depth. Thus, they recommended that a long wave model could be used to model the long distance propagation of the submarine landslide generated waves.

Grilli and Watts also studied the waves generated by a submarine slump using their FNPF model [14]. They carried out detailed sensitivity analyses on the specific parameters which affect the generated tsunami amplitude. Furthermore, effects of the SMF deformation were explored at the generation zone and in the far-field. A series of 3D laboratory experiments for water waves generated by a sliding rigid body were conducted to validate future numerical models [40]. In these experiments, characteristics of the generated waves were examined for various initial depths of the sliding body. They tried to determine relations between the measured run-up of the waves and the kinematics of the sliding body.

A numerical model was developed by Lynett and Liu for underwater landslide induced waves and their run-up [41]. Their model solves fully nonlinear, weakly dispersive extended Boussinesq equations using the finite differences method. A 2D numerical underwater landslide was simulated using the model and using the FNPF model of Grilli and Watts [37]. The results obtained from both models were compared and analyzed. Moreover, they investigated constraints of depth-integrated equations on the modelling of wave generation by landslides. Further analysis on impacts of nonlinearity was made through the modeling of the same experiments by fully nonlinear, weakly nonlinear and the linear versions of extended Boussinesq equations. They concluded

that the role of the non-linear terms may become more important when the ratio of the landslide thickness to the landslide length increases. Lynett and Liu extended their numerical model by adding a multi-layer approach to increase the dispersive features of the equations and to expand the validity of the equations in deeper water [42]. In addition to underwater landslides, subaerial landslides ware also simulated in 3D. They derived empirical formulas which relate the maximum run-up to parameters of the landslides.

Another numerical model based on the extended Boussinesq equations was proposed by Fuhrman and Madsen [43]. They validated their numerical model through the laboratory experiments of Hammack [30], the numerical submarine landslide experiment of Lynett and Liu [41] and the laboratory experiment of Grill *et al.* [39]. Using the impulsive positive bottom deformation of Hammack [30], they observed a full evolution of solitary waves that perfectly matched the solitary wave profile given by Synolakis [32]. In addition, they extended their model to 3D and simulated the experiment of F. Enet and Grilli [40] accurately.

A non-hydrostatic model based on the Euler equations was suggested by Tijandra and Pudjaprasetya [44] to model the experiment of Hammack [30]. In the formulation of the model, the momentum equation in the horizontal direction was reduced to the nonlinear shallow water equation including the dynamic pressure term. The vertical momentum equation was approximated so that the entire water column was modeled as one layer. Along the derived horizontal momentum equation and continuity equation, their model solves the linearized vertical momentum equation using the staggered finite volume method. They extended their numerical model further [45] for the numerical submarine slide experiment of Lynett and Liu [41]. Although good accuracy was attained for the simulations of the Hammack's experiments, minor deviations from the results of disperive model of Grilli and Watts [37] were observed for the simulation of the underwater landslide. Another numerical model based on the shallow water equations was proposed by Imamura *et al.* [46]. In the model, the pressure was assumed to be hydrostatic. An important feature of the model is that bottom friction was included. The governing equations of the model were discretized using the stag-

gered leap-fog scheme for time-stepping. For increasing the computational efficiency, the nonlinear terms can be excluded in the model depending on the non-linearity of the simulations.

An advanced numerical model that includes turbulent flow by the large eddy simulation technique was presented by Liu *et al.* [47]. Run-up and run-down were investigated for waves generated by a sliding triangular prism block. They conducted a set of laboratory experiments including fully submerged sliding and submerging sliding to validate their model. The result of experiments agreed well with the results of the model. A hydrodynamic model based on the Navier-Stokes equations was developed by Maa *et al.* [48] to investige waves generated by granular landslide. In the model, the momentum equations are solved using the finite volume method, while the pressure field is found from pressure Poisson equation using the finite differences method. The model was verified by simulating the laboratory experiments of Rzadkiewicz *et al.* [49]. Unlike numerical models based on potential flow, the effects of viscosity were included as such they could investigate the interaction of the sliding mass and the surrounding water during sliding efficiently. Comparisons of waves due to the deforming landslides and rigid landslides were made and it was suggested that rigid landslides were expected to produce larger waves. Further analyses regarding deforming landslides and comprehensive reviews on the modelling techniques of landslide generated water waves can be found in the studies of Smith *et al.* and Levholt *et al.* [50, 51]. Both studies suggest that the deformation of the sliding mass has secondary effects on water wave generation and that the characteristics of generated waves depend primarily on the initial acceleration of landslide, as was also suggested by Watts *et al.* [38].

A meshless numerical model that incorporates the simulation of waves due to underwater landslides using smoothed particle hydrodynamics was proposed by Qiu *et al.* [52] . In addition to the rigid body landslide, they modeled granular landslide using the discrete element method. Their model solves the 2D Euler equations for weakly compressible flow. Simulations of laboratory experiments from literature demonstrated the accuracy and reliability of their model. Hsiao *et al.* [53] introduced another meshless model for wave propagation and run-up created by underwater landslides. The

Radial basis function collocation method (RBFCM) was employed to solve the boundary value problem of fully nonlinear potential flow theory. The Gaussian radial basis function (RBF) was chosen to approximate the solution in the entire domain. Model validation was made through the simulation of the experiment of Lynett and Liu [41]. Results of the FNPF model of Grilli and Watts [37] and the Boussinesq model of Fuhrman and Madsen [43] were also included for comparison. The model's prediction of free surface elevations for different time levels matched perfectly with those of the fully nonlinear and disperive BEM model of Grilli and Watts. Huang *et al.* extended the model of Hsiao *et al.* to study the waves resulting from a subaerial mass slide [54]. After implementation of different cases of subaerial slides using the model, the obtained results were found to agree with the results of the Boussinesq model of Fuhrman and Madsen [43].

3. FULLY NONLINEAR POTENTIAL FLOW THEORY

Boundary value problems (BVPs) where the governing equation (GE) is a differential equation subject to boundary conditions appear in studies of wave propagation and transformation. Determination of the governing equation and the boundary conditions for a BVP is based on the physical situation that is under investigation. Except for the rare cases where an analytical solution exists, the BVP is solved by numerical methods.

An illustration of 2D boundary value problem for wave propagation at constant depth is given in Figure 3.1. The governing equation is applied in the fluid domain with free surface boundary conditions (FSBCs), a bottom boundary condition (BBC) and lateral boundary conditions (LBCs). The governing equation of the classical wave boundary value problem is the Laplace equation which does not involve the time parameter. Time is introduced the free surface boundary conditions. When solving this kind of time variant problems numerically, time marching schemes have to be adopted for time dependent equations of the BVP in order to progress in time. At each time increment, the BVP has to be solved in spatial dimensions to determine the solution over its domain.

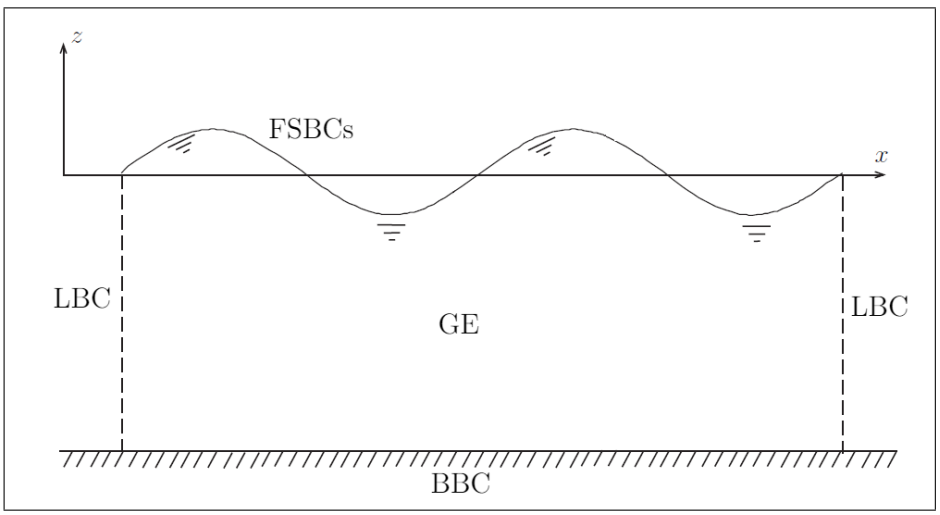

Figure 3.1. Illustration of 2D boundary value problem for water wave propagation.

The present numerical model solves the illustrated wave boundary value problem based on potential flow theory with fully nonlinear free surface boundary conditions for modeling of water wave generation, propagation and run-up. Two different descriptions of the free surface are obtained by the modification of the FSBCs for the time-stepping. Time marching schemes are adopted to integrate temporal FSBCs in the obtained descriptions. Subsequently, the results of the integration are employed as spatial boundary conditions which are required to solve boundary value problem at each time step. Deformations of the free surface are updated according to the results of integration at each time level.

3.1. Governing Equation

Potential flow theory is commonly used to represent the motion of water flow is based on the assumption that water is incompressible, inviscid and irrotational. By assuming the effect of the viscosity to be confined to boundary layers encountered at the surface and bottom, the motion in whole water column can be considered as irrotational and inviscid. Irrotationality requires that the rotation of the velocity field be zero, that is

$$\vec{\nabla} \times \vec{V} = 0 \tag{3.1}$$

where V is the velocity vector whose components are u in the horizontal x-direction and w in the vertical z-direction. This equation implies that the velocity field may be defined as the gradient of a scalar field: the velocity potential $\phi(x, z, t)$

$$\vec{V} = \vec{\nabla}\phi \tag{3.2}$$

The incompressibility condition requires that the divergence of the velocity field be zero,

$$\vec{\nabla} \cdot \vec{V} = 0 \tag{3.3}$$

In terms of the velocity potential, this equation becomes the Laplace equation

$$\nabla^2\phi = 0 \tag{3.4}$$

which is the continuity equation of an ideal fluid and the governing equation of the classical wave BVP.

3.2. Free Surface Boundary Conditions

The FSBCs are implemented on the free surface which is interface between air and water. One of the FSBCs, the kinematic free surface boundary condition (KFSBC), states that water particles on the free surface remain at the free surface throughout the motion of wave. According to Dean and Dalrymple [16], a surface $F(x, z, t)$ can be defined to describe the free surface as follows:

$$F(x, z, t) = z - \eta(x, t) = 0 \tag{3.5}$$

where $\eta(x, t)$ is free surface displacement with respect to still water level. Since particles on the free surface stays on the surface, the material derivative can be set equal to to zero,

$$\frac{DF(x, z, t)}{Dt} = \frac{\partial F(x, z, t)}{\partial t} + u\frac{\partial F(x, z, t)}{\partial x} + w\frac{\partial F(x, z, t)}{\partial z} \tag{3.6}$$

Equation 3.6 states that the free surface does not change according to an observer that moves with the free surface. Inserting Equation 3.5 into Equation 3.6 and noting that,

$$\frac{\partial z}{\partial t} = 0 \quad \frac{\partial z}{\partial x} = 0 \quad \frac{\partial z}{\partial z} = 1$$

Equation 3.6 becomes,

$$\frac{\partial \phi}{\partial z} = \frac{\partial \eta}{\partial t} + \frac{\partial \phi}{\partial x}\frac{\partial \eta}{\partial x} \qquad \text{on} \quad z = \eta(x, t) \tag{3.7}$$

or

$$w = \frac{\partial \eta}{\partial t} + u\frac{\partial \eta}{\partial x} \qquad \text{on} \quad z = \eta(x,t) \tag{3.8}$$

Equation 3.8 is the KFSBC for 2D wave propagation. Its 3D version can be derived in similar manner. The second free surface boundary condition is the dynamic free surface boundary condition (DFSBC) which from the requirement of the pressure match between water and air at the interface. Referencing air pressures to the gauge pressure, the Bernoulli equation on the free surface can be written as

$$\frac{\partial \phi}{\partial t} = -g\eta - \frac{1}{2} \mid \nabla\phi \mid^2 \qquad \text{on} \quad z = \eta(x,t) \tag{3.9}$$

The DFSBC and the KFSBC which are two nonlinear transient boundary conditions in the eulerian frame have to be satisfied on the free surface. It is worthy of note that linear wave theory can be derived from the boundary value problem, in which the governing equation is Laplace's Equation and free surface boundary conditions are linearized versions of the DFSBC and the KFSBC. Derivation of linear wave theory using the BVP can be found in [16].

For each time level, the KFSBC and the DFSBC are integrated to find new geometry of the free surface along with the velocity potentials at the surface. The velocity potentials are used as Dirichlet type information at new locations by setting up the boundary value problem. The DFSBC given in Equation 3.9 includes the local time derivative that is the time rate of change of the velocity potential at a point where the free surface momentarily located. Integration of the DFSBC given in Equation 3.9 over time yield the new velocity potentials at the points which constitute the free surface at the previous time level. Thus, the KFSBC and the DFSBC given in Equation 3.7 and 3.9 are not practical in the context of the time-marching. In present study, two different descriptions of the deforming free surface are used to integrate these transient equations. The First is the full-Lagrangian description [55] which is capable of keeping

track of the particles as well as their corresponding velocity potentials. Secondly, the semi-Lagrangian description [56] in which water particles on the surface are free to move only in vertical direction is utilized.

3.2.1. The Full Lagrangian Description

Another version of the KFSBC which also states that water particles on surface remains there throughout propagation may be given as follows [55]:

$$\frac{Dx_L}{Dt} = \frac{\partial \phi}{\partial x} \tag{3.10a}$$

$$\frac{Dz_L}{Dt} = \frac{\partial \phi}{\partial z} \tag{3.10b}$$

where x_L and z_L are Lagrangian positions of the water particles and $D()/Dt$ indicates the material derivative. Equation 3.10a and 3.10b describes the motion of water particles on the free surface in the Lagrangian frame. The integration of these equations yields the new locations of particles which constitute the new free surface profile. The DFSBC has to be modified so that integration of it can give new velocity potentials at new locations. Adding $u^2 + w^2$ to both sides of Equation 3.9,

$$\frac{\partial \phi}{\partial t} + u\frac{\partial \phi}{\partial x} + w\frac{\partial \phi}{\partial z} = -g\eta + \frac{1}{2} \mid \nabla \phi \mid^2 \qquad \text{on} \quad z = \eta(x,t) \tag{3.11}$$

$$\text{where} \quad \mid \nabla \phi \mid^2 = u\frac{\partial \phi}{\partial x} + w\frac{\partial \phi}{\partial z} = \frac{\partial \phi}{\partial x}\frac{\partial \phi}{\partial x} + \frac{\partial \phi}{\partial z}\frac{\partial \phi}{\partial z}$$

Noting that,

$$\frac{D\phi_L}{Dt} = \frac{\partial \phi}{\partial t} + u\frac{\partial \phi}{\partial x} + w\frac{\partial \phi}{\partial z}$$

the DFSBC in Lagrangian description can be written as,

$$\frac{D\phi_L}{Dt} = -g\eta + \frac{1}{2} \mid \nabla \phi \mid^2 \qquad \text{on} \quad z = \eta(x,t) \tag{3.12}$$

Integration of Equation 3.12 yields the new velocity potentials at the new locations determined by Equations 3.10a and 3.10b. Since the particles are free to move in all directions, this approach allows one water particle to pass over another. Therefore, overturning waves where the water surface becomes multi-valued can be modelled by the full-Lagrangian description (FLD) of the free surface. In the present study, run-up and run-down of non-breaking waves on a sloping beach is modelled using this description by keeping track of water particles which slip on the sloping beach.

3.2.2. The Semi-Lagrangian Description

When the horizontal displacement of the free surface water particles is assumed to be small and therefore neglected, the time rate of change of the velocity potential on the surface can be written as [56],

$$\frac{\partial \phi_s}{\partial t} = \frac{\partial \phi}{\partial t} + \frac{\partial \phi}{\partial z}\frac{\partial \eta}{\partial t} \qquad \text{on} \quad z = \eta(x,t) \tag{3.13}$$

Note that the first term on the right hand side of Equation 3.13 is local derivative, while the second term is vertical convective term where $\partial\eta/\partial t$ represent vertical velocity. So, Equation 3.13 is material derivative by which only vertical displacement is considered. Inserting Equation 3.9 into Equation, we get 3.13,

$$\frac{\partial \phi_s}{\partial t} = -g\eta - \frac{1}{2} \mid \nabla\phi \mid^2 + \frac{\partial \phi}{\partial z}\frac{\partial \eta}{\partial t} \qquad \text{on} \quad z = \eta(x,t) \tag{3.14}$$

Equation 3.14 is the DFSBC in the semi-Lagrangian form which has been coupled with the KFSBC given in Equation 3.7. The vertical displacement of water particles on the free surface is followed by Equation 3.14 which disregards their horizontal movements. Using the semi-Lagrangian description (SLD), overturning and run-up cannot be modelled as the motion of water particles on the free surface is limited to only vertical displacement.

3.3. Bottom Boundary Conditions

The bottom boundary conditions implemented in this study rely on the impermeable bottom assumption in which the seepage flow through the bottom surface does not occur. Selection of an appropriate bottom boundary condition depends on the information given for the deformable bottom whose kinematics are known beforehand either as a function of water depth or as a function of the velocity field throughout the motion .

3.3.1. Bottom Boundary Condition as a Function of Water Depth

If the motion of the bottom is known as a function of time, then the water depth can be expressed as,

$$-h(x,t) = z \tag{3.15}$$

Thus, a surface similar to the one in the Section 3.2 can defined as,

$$F(x,z,t) = z + h(x,t) = 0 \tag{3.16}$$

Since there is no flow through this surface, the material derivative of Equation 3.16 can be set equal to zero,

$$\frac{\partial(z+h(x,t))}{\partial t} + u\frac{\partial(z+h(x,t))}{\partial x} + w\frac{\partial(z+h(x,t))}{\partial z} = 0$$

Carrying out the indicated differentiation, the equation above can be rewritten as

$$\frac{\partial h}{\partial t} + u\frac{\partial h}{\partial x} + w = 0 \qquad \text{on} \quad z = h(x,t) \tag{3.17}$$

Equation 3.17 is the bottom boundary condition as a function of water depth for deforming impervious bottoms. When the water depth is known for all time, Equation

3.17 can be directly applied as a spatial boundary condition.

3.3.2. Alternative Form of the Bottom Boundary Condition

When the bottom deformation is not formulated as a function of time, the following no-flux boundary condition can be used with known velocity of the bottom.

$$\vec{\nabla}\phi \cdot \vec{n} = \vec{V_b} \cdot \vec{n} \tag{3.18}$$

where $\vec{n}$ and $\vec{V_b}$ are the unit normal vector and the velocity vector of the bottom surface, respectively. The components of the normal vector on the bottom can be found as

$$n^x = \frac{\frac{\partial h}{\partial x}}{\sqrt{(\frac{\partial h}{\partial x})^2 + 1}} \qquad n^z = \frac{1}{\sqrt{(\frac{\partial h}{\partial x})^2 + 1}} \tag{3.19}$$

where the n^x and n^z are the components of unit normal vector in x-direction and z-direction, respectively. Equation 3.19 is accurate in magnitude, but the orientation of the normal may vary according to modeller preferences. Numerical techniques may be used for spatial derivatives in Equation 3.19.

3.4. Lateral Boundary Conditions

Selection of lateral boundary conditions depends on the objective of the problem. For instance, in the derivation of linear wave theory periodicity is invoked in space where the lateral boundaries are separated by a wave length [16]. For numerical models, radiation boundary conditions or absorbing boundary conditions are popular among modellers for outgoing waves. Radiation boundary conditions are used to insure that outgoing waves do not reflect from the end of the domain. However, the no-flux boundary condition which result in complete reflection of incident waves is used in the present study for the simulation of the laboratory experiments conducted in wave tanks

having impervious end walls. This boundary condition is given as

$$\vec{\nabla}\phi \cdot \vec{n} = 0 \tag{3.20}$$

Note that Equation 3.20 is the simplified form of Equation 3.18 for the non-deforming boundaries. It can be further simplified for a non-deforming vertical wall at the end of a laboratory wave flume:

$$\frac{\partial \phi}{\partial x} = 0 \qquad \text{on} \quad x = x_{end} \tag{3.21}$$

The incident wave boundary condition that generates waves at the start of the computational domain is another type of commonly used LBC. In numerical models, incident waves can be generated either by specifying wave properties expressed as a Dirichlet boundary condition or by a utilizing wave maker with Neumann boundary condition. Equation 3.18 can be utilized for wave pedal whose motion accelerates the water in its direction of motion. In the present model, a body sliding on the sloping bottom and vertical bottom deformation work as an influx boundary that accelerates the water in the domain by its motion. Here, it has to be pointed out that the displacement of any wave makers has to be updated before the application of the boundary condition.

3.5. Summary of the Boundary Value Problem

The governing equation of the BVP is the Laplace's Equation 3.4 which is a time independent equation and has to be satisfied in the domain at all time levels.

$$\nabla^2 \phi = 0 \tag{3.4}$$

On the free surface, Equations 3.7 and 3.9 are two time dependent boundary conditions which are defined in Eulerian frame have to be integrated to march in time.

$$\frac{\partial \phi}{\partial z} = \frac{\partial \eta}{\partial t} + \frac{\partial \phi}{\partial x}\frac{\partial \eta}{\partial x} \qquad \text{on} \quad z = \eta(x,t) \tag{3.7}$$

$$\frac{\partial \phi}{\partial t} = -g\eta - \frac{1}{2} \mid \nabla \phi \mid^2 \qquad \text{on} \quad z = \eta(x,t) \tag{3.9}$$

Two different descriptions of the free surface are suggested to deal with the deformation of the free surface during integration. The first is the full-Lagragian description where the KFSBC and the DFSBC are defined in the Lagrangian frame and are given as Equations 3.10 and 3.12, respectively.

$$\frac{Dx_L}{Dt} = \frac{\partial \phi}{\partial x} \tag{3.10a}$$

$$\frac{Dz_L}{Dt} = \frac{\partial \phi}{\partial z} \tag{3.10b}$$

$$\frac{D\phi_L}{Dt} = -g\eta + \frac{1}{2} \mid \nabla \phi \mid^2 \qquad \text{on} \quad z = \eta(x,t) \tag{3.12}$$

The second is the semi-Lagrangian description where the KFSBC as in Equation 3.7 and DFSBC as in Equation 3.14 are defined at fixed x-locations.

$$\frac{\partial \phi}{\partial z} = \frac{\partial \eta}{\partial t} + \frac{\partial \phi}{\partial x}\frac{\partial \eta}{\partial x} \qquad \text{on} \quad z = \eta(x,t) \tag{3.7}$$

$$\frac{\partial \phi_s}{\partial t} = -g\eta - \frac{1}{2} \mid \nabla \phi \mid^2 + \frac{\partial \phi}{\partial z}\frac{\partial \eta}{\partial t} \qquad \text{on} \quad z = \eta(x,t) \tag{3.14}$$

For the bottom boundary condition, Equation 3.17 or Equation 3.18 can be employed depending on the given information for the bottom geometry.

$$\frac{\partial h}{\partial t} + u\frac{\partial h}{\partial x} + w = 0 \qquad \text{on} \quad z = h(x,t) \tag{3.17}$$

$$\vec{\nabla}\phi \cdot \vec{n} = \vec{V_b} \cdot \vec{n} \qquad \text{on} \quad z = h(x,t) \tag{3.18}$$

The general solution strategy of the BVP is outlined in Figure 3.2.

1- Set the initial conditions.

2- Integrate Equation 3.10 (FLD) or Equation 3.7 (SLD) using a time marching scheme to find new location of the free surface.

3- Integrate Equation 3.12 (FLD) or Equation 3.14 (SLD) using a time marching scheme to find new velocity potential at new locations.

4- Update the locations of the free surface as well as the locations of the other deforming boundary conditions.

5- Use the new velocity potentials on the free surface as Dirichlet boundary conditions and Equation 3.17 or Equation 3.18 as Neumann boundary conditions to set up the BVP.

6- Solve the BVP using a numerical method to find the new velocities and the new velocity potentials.

7- Return to step **2** for the next time level.

Figure 3.2. General solution strategy for fully nonlinear potential flow theory.

4. NUMERICAL METHOD

The classical wave boundary value problem with its linear governing equation and its nonlinear, time dependent free surface boundary conditions requires the linearization of the free surface boundary conditions and their application at the still water level so that an analytical solution can be obtained. The process involves the small amplitude wave assumptions which require that the wave height be much smaller in comparison to the wave length and the water depth.

If, as is done in the present study, the free surface boundary conditions are not linearized and applied at the free surface, an analytical solution of the problem is not possible and one must resort to numerical solutions. In addition to the deformable free surface whose location must be updated as the solution progresses, the driving mechanism of the waves consists of a landslide or a moving tectonic plate on the bottom whose location and even shape may be time dependent. Such deformable boundaries are difficult to implement when using numerical methods that require a prescribed mesh structure. Thus, it seems reasonable to consider a meshless numerical method for the present study.

The deformations on the bottom can occur at large depths and the resulting waves often propagate over large expanses of the oceans. Thus, the solution domain of the problem can be quite extensive and any numerical method that requires domain discretization would lead to large system matrices to be updated and solved as the solution progresses. To avoid taxing the computational facilities available at the time of this study, a meshless boundary only method, namely the Method of Fundamental Solutions (MFS), was chosen for the present study.

The MFS makes use of the fundamental solution of the governing equation of the problem thus rendering domain solutions unnecessary. Once the solution on the boundary is obtained, the solutions in the domain can be obtained by superposition owing to the linearity of the governing equation; the Laplace equation in the present

case.

The classical BEM which is also based on the fundamental solution of the governing equation requires the discretization of the solution domain boundary into elements (nodes, lines, curves or surface elements). The solution on the boundary is accomplished by numerical integration and a superposition for nodes in the domain follows. The main difference between two methods is that the MFS does not necessitate integration along boundaries and discretization of boundaries according to predefined rules, therefore the MFS is truly meshless.

4.1. Method of Fundamental Solutions

The MFS is a collocation method. The formulation and solution of a problem using the MFS is quite similar to that using the Radial Basis Function Collocation Method (RBFCM). The difference between the two methods comes from the nature of the approximating functions used. For the RBFCM the approximating functions are radial basis functions (RBFs) which depend on the geometrical distance of two set of points. The first set consists of the collocation nodes where the information of the problem is given and the other set is the RBF centers, where the RBFs are defined. As such RBFs are non-singular functions making it possible to place the RBF centers and the collocation points at the same geometrical location. For the MFS, the fundamental solutions which are by nature singular are used as the approximating functions necessitating the geometrical locations of the collocation points to be different from the locations of the sources where the approximating functions are defined.

The MFS which was initially presented by Kupradze and Aleksidze [57, 58] is a boundary-only meshless method in which collocation is made only on boundaries, because the GE is automatically satisfied by the approximating function which is the fundamental solution of the GE. The present model uses the fundamental solution of the 2D Laplace's equation as the source basis function to solve the BVP which has been described in the Chapter 3. The fundamental solutions for Laplace's equation in

d-dimensional space were originally introduced by M. Bôcher [59] as follows

$$C \ln r \qquad \text{for} \qquad d = 2 \tag{4.1a}$$

$$C r^{2-d} \qquad \text{for} \qquad d > 2 \tag{4.1b}$$

where C is a constant and the r indicates geometrical distance. The derivation of the fundamental solution of Laplace's equation can be found in the book of Kythe [60] along with the fundamental solutions of different types of differential equations. Equation 4.1a without the constant is chosen to be the source (approximating) function. The velocity potential can be written as the linear combination of M approximating functions f, which are $\ln r$ in the present case.

$$\phi(x, y) \cong \sum_{j=1}^{M} \alpha_j f(r) = \sum_{j=1}^{M} \alpha_j \ln r \qquad \text{where} \quad r = \sqrt{(x - x_j)^2 + (y - y_j)^2} \tag{4.2}$$

where the subscript j denotes sources whose weighting coefficient is given by α_j. The spatial derivative of the function f can be found as,

$$\frac{\partial f}{\partial \zeta} = \frac{\partial f}{\partial r} \frac{\partial r}{\partial \zeta} \tag{4.3}$$

$$\text{Noting,} \quad \frac{\partial (r^2)}{\partial \zeta} = 2r \frac{\partial r}{\partial \zeta} = 2(\zeta - \zeta_j) \quad \rightarrow \quad \frac{\partial r}{\partial \zeta} = \frac{(\zeta - \zeta_j)}{r}$$

$$f^{\zeta} = \frac{\partial f}{\partial \zeta} = \frac{\partial f}{\partial r} \frac{(\zeta - \zeta_j)}{r} \tag{4.4}$$

where ζ represents one of the coordinate directions and the superscript ζ indicates the spatial derivative in ζ-direction. The first order spatial derivatives of $\ln r$ can be

obtained using the relation given in Equation 4.4 as

$$f^x = \frac{\partial f}{\partial x} = \frac{\partial f}{\partial r}\frac{\partial r}{\partial x} = \frac{(x - x_j)}{r^2} \tag{4.5a}$$

$$f^z = \frac{\partial f}{\partial z} = \frac{\partial f}{\partial r}\frac{\partial r}{\partial z} = \frac{(z - z_j)}{r^2} \tag{4.5b}$$

Furthermore, the second order spatial derivatives can be found as

$$f^{xx} = \frac{\partial^2 f}{\partial x^2} = \frac{\partial((x - x_j)r^{-2})}{\partial x} = \frac{1}{r^2} - \frac{2(x - x_j)^2}{r^4} \tag{4.6a}$$

$$f^{zz} = \frac{\partial^2 f}{\partial z^2} = \frac{\partial((z - z_j)r^{-2})}{\partial z} = \frac{1}{r^2} - \frac{2(z - z_j)^2}{r^4} \tag{4.6b}$$

$$\text{where} \quad r = \sqrt{(x - x_j)^2 + (z - z_j)^2}$$

Note that the summation of the second order spatial derivatives given in the Equations 4.6a and 4.6b is equal to zero. Thus, the source function $\ln r$ satisfies the 2D Laplace equation naturally. The first spatial derivatives of the velocity potential can be given as

$$\frac{\partial \phi(x, y)}{\partial x} \cong \sum_{j=1}^{M} \alpha_j \frac{\partial f(r)}{\partial x} = \sum_{j=1}^{M} \alpha_j \frac{(x - x_j)}{r^2} \tag{4.7a}$$

$$\frac{\partial \phi(x, y)}{\partial z} \cong \sum_{j=1}^{M} \alpha_j \frac{\partial f(r)}{\partial z} = \sum_{j=1}^{M} \alpha_j \frac{(z - z_j)}{r^2} \tag{4.7b}$$

For the solution of the classical wave BVP, the collocation nodes where the information is supplied are placed on the physical boundaries. Collocation is made only on boundaries, thus the following linear system of equation is obtained.

$$\underbrace{\left[\mathbf{B}_{\partial\Omega} f\right]}_{S_{N\times M}} \boldsymbol{\alpha}_{M\times 1} = \mathbf{b}_{N\times 1} \tag{4.8}$$

where the operator $\mathbf{B}_{\partial\Omega}$ is a boundary condition operator and N is the number of the collocation nodes. The vector $\mathbf{b}$ stands for the right hand sides of the boundary

conditions. It has to be pointed out that the numbers of collocation nodes and sources are not necessarily same. However the number of sources M has to be greater or equal to the number of collocation nodes N so that the linear system of equations given in Equation 4.8 can be solved. In the present study, the number of sources is taken to be equal to the number of collocation nodes ($N = M$). After obtaining the coefficient vector $\boldsymbol{\alpha}$ in Equation 4.8, the velocity potential and its derivatives at any point (x, y) can be found by Equations 4.2 and 4.7, respectively.

It has been pointed out that the fundamental solutions are by nature singular. Singularity occurs when the geometrical distance r is equal to zero. Therefore, the locations of collocation nodes and sources should not coincide. The collocation nodes which depend on given information have to be placed on physical boundaries. However the sources at which the approximating functions are defined have to be located on a fictitious boundary outside the domain of interest to avoid singularities. The separation distance between the two types of points is influential on the accuracy of the solutions and is an active research area. In literature, there are several techniques to locate the fictitious boundary associated with a computational domain. An approach, which is proposed by Bogomolny, is to place a circular fictitious boundary surrounding the physical boundary [61]. Theoretically, the method accuracy increases as the distance between the collocation nodes and sources increases, thus the optimum choice for the radius of fictitious boundary is infinity [62]. However, if the distance between collocation nodes and sources becomes too large, the system matrix $\mathbf{S}$, which is equal to $\left[\mathbf{B}_{\partial\Omega} f\right]$ in Equation 4.8, becomes more ill-conditioned, because the rows of the matrix become almost identical.

There are two restrictions which have to be considered during the placement of sources for numerical accuracy and stability. Firstly, sources and collocation nodes can not be too close so as to avoid singularties. Secondly, sources can not be far away from the domain of interest, since the condition number of the resultant matrix increases. Numerical tests have shown that the accuracy of the method is not considerably affected by the ill-conditioning [62]. Thus, the sources can be located away from the physical boundary as much as the linear system of Equations given in Equation 4.8 can be still

solved by the computer within a certain degree of precision.

In the studies of Wu *et al.*, fictitious boundaries of the wave BVP were located parallel to the physical boundaries [63,64]. Numerical tests mentioned in these studies showed that if the distance between collocation nodes and RBF centers is less than the nodal spacing on the physical boundary, instability arises. In the same studies, the chosen offset distance of the sources to the physical boundaries is equal to 1.2 times of the nodal spacing on the physical boundary. In the present study, the sources were placed as shown in Figure 4.1 with an offset of 5 times the inter-nodal distance used on the boundary. The position of the sources are updated at each time increment according to positions of the collocation nodes to guarantee that the offset distance between the RBF centers and the collocation nodes remain constant. Thus, any instability that can stem from the closeness of the sources and the collocation nodes is avoided.

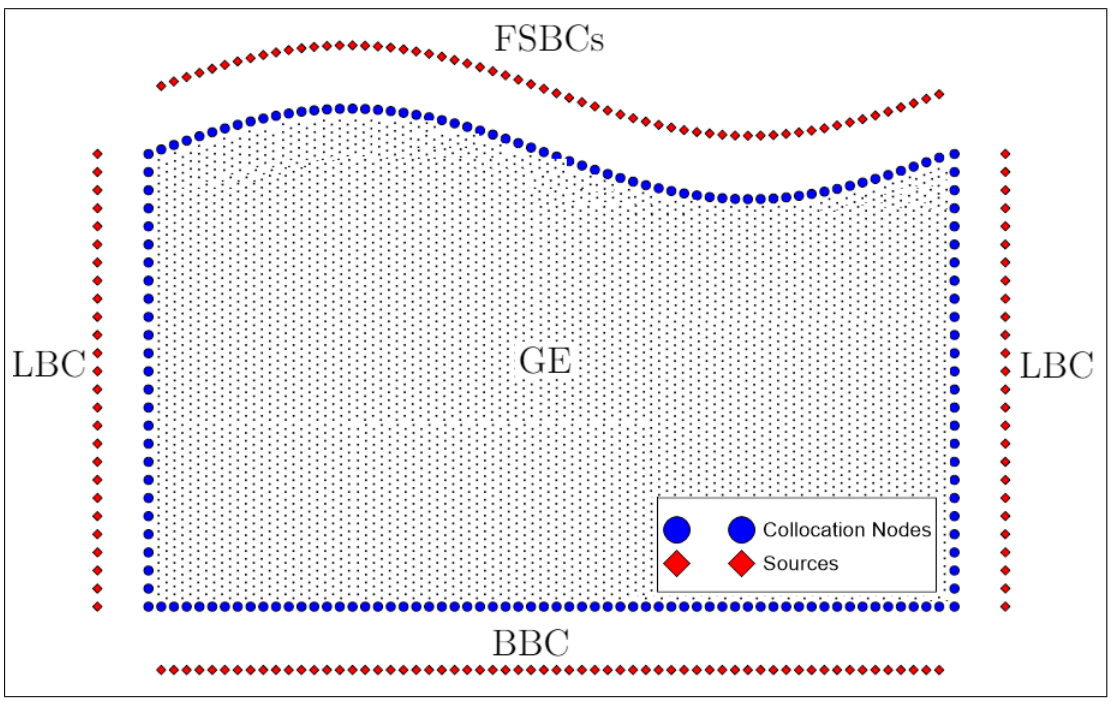

Figure 4.1. Illustration of node placement for the BVP which is given in Figure 3.1. Dotted area is the solution domain. Collocation nodes and RBF centers are located on the physical boundaries and on the fictitious boundaries, respectively.

4.1.1. Implementation of the MFS

In the present model, the system matrix **S** given in Equation 4.8 depends on the geometrical distances between collocation nodes and sources. It is a time dependent matrix due to the fact that the locations of the collocation nodes on deforming boundaries as well as the sources are modified at each time level. Depending on the type of boundary condition, the elements of the right hand side (RHS) vector **b** given in Equation 4.8 have to be also updated.

As described in the previous chapter, the KFSBC is integrated to find locations of the surface collocation nodes either in full-Lagrangian description or in semi-Lagrangian description. The velocity potentials which are used as Dirichlet type boundary conditions can be found by the numerical integration of the DFSBC using the same description that is used for the integration of the KFSBC. Application of the Dirichlet boundary condition at the ith node in the system of equations is as follow

$$f_{i1}\alpha_1 \;+\; f_{i2}\alpha_2 \;+\; f_{i3}\alpha_3 \;+\; \cdots \;+\; f_{iM}\alpha_M \;=\phi_i^* \tag{4.9}$$

where ϕ_i^* refers to the velocity potential at the ith node and it is the numerical result of the integration of the DFSBC. The source functions in Equation 4.9 are reconstructed at each time step according to the results of the integration of the KFSBC. Application of the no-flux boundary condition for a stationary vertical wall at the ith collocation node gives

$$f_{i1}^x\alpha_1 \;+\; f_{i2}^x\alpha_2 \;+\; f_{i3}^x\alpha_3 \;+\; \cdots \;+\; f_{iM}^x\alpha_M \;=0 \tag{4.10}$$

It is also important to note that although the positions of the collocation nodes on stationary walls do not change, the source functions in Equation 4.10 have to be rebuilt, since the location of the sources parallel to moving boundaries are updated at each level. When the water depth is known as a function of time, the bottom boundary condition

given in Equation 3.17 can be applied at the ith collocation node in the following way

$$(h_i^x f_{i1}^x + f_{i1}^z)\alpha_1 \quad + \quad (h_i^x f_{i2}^x + f_{i2}^z)\alpha_2 \quad + \quad \cdots \quad + \quad (h_i^x f_{iM}^x + f_{iM}^z)\alpha_M \quad = -(\tfrac{\partial h}{\partial t})_i \tag{4.11}$$

where h_i^x represents the spatial derivative of the water depth in x-direction at the ith collocation node. The alternative bottom boundary condition given in Equation 3.18 can be applied as

$$(n_i^x f_{i1}^x + n_i^z f_{i1}^z)\alpha_1 \quad + \quad \cdots \quad + \quad (n_i^x f_{iM}^x + n_i^z f_{iM}^z)\alpha_M \quad = (n_i^x u_i^b + n_i^z w_i^b) \tag{4.12}$$

where the u_i^b and w_i^b are the components of the velocity vector of the deforming bottom at the ith collocation node. Since the positions of the collocation nodes on deforming boundaries change, the source functions in Equations 4.11 and 4.12 have to be updated at each time level. The resultant system of equations in matrix form is

$$\mathbf{S}_{N\times N}\,\boldsymbol{\alpha}_{N\times 1} = \mathbf{b}_{N\times 1} \tag{4.13}$$

The construction of the system matrix $\mathbf{S}$ and the RHS vector $\mathbf{b}$ depends on the geometry of the problem that is under investigation. For the simulations in a 2D numerical wave tank which has two vertical walls at both ends and a sliding body on its bottom as illustrated in Figure 4.2, the system matrix $\mathbf{S}$ and the RHS vector $\mathbf{b}$ given in Equation 4.8 can be constructed as follows

$$S_{ij} = \begin{cases} f_{ij}, & \text{if } (x_i, z_i) \in \partial\Omega_{FS} \\ f_{ij}^x, & \text{if } (x_i, z_i) \in \partial\Omega_{W1} \\ n_i^x f_{ij}^x + n_i^z f_{ij}^z, & \text{if } (x_i, z_i) \in \partial\Omega_B \\ f_{ij}^x, & \text{if } (x_i, z_i) \in \partial\Omega_{W2} \end{cases}$$

and

$$b_i = \begin{cases} \phi_i^*, & \text{if } (x_i, z_i) \in \partial\Omega_{FS} \\ 0, & \text{if } (x_i, z_i) \in \partial\Omega_{W1} \\ n_i^x u_i^b + n_i^z w_i^b, & \text{if } (x_i, z_i) \in \partial\Omega_B \\ 0, & \text{if } (x_i, z_i) \in \partial\Omega_{W2} \end{cases}$$

where the free surface, the first vertical wall, the bottom and the second vertical wall boundaries are expressed by the $\partial\Omega_{FS}$, $\partial\Omega_B$, $\partial\Omega_{W1}$ and $\partial\Omega_{W2}$, respectively. Note that the implementation of Equation 4.12 is illustrated above. Equation 4.11 can be implemented in a similar way.

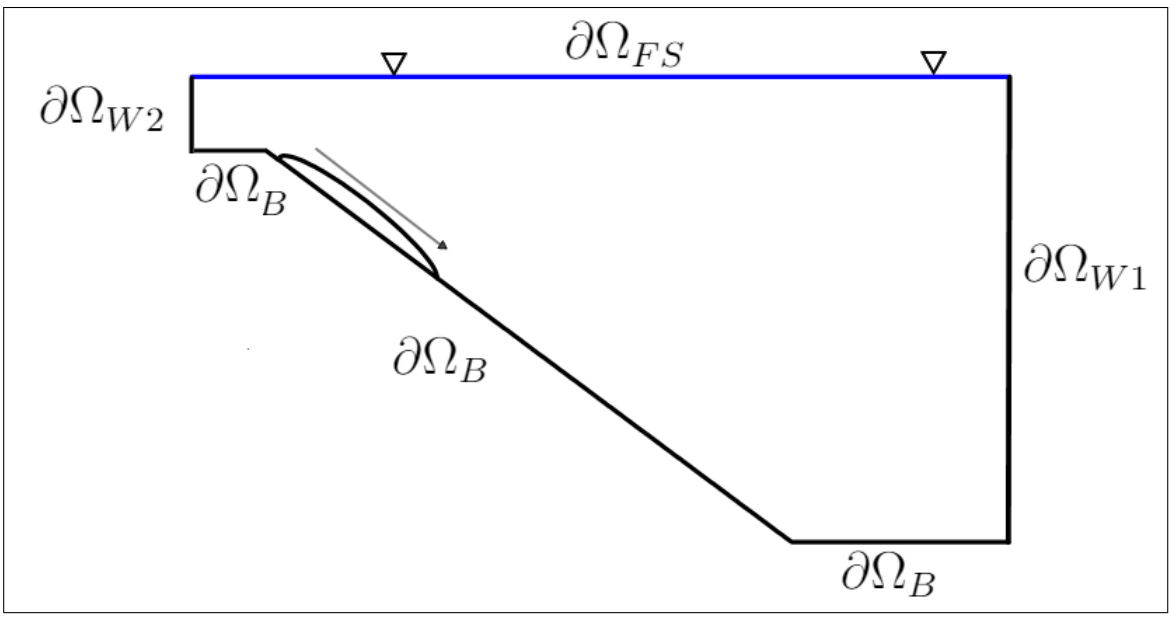

Figure 4.2. An example wave tank geometry for the construction of its BVP. The free surface, the first vertical wall, the bottom and the second vertical wall boundaries are represented by the $\partial\Omega_{FS}$, $\partial\Omega_B$, $\partial\Omega_{W1}$ and $\partial\Omega_{W2}$, respectively.

The system matrix and the RHS of Equation 4.13 have to be updated at each time level before solving the linear system of equations for the coefficient vector $\boldsymbol{\alpha}$ that is also time dependent. After obtaining the coefficient vector $\boldsymbol{\alpha}$ in each time level, the

velocity potential and the velocity at any point (x, y) can be found using

$$\phi(x,z) = \sum_{j=1}^{M} \ln r \alpha_j \tag{4.14a}$$

$$u(x,z) = \sum_{j=1}^{M} \frac{(x-x_j)}{r^2} \alpha_j \tag{4.14b}$$

$$w(x,z) = \sum_{j=1}^{M} \frac{(z-z_j)}{r^2} \alpha_j \tag{4.14c}$$

$$\text{where} \qquad r = \sqrt{(x-x_j)^2 + (z-z_j)^2}$$

4.2. Time Marching Schemes

The wave BVP desribed in the previous Chapter is formulated in spatial coordinates. At each time level, it has to be set and solved to approximate the unknown variables using Equations 4.14. The link between successive time levels is provided through the free surface boundary conditions which involve the first derivatives of the free surface elevation and velocity potential with respect to time. Their numerical integration over time provides the necessary information to solve the BVP at the next time level. The integration of the KFSBC at the ith node gives the new location of the ith node at the next time level. Since the positions of collocation nodes on the free surface and other deforming boundaries change, the system matrix in Equation 4.13 is updated accordingly. The DFSBC at ith node is also numerically integrated to find the new velocity potential of ith node at the new location. The new velocity potential is used as Dirichlet boundary condition on the right hand side of Equation 4.13.

In this numerical model, two different time marching schemes are adopted to integrate the FSBCs in full-Langragian description; the fourth order Runga-Kutta (RK O(4)) and the second order finite difference formulation of Wu *et al.*. [65]. For

the integration of the FSBCs in semi-Lagrangian description, the fourth order Adams-Bashforth (AB O(4)) predictor is utilized.

4.2.1. Numerical Integration of the FSBCs using FLD

Equations 3.10 and 3.12 are coupled FSBCs in the full-Lagrangian description (FLD). Equation 3.10 is integrated to find the locations of the free surface collocation nodes at next time level (x_i^{m+1}, z_i^{m+1}) and integration of Equation 3.12 leads to the velocity potentials (ϕ_i^{m+1}) at the free surface collocation nodes (x_i^{m+1}, z_i^{m+1}). The superscript m indicates the time level and the time-step is represented by dt in the following sections.

4.2.1.1. The Fourth Order Runga-Kutta Method. The Runga-Kutta methods are self-starting multi-step methods that are commonly used for the solution of initial value problems. The generalized implementation of RK O(4) is outlined below for a first order differential equation and its initial value.

$$\frac{dy}{dx} = f_d(x, y) \qquad y(x_0) = y_0 \tag{4.15}$$

where y is the unknown function whose value at the point x_0 and derivative with respect to x are known. Using a step size dh, $y(x_0 + dh)$ can be approximated as follows

$$y(x_0 + dh) = y(x_0) + \frac{1}{6}(k_1 + 2k_2 + 2k_3 + k_4) \tag{4.16}$$

where
$$k_1 = dh\, f_d(x_0, y_0) \tag{4.17a}$$
$$k_2 = dh\, f_d(x_0 + \frac{dh}{2}, y_0 + \frac{k_1}{2}) \tag{4.17b}$$
$$k_3 = dh\, f_d(x_0 + \frac{dh}{2}, y_0 + \frac{k_2}{2}) \tag{4.17c}$$
$$k_4 = dh\, f_d(x_0 + dh, y_0 + k_3) \tag{4.17d}$$

The FSBCs which are given in Equations 3.10 and 3.12 are integrated at the free surface collocation nodes with the RK O(4) using the step-by-step algorithm presented below

(i) $k_1 = dh\, f_d(x_0, y_0)$

(a) Find k_1s

- $(k_1^x)_i = dt\, u_i^m$
- $(k_1^z)_i = dt\, w_i^m$
- $(k_1^\phi)_i = dt\left(0.5(u_i^m\, u_i^m + w_i^m\, w_i^m) - g\, z_i^m\right)$

(ii) $k_2 = dh\, f_d(x_0 + dh/2, y_0 + k_1/2)$

(a) Update the positions of the free surface collocation nodes and their velocity potentials

- $x_i^{k_1} = x_i^m + 0.5(k_1^x)_i$
- $z_i^{k_1} = z_i^m + 0.5(k_1^z)_i$
- $\phi_i^{k_1} = \phi_i^m + 0.5(k_1^\phi)_i$

(b) Update the BBC (and other deforming BCs) for time level $t = t^m + dt/2$

(c) Update the system matrix $\mathbf{S}$ and the RHS vector $\mathbf{b}$ using (a) and (b)

(d) Solve the BVP to find $u_i^{k_1}$s and $w_i^{k_1}$s

(e) Find k_2s

- $(k_2^x)_i = dt\, u_i^{k_1}$
- $(k_2^z)_i = dt\, w_i^{k_1}$
- $(k_2^\phi)_i = dt\left(0.5(u_i^{k_1}\, u_i^{k_1} + w_i^{k_1}\, w_i^{k_1}) - g\, z_i^{k_1}\right)$

(iii) $k_3 = dh\, f_d(x_0 + dh/2, y_0 + k_2/2)$

(a) Update the positions of the free surface collocation nodes and their velocity potentials

- $x_i^{k_2} = x_i^m + 0.5(k_2^x)_i$
- $z_i^{k_2} = z_i^m + 0.5(k_2^z)_i$
- $\phi_i^{k_2} = \phi_i^m + 0.5(k_2^\phi)_i$

(b) Update the BBC (and other deforming BCs) for time level $t = t^m + dt/2$

(c) Update the system matrix $\mathbf{S}$ and the RHS vector $\mathbf{b}$ using (a) and (b)

(d) Solve the BVP to find $u_i^{k_2}$s and $w_i^{k_2}$s

(e) Find k_3s

- $(k_3^x)_i = dt\, u_i^{k_2}$
- $(k_3^z)_i = dt\, w_i^{k_2}$
- $(k_3^\phi)_i = dt\, \left(0.5(u_i^{k_2}\, u_i^{k_2} + w_i^{k_2}\, w_i^{k_2}) - g\, z_i^{k_2}\right)$

(iv) $k_4 = dh\, f_d(x_0 + dh, y_0 + k_3)$

(a) Update the positions of the free surface collocation nodes and their velocity potentials

- $x_i^{k_3} = x_i^m + (k_3^x)_i$
- $z_i^{k_3} = z_i^m + (k_3^z)_i$
- $\phi_i^{k_3} = \phi_i^m + (k_3^\phi)_i$

(b) Update the BBC (and other deforming BCs) for time level $t^{m+1} = t^m + dt$

(c) Update the system matrix $\mathbf{S}$ and the RHS vector $\mathbf{b}$ using (a) and (b)

(d) Solve the BVP to find $u_i^{k_3}$s and $w_i^{k_3}$s

(e) Find k_4s

- $(k_4^x)_i = dt\, u_i^{k_3}$
- $(k_4^z)_i = dt\, w_i^{k_3}$
- $(k_4^\phi)_i = dt\, \left(0.5(u_i^{k_3}\, u_i^{k_3} + w_i^{k_3}\, w_i^{k_3}) - g\, z_i^{k_3}\right)$

(v) $y(x_0 + dh) = y(x_0) + \frac{1}{6}(k_1 + 2k_2 + 2k_3 + k_4)$

(a) Find the positions of the free surface collocation nodes and their velocity potentials at $t^{m+1} = t^m + dt$

- $x_i^{m+1} = x_i^m + \frac{1}{6}(k_1^x + 2k_2^x + 2k_3^x + k_4^x)_i$
- $z_i^{m+1} = z_i^m + \frac{1}{6}(k_1^z + 2k_2^z + 2k_3^z + k_4^z)_i$
- $\phi_i^{m+1} = \phi_i^m + \frac{1}{6}(k_1^\phi + 2k_2^\phi + 2k_3^\phi + k_4^\phi)_i$

(b) Update the system matrix $\mathbf{S}$ and the RHS vector $\mathbf{b}$ using x_i^{m+1}s, z_i^{m+1}s, ϕ_i^{m+1}s and the BBC (and other deforming BCs) at $t^{m+1} = t^m + dt$

(c) Solve the BVP to find u^{m+1}s and w^{m+1}s

(vi) The model can proceed to the next time level

In the algorithm above, superscript k indicates that the variable is updated using the k.

4.2.1.2. The Finite Difference Formulation of Wu *et al.* A second order centered difference formula can be used for the discretization of the FSBCs in the time domain as

$$\phi_i^{m+1} = \phi_i^{m-1} + 2dt\left(\frac{1}{2} \mid \nabla\phi_i^m \mid^2 - g\, z_i^m\right) \tag{4.18}$$

and,

$$x_i^{m+1} = x_i^{m-1} + 2dt\, u_i^m \tag{4.19a}$$

$$z_i^{m+1} = z_i^{m-1} + 2dt\, w_i^m \tag{4.19b}$$

The position of the free surface collocation nodes at the next time level is given by x_i^{m+1} and z_i^{m+1}. ϕ_i^{m+1} is used as Dirichlet boundary condition for the free surface as was done in the previous section. After updating the positions of the collocation nodes on deforming boundaries and their corresponding RHSs for the time level $t^{m+1} = t^m + dt$, the BVP can be solved to find the w_i^{m+1} and u_i^{m+1} at the collocation nodes (x_i^{m+1}, z_i^{m+1}). In the study of Wu *et al* [65], the Crank-Nicolson formula is suggested for the modification of the positions of the free surface collocation nodes. The application of the Crank-Nicolson formula is as follows

$$x_i^{m+1} = x_i^m + \frac{dt}{2}\left(u_i^m + u_i^{m+1}\right) \tag{4.20a}$$

$$z_i^{m+1} = z_i^m + \frac{dt}{2}\left(w_i^m + w_i^{m+1}\right) \tag{4.20b}$$

Better numerical stability was achieved by the use of Equation 4.20 [65]. Solving the BVP again using the locations given by Equations 4.20 is not necessary according to Wu *et al* [65]. They suggested that the velocities found at the modified locations given by Equations 4.20 do not differ considerably from the velocities at the locations found by Equations 4.19. Thus, after modifying the location of collocation nodes using Equations 4.20, the numerical model can proceed to next time level without modifying the velocities.

4.2.2. Numerical Integration of the FSBCs using SLD

The FSBCs in semi-Lagrangian form are given in Equations 3.14 and 3.7 which are two coupled equations defined at fixed x-coordinates. In the SLD, only vertical positions of the free surface collocation nodes are updated. The integration of Equation 3.12 gives the free surface displacement at the next time level (η_i^{m+1}). The velocity potentials (ϕ_i^{m+1}) at the free surface collocation nodes (x_i, η_i^{m+1}) can be found by the integration of Equation 3.14.

4.2.2.1. The Fourth Order Adams-Bashforth Predictor. The implementation of the AB O(4) by the numerical integration of the differential equations is as follows,

$$\frac{dy}{dx} = f_d(x, y) \tag{4.21}$$

where f_d is the derivative of an unknown function. The y^{m+1} can be predicted in the following way,

$$y^{m+1} = y^m + \frac{dh}{24}(55{f_d}^m - 59{f_d}^{m-1} + 37{f_d}^{m-2} - 9{f_d}^{m-3}) \tag{4.22}$$

$$\text{where} \qquad {f_d}^m = f_d(x^m, y^m) \tag{4.23a}$$

$${f_d}^{m-1} = f_d(x^{m-1}, y^{m-1}) \tag{4.23b}$$

$${f_d}^{m-2} = f_d(x^{m-2}, y^{m-2}) \tag{4.23c}$$

$${f_d}^{m-3} = f_d(x^{m-3}, y^{m-3}) \tag{4.23d}$$

The velocity potentials ϕ_i^{m+1} and the free surface displacements η_i^{m+1} can be found using AB O(4) as

$$\phi_i^{m+1} = \phi_i^m + \frac{dt}{24}\left(55\left(\frac{\partial\phi}{\partial t}\right)_i^m - 59\left(\frac{\partial\phi}{\partial t}\right)_i^{m-1} + 37\left(\frac{\partial\phi}{\partial t}\right)_i^{m-2} - 9\left(\frac{\partial\phi}{\partial t}\right)_i^{m-3}\right) \tag{4.24a}$$

$$\eta_i^{m+1} = \eta_i^m + \frac{dt}{24}\left(55\left(\frac{\partial\eta}{\partial t}\right)_i^m - 59\left(\frac{\partial\eta}{\partial t}\right)_i^{m-1} + 37\left(\frac{\partial\eta}{\partial t}\right)_i^{m-2} - 9\left(\frac{\partial\eta}{\partial t}\right)_i^{m-3}\right) \tag{4.24b}$$

$$\text{where} \qquad \left(\frac{\partial\phi}{\partial t}\right)_i^m = -\frac{1}{2} \mid \nabla\phi_i^m \mid^2 - g\,\eta_i^m + w_i^m\left(\frac{\partial\eta}{\partial t}\right)_i^m$$

$$\text{and} \qquad \left(\frac{\partial\eta}{\partial t}\right)_i^m = w_i^m - u_i^m\left(\frac{\partial\eta}{\partial x}\right)_i^m$$

After updating the necessary information on the free surface and the other boundaries as done in the FLD, the BVP is solved to find the velocities (u_i^{m+1}, w_i^{m+1}) on the free surface collocation nodes (x_i, η_i^{m+1}). Since the horizontal spacing between the free surface collocation nodes is constant, the centered finite difference formula of the second order can be used for the spatial derivative of the free surface displacement η as follows

$$\left(\frac{\partial\eta}{\partial x}\right)_i^m = \begin{cases} \frac{-\eta_{i+2}^m + 4\eta_{i+1}^m - 3\eta_i^m}{2dx}, & \text{if } i = 1 \\ \frac{\eta_{i+1}^m - \eta_{i-1}^m}{2dx}, & \text{if } i = 2, ..., N_{FS} - 1 \\ \frac{\eta_{i-2}^m - 4\eta_{i-1}^m + 3\eta_i^m}{2dx}, & \text{if } i = N_{FS} \end{cases} \tag{4.25}$$

where the dx is the nodal spacing and the N_{FS} indicates the number of collocation nodes on the free surface. The use of Equation 4.25 is computatinally efficient as it does not necessitate a matrix inversion. In addition, it is accurate in the vicinity of the corners where the free surface and the solid boundaries intersect. Note that the integration with AB O(4) require 4 previous values of the integrand. To able to initiate

the model, information for the time levels $m = 0, -1, -2, -3$ is provided as

$$\phi^0 = \phi^{-1} = \phi^{-2} = \phi^{-3} = 0$$
$$u^0 = u^{-1} = u^{-2} = u^{-3} = 0$$
$$w^0 = w^{-1} = w^{-2} = w^{-3} = 0$$
$$\eta^0 = \eta^{-1} = \eta^{-2} = \eta^{-3} = 0$$

5. EXPERIMENTS AND RESULTS

5.1. The Experiments of Hammack

Hammack's experiments, in which waves were generated by the vertical motion of the horizontal wave generator in a constant depth wave tank, are simulated using the numerical model. The experiment has been described in the Section 2.2 and further explanation of the experimental set up can be found in [30]. The motion of the bed section that is illustrated in Figure 5.1 is given by Hammack as,

$$h(x,t) = h_0 - \zeta_0(1 - e^{-\beta t})\,\mathcal{H}(b^2 - x^2) \tag{5.1}$$

where ζ_0 is the total maximum displacement of the bed section of length b. The Heaviside step function and the undisturbed water depth are represented by $\mathcal{H}$ and h_0, respectively. The α in Equation 5.1 is found by

$$\beta = 11/t_c \tag{5.2}$$

where t_c is the characteristic time for the motion of the bed section and is used for the classification of the motion.

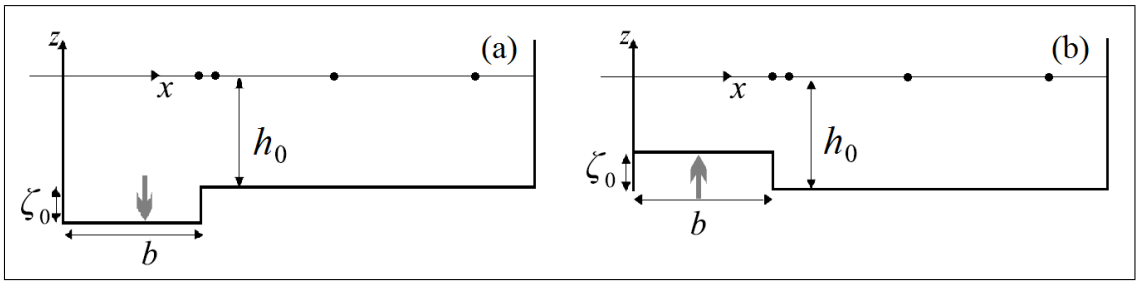

Figure 5.1. Illustration of bed deformation in Hammack's Experiments:(a) Negative bed deformation,(b) Positive bed deformation. Dots represent the wave gauges that are 0, 20, 180 and 400 water depths away from the wave generator

The results presented in the following two sections are obtained in the numerical model using RK O(4) for the integration of the nonlinear FSBCs in FLD. The results obtained using the finite difference formulation of Wu *et al.* [65] are given in the Appendix A. The SLD of the free surface is also utilized for the modelling of the Hammack's experiment. The results for the SLD are given in the Appendix B. The model will be hereinafter referred to as FNLFLD model, when the FLD of the free surface is utilized in the numerical model for the fully nonlinear free surface. Similarly, the FNLSLD model will be presenting the model in which the SLD of the fully nonlinear free surface is used.

In the experiment of Hammack [30], the free surface elevations, which were given as time series in non-dimensional parameters, were sampled at four different gauges that have fixed x-locations. Since the water particles are free to move in all directions using the FLD, the free surface elevations at fixed x-locations are obtained in the FNLFLD model by the interpolation of the free surface using Gaussian RBF. The interpolation procedure is given in the Appendix C.1.

5.1.1. Impulsive Bed Down-thrust

The exponential bed deformation given by Equation 5.1 is simulated for the negative deformation case using the FNLFLD model. The time series of the free surface elevations were given by Hammack for the non-dimensional parameters $\zeta_0/h_0 = -0.1$, $b/h_0 = 12.2$ and $t_c\sqrt{gh}/b = 0.093$. In the FNLFLD model, the case that has a still water level $h_0 = 0.5\,m$ is modelled with an initial nodal spacing of $dx = 0.5m$ both on the free surface and on the bottom. The time step is set to $dt = 0.01\,s$ for the integration of the FSBCs using RK O(4). In addition, the number of collocation nodes on each fully reflecting wall is equal to 11 with a vertical nodal spacing of $dz = 0.05\,m$. The Courant number that is calculated using the initial nodal spacing on the free surface is approximately equal to 0.045. The simulations are stopped before any reflection occurs from the vertical wall located at the right end of the domain.

The free surface elevations captured in the FNLFLD model and in the PBBM model of Hammack are given in Figure 5.2 along with the measured free surface elevations in the experiment [30]. The PBBM model is not capable of generating waves due to bottom motion, therefore the time series of the free surface elevations of the PBBM model is absent at the first gauge which is located at the right end of the wave generator ($(x-b)/h_0 = 0$). Hammack initiated the PBBM model using the results of the linear theory at the second gauge which is located 20 water depth away from the wave generator ($(x-b)/h_0 = 20$). The time series results in the Figures 5.2 a and 5.2 b shows the accuracy of the FNLFLD model by the generation of waves due to the exponential bed deformation. A large negative leading wave whose amplitude is approximately equal to the half of the maximum bed displacement is produced. The train of shorter oscillatory waves that follows the leading wave is also generated. At gauge b, the linear theory solution of Hammack predicts the wave evolution accurately, thus it can be used in the model that can not generate waves by bottom motion.

At gauge c ($(x-b)/h_0 = 180$), the leading wave takes on a smooth triangular shape and the amplitudes of the oscillatory waves increase. After further propagation, the frontal slope and the amplitude of the leading wave decreases as is evident in Figure 5.2 d. At $(x-b)/h_0 = 180$ and $(x-b)/h_0 = 400$, the PBBM model and the present model predict the general arrangement of wave evolution well, however the speed and the amplitude of the waves in the experiment differ considerably from the models. Hammack suggested that this is due to the viscous effects that are not taken into account by the PBBM model [30]. During propagation, the energy dissipation due to viscosity shortens the amplitudes and the wall shear stresses between the water and the sides of the channel decrease the speed of the leading wave and the oscillatory waves [31]. Thus, the rightward shift of the experiment results increases between the gauges c and d. The results of the FNLFLD model and the PBBM model agree closely for the leading wave at the gauges c and d, however they differ noticeably for the oscillatory waves. Hammack and Segur indicated that these trailing oscillatory waves are dispersive [31], therefore the deviation between the two models may be related to the dispersion characteristics of the PBBM equation which is a KdV-type of equation with improved dispersion properties [66].

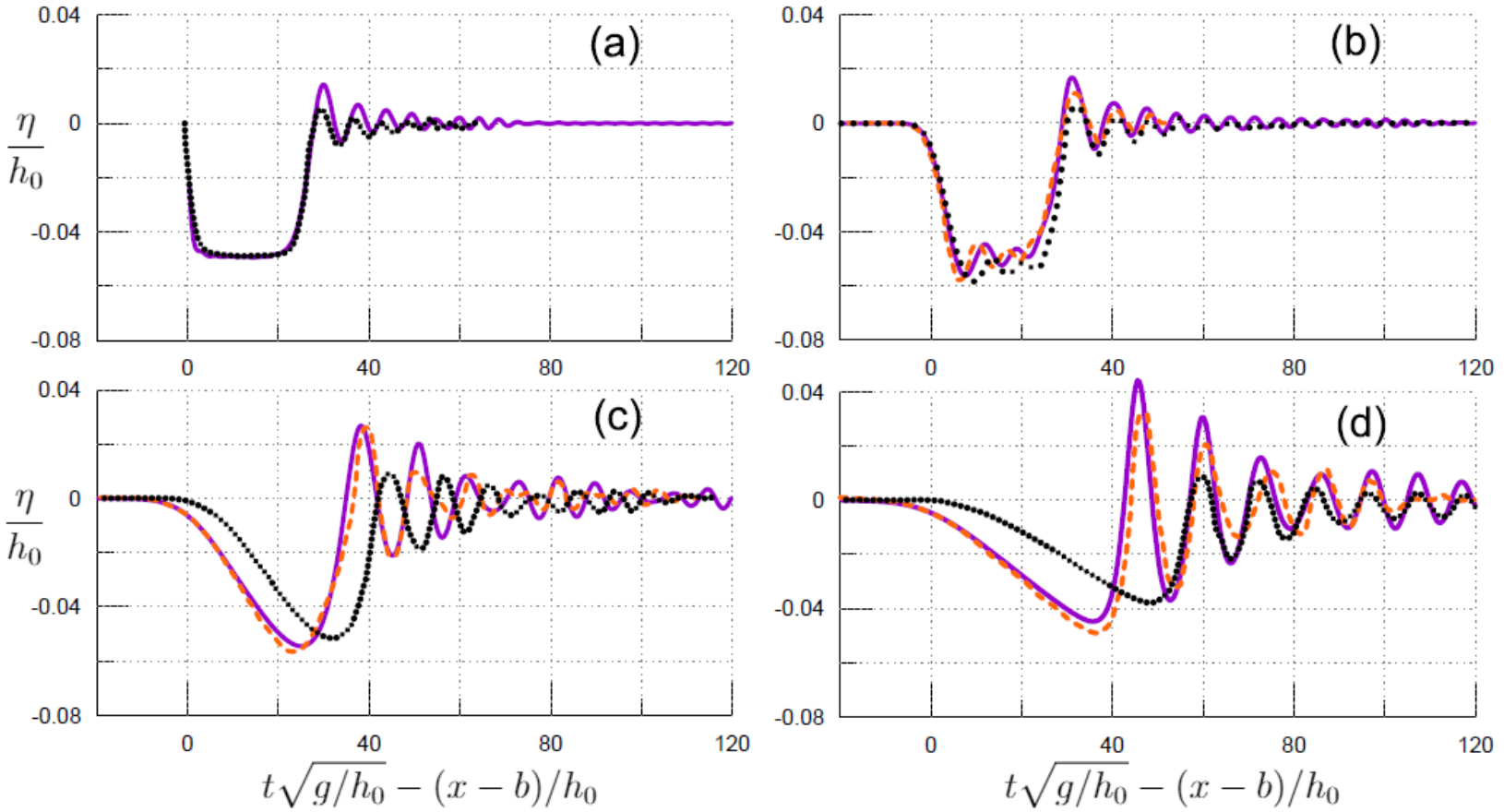

Figure 5.2. Time series of the free surface elevations of the FNLFLD (solid line), the KdV-type (PBBM) model of Hammack (dashed line) and the experiment of Hammack (dotted line) [30] at gauges (a) $(x-b)/h_0 = 0$, (b)$(x-b)/h_0 = 20$, (c)$(x-b)/h_0 = 180$ and (d)$(x-b)/h_0 = 400$.

The results of fully nonlinear, highly dispersive Boussinesq (FNHDB) model of Fuhrman and Madsen at gauges c and d are included in Figure 5.3 to compare with the FNLFLD model. As can be seen in Figure 5.3, the results of the both models agree well in the region of the leading wave as well as in the region of the dispersive oscillatory waves.

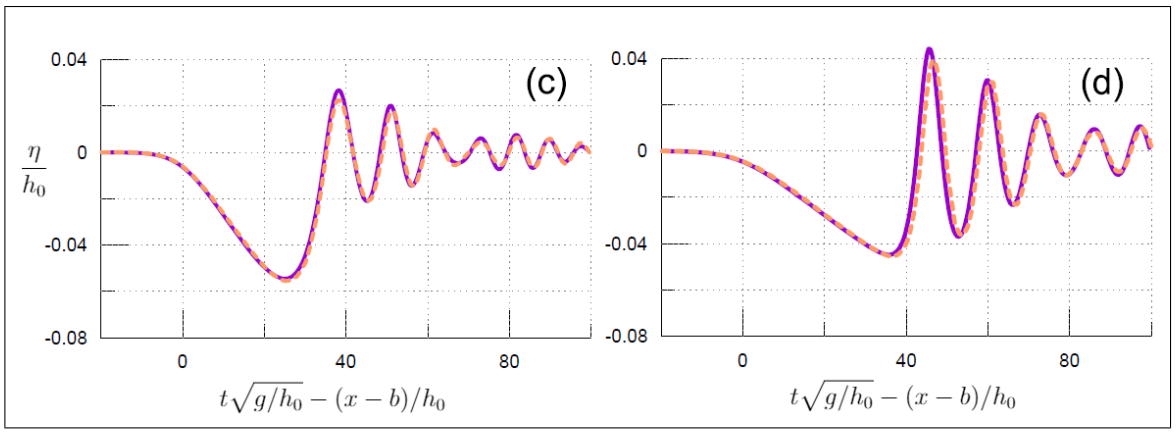

Figure 5.3. Time series of the free surface elevations of the FNLFLD (solid line) and the FNHDB model of Fuhrman and Madsen (dashed line) [43] at gauges (c)$(x-b)/h_0 = 180$ and (d)$(x-b)/h_0 = 400$.

Hammack defined two Ursell numbers for the leading wave part and the oscillatory waves part to explain the effects of non-linearity [30]. According to the results of the experiment, the Ursell number of the leading front increases considerably from 3 to 55 during propagation from the source to the last gauge whereas the Ursell number calculated from the properties of the oscillatory waves part does not vary noticeably and is equal to 2 at the last gauge. Thus, nonlinear effects becomes more important for the leading wave, while for the trailing part nonlinear and linear effects stay about equal [30]. The reason why the results of the FNLFLD model agree better in the region of leading wave with the FNHDB model of Fuhrman and Madsen than with the PBBM model of Hammack may be the domination of the nonlinear effects in this region. While on the other hand the governing equation of the PBBM is based on the assumption that nonlinear effects are approximately equal to linear effects [30].

5.1.2. Impulsive Bed Up-thrust

The positive bottom movement that was investigated by Hammack has the non-dimensional parameters $\zeta_0/h_0 = 0.1$, $b/h_0 = 12.2$ and $t_c\sqrt{gh}/b = 0.148$. The exponential motion is described again with Equation 5.1 and is illustrated in Figure 5.1 b. The case considered in the FNLFLD model has an undisturbed water level $h_0 = 0.5\,m$ as before. The nodal spacing and the time step are chosen to be same as in the simulation of the bed down-thrust.

The free surface elevations obtained from the FNLFLD model along with those obtained from the PBBM model of Hammack and those measured in his experiment are given as time series in Figure 5.4 for the impulsive bed up-thrust. Figures 5.4 a and 5.4 b show the free surface elevations near the generation zone at $(x-b)/h_0 = 0$ and $(x-b)/h_0 = 20$. The result of the PBBM model is again missing at the first gauge since the analytical linear solution of Hammack at gauge b is given to the model as initial data as in the case of down-thrust. The impulsive bed up-thrust generates a large positive wave which is followed by smaller oscillatory waves in the experiment and in the FNLFLD model. The initial amplitude of the positive wave is about the half of the maximum displacement of the wave generator. The results of the experiment at the first two gauges match the results obtained from the FNLFLD model closely except for an amplitude difference which is within 8 percent of the experiment.

In the far-field gauges c ($(x-b)./h_0 = 180$) and d ($(x-b)./h_0 = 400$), the positive wave starts to evolve into separate waves which are ordered by their amplitudes. The dispersive oscillatory waves which are smaller in magnitude follows the larger waves. As can be seen from Figure 5.4 c and 5.4 d, the overall trend of wave evolution in the experiment is accurately modelled by both the FNLFLD model and the PBBM model. The time shift and the amplitude difference between the results of the experiment and the models is associated with the effects of the viscosity [30]. This time shift and amplitude difference increases during propagation between the third and fourth wave gauges as in the simulation of the bed down-thrust.

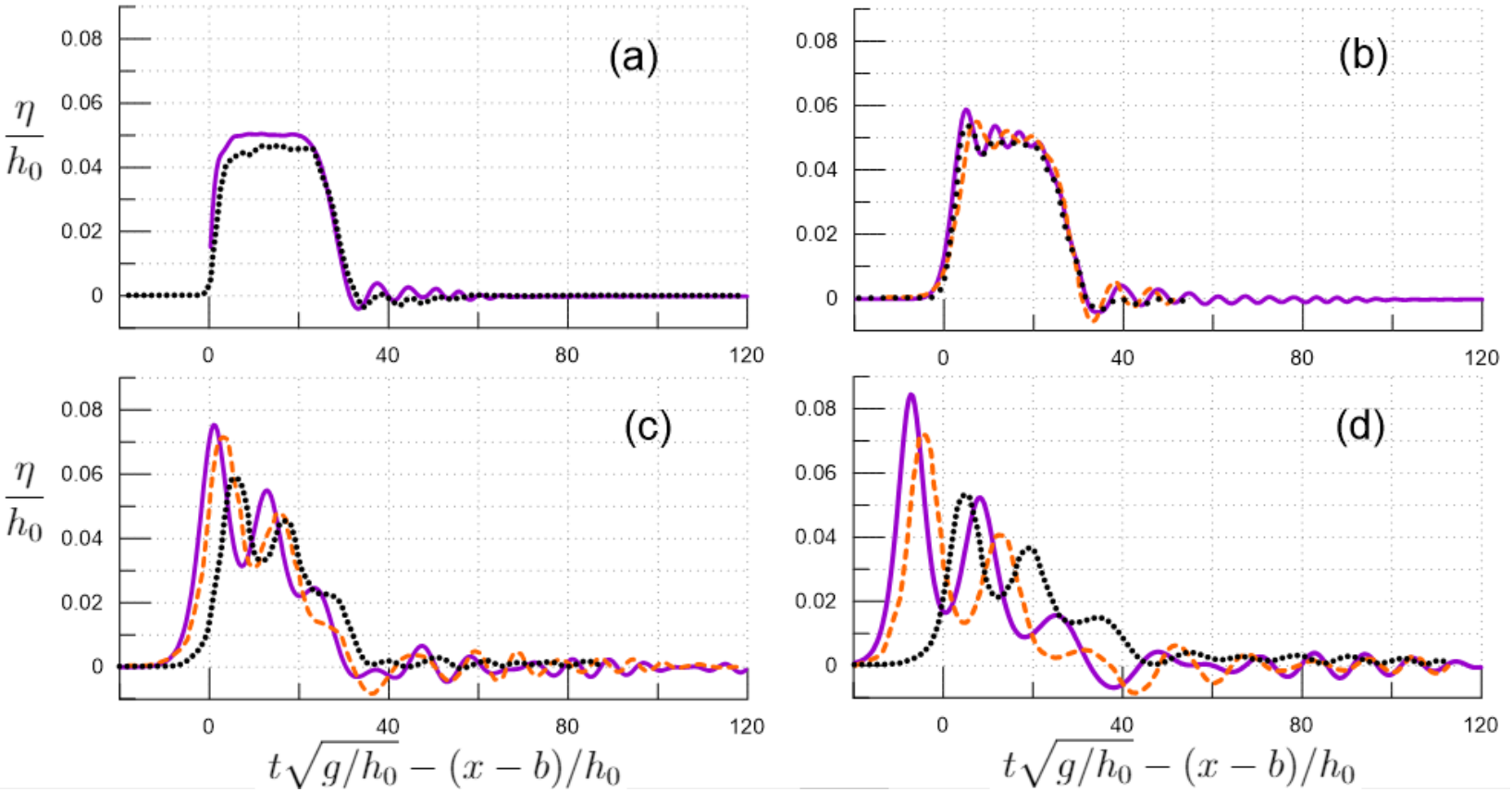

Figure 5.4. Time series of the free surface elevations of the FNLFLD model (solid line), the KdV-type (PBBM) model of Hammack (dashed line) and the experiment of Hammack (dotted line) [30] at gauges (a) $(x-b)/h_0 = 0$, (b)$(x-b)/h_0 = 20$, (c)$(x-b)/h_0 = 180$ and (d)$(x-b)/h_0 = 400$.

Between two gauges whose time series data given in the Figures 5.4 c and 5.4 d, the amplitude of the leading wave in the model of Hammack does not change, whereas it is increasing in the FNLFLD model as in the model of Fuhrman and Madsen [43] (see Figure D.1) and in the model of Tijandra and Pudjaprasetya [45] (see Figure D.2). According to the measurements of the experiment, the Ursell number that is found by Hammack increases from 0.7 (at the generation zone) to 3 at the last gauge which is located 400 water depths away from the generation zone [30]. The increase in non-linearty could not be modeled using the PBBM equation.

The relatively shorter time shift between the FNLFLD model and the PBBM model of Hammack at gauges c and d is associated with the amplitude dispersion. Since the amplitudes of the leading waves in the FNLFLD model are larger, it is expected that these waves reach the gauges c and d earlier than the ones in the PBBM model of Hammack. This time shift is also observed in the study of Fuhrman and Madsen who stated that the waves in the PBBM model undergo limited amplitude dispersion [43].

Further propagation of the waves in the numerical wave tank which is much longer than the tank in the experiment leads to the full evolution of solitary waves as can be seen in Figure 5.5. The evolution of the solitary waves confirms the suggestion of Hammack and Segur who indicated that solitary waves are expected to evolve after sufficient propagation when the net volume of the water displaced by the bottom motion is positive [25]. For the case, the separation distance found by Hammack and Segur using the asymptotic solution of the KdV equation is 700 water depths from the generation zone. In addition to that, the number of solitary waves was predicted to be 3. However, the separation of the third solitary wave is not observed in the numerical wave tank of the FNLFLD model even after 2500 water depths of propagation.

The free surface profiles obtained from the FNHDB model of Fuhrman and Madsen at $t\sqrt{g/h_0} = 2375$ is also included in Figure 5.5. According to given results of the Boussinesq model [43], the first solitary wave is located at 2470.82 water depth away from the generation zone ($x/h_0 = 2470.82$) with a height of 0.0809 water depth ($H/h_0 =$

0.0809), while the second one is located at $x/h_0 = 2419.8$ having $H/h_0 = 0.0442$ height. The height and the location of the first solitary wave in the FNLFLD model at $t\sqrt{g/h_0} = 2375$ is found as $H/h_0 = 0.0822433$ and $x/h_0 = 2472.25$,respectively. At the same instant, the second wave located at $x/h_0 = 2421.9$ is $H/h_0 = 0.0469807$ in height. The difference in the heights of the first solitary waves of both models is 1.6 percent of the height of the first solitary wave of the FNHDB model, whereas the difference in the second waves is about 6.3 percent of the wave height that is oberved in the FNHDB model. The time shift between the second waves of the two models is larger than the time shift of their leading waves as the amplitude dispersion that the waves undergo is proportionally to their height.

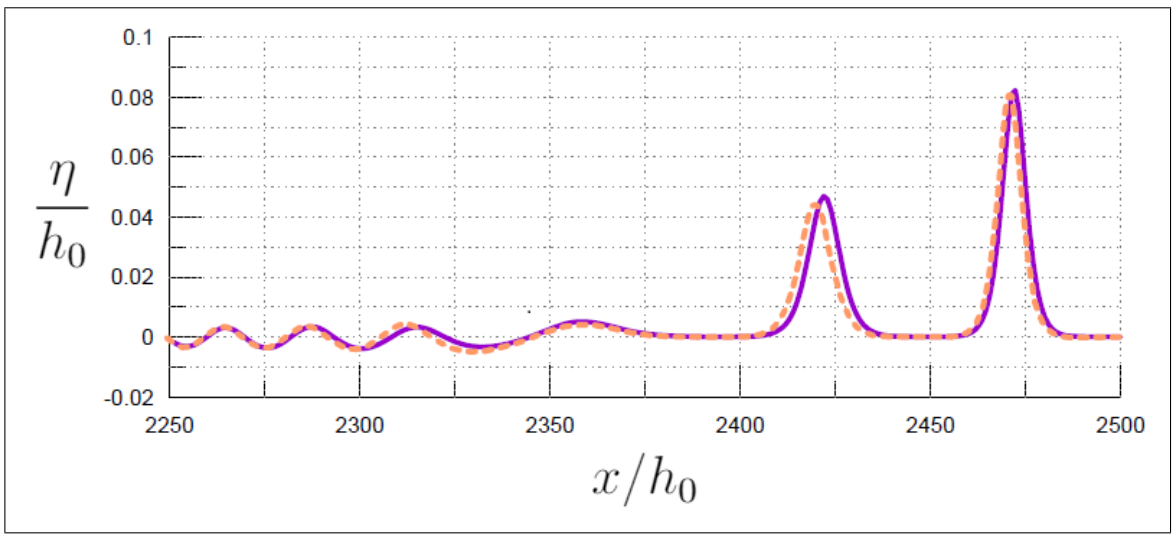

Figure 5.5. The free surface profiles in the FNLFLD (solid line) and in the FNHDB model of Fuhrman and Madsen (dashed line) [43] at $t\sqrt{g/h_0} = 2375$.

The full evolution of the solitary waves is also observed in FNLSLD model. The related free surface profile is given in Figure B.3. The leading wave found in the FNLSLD model has a height of $H/h_0 = 0.080466$ at $x/h_0 = 2471.2$, whereas the second wave is located at $x/h_0 = 2421.8$ having a height of $H/h_0 = 0.04632$. The free surface profiles observed after 2500 water depths of propagation in the FNLFLD model and in FNLSLD model are almost the same except an amplitude difference of the 2 percent at the leading solitary waves. Thus only time shift observed between the two models is at the leading solitary waves. This may be due to the loss of nonlinearity

that results from neglecting the horizontal displacement in the SLD of the free surface.

It has to be noted that the free surface profile at $t\sqrt{g/h_0} = 2375$ obtained using the formulation of Wu *et al.* for the integration of the FSBC deviates greatly from the results given in Figure 5.5 even with a timestep that is ten times smaller than the timestep utilized in RK O(4), although two time integration techniques for FLD lead to same results at the wave gauges.

Another newsworthy point observed from the solitary waves in the FNLFLD model is that their shapes closely match the solitary wave profile [67] given by

$$\eta = H \operatorname{sech}^2\left(\sqrt{\frac{3H}{4h_0^3}}(x - x_0)\right) \tag{5.3}$$

where x_0 is the center of the wave. The solitary waves given by Equation 5.3 is plotted in Figure 5.6 using the amplitudes and the locations that are found in the FNLFLD model along with the free surface profile produced by the model.

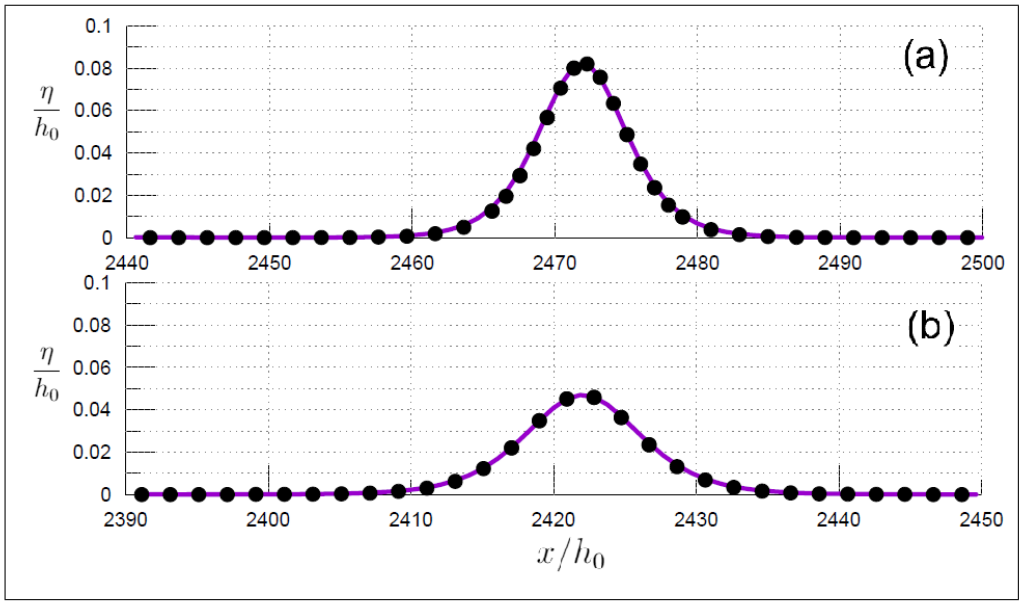

Figure 5.6. The free surface profiles of the solitary waves at $t\sqrt{g/h_0} = 2375$ found by the FNLFLD model (solid line) and by Equation 5.3 (dots) with: (a)$H/h_0 = 0.0822433$ and $x/h_0 = 2472.25$, (b) $H/h_0 = 0.0469807$ and $x/h_0 = 2421.9$.

5.2. The Numerical Submarine Landslide Experiment of Lynett and Liu

A numerical experiment was conducted by Lynett and Liu [41] to determine the limitations of the depth-integrated fully nonlinear, weakly dispersive Boussinesq-type (FNWDB) model by modeling the waves generated by a submerged landslide. The time dependent water depth given by Lynett and Liu [41] and sunsequently corrected by Fuhrman and Madsen [43] is as follows

$$h(x,t) = x\tan\theta - h'(x,t) \tag{5.4}$$

where the $x\tan\theta$ stands for the sloping bottom having an angle θ and the $h'(x,t)$ describes the motion of the sliding mass on the sloping bottom. The time variant part of the water depth is computed from

$$h'(x,t) = \frac{\triangle h}{4}\Big[1+\tanh\Big(2(x-x_l(t))\cos\theta\Big)\Big]\Big[1-\tanh\Big(2(x-x_r(t))\cos\theta\Big)\Big] \tag{5.5}$$

where $\triangle h$ is the maximum vertical height of the sliding mass. The x_l and x_r are the horizontal positions of inflection points on the back side and on the front side, respectively. The points of inflection are calculated as

$$x_l = x_c - \frac{b}{2}\cos\theta \tag{5.6a}$$

$$x_r = x_c + \frac{b}{2}\cos\theta \tag{5.6b}$$

where the x_c and b are the horizontal position of the center and the length between inflection points of the sliding mass parallel to the slope, respectively. The motion of the center is given by

$$x_c(t) = x_0 + S(t)\cos\theta \tag{5.7}$$

where x_0 is the initial horizontal position of the sliding mass center. S(t) describes the motion of the sliding mass parallel to the slope as

$$S(t) = S_0 \ln\left(\cosh\left(\frac{t}{t_0}\right)\right) \tag{5.8}$$

where t_0 is the characteristic duration of the slide. Detailed explanations of the parameters can be found in [37].

The case that has the parameter $S_0 = 4.712\,m$, $x_0 = 2.379\,m$, $t_0 = 3.713\,s$, $\triangle h = 0.05\,m$, $\theta = 6^\circ$ and $b = 1\,m$ is simulated using the present numerical model with the FLD of the free surface (the FNLFLD model). The rigid body motion of the landslide with given parameters is illustrated in Figure 5.7 with the snapshots of the bottom at four different time levels. Note that the run-up and run-down calculations have to be included for the case, thus the utilization of the SLD of the free surface is not possible.

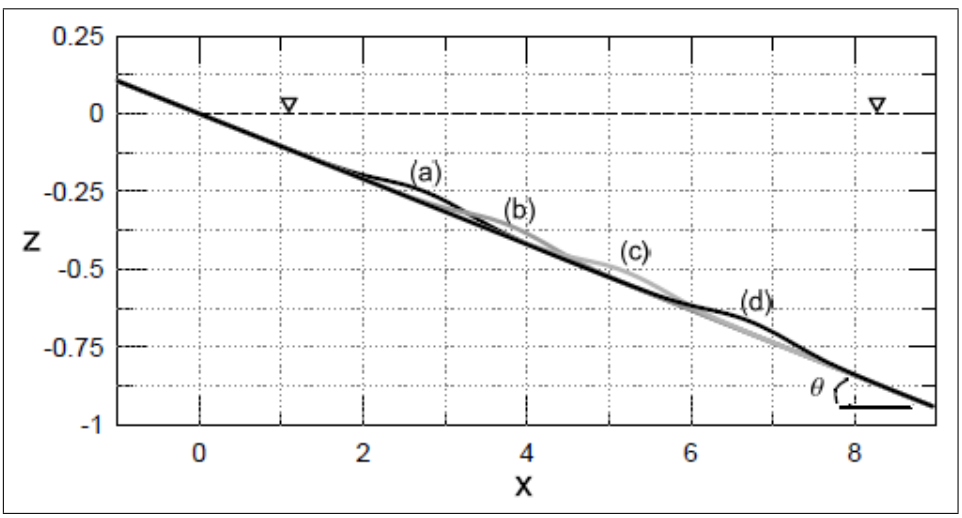

Figure 5.7. The position of the sliding mass at four different time level:(a) $t = 1.51\,s$, (b) $t = 3.00\,s$, (c) $t = 4.51\,s$ and (d) $t = 5.86\,s$.

The solution domain in the simulation ends at $x = 30\,m$ where a fully reflecting wall is placed. The simulation ends before any reflection from the wall occurs. For the integration of the free surface, the formulation presented by Wu [65] is used. The

horizontal spacing on the free surface and the bottom is chosen to be $dx = 0.05\,m$, while the vertical nodal spacing on the wall is $dz = 0.05\,m$. The time step dt is equal to $0.001\,s$. Since the water depth is given as a function of time, the BBC given in Equation 3.17 is utilized.

The node placement for the landslide is sketched in Figure 5.8 where the nodal spacing is not the same as in the simulation for the scaling purposes of the Figure. The locations of the source points parallel to the free surface and the bottom updated at each time level to keep the offset distance constant. The only additional requirement for the run-up calculations is to extend the sloping bottom on which the collocation nodes of the free surface can run up. The same BBC is applied at the collocation nodes located on the extended part of the slope. The first collocation node of the free surface is placed on the sloping bottom.

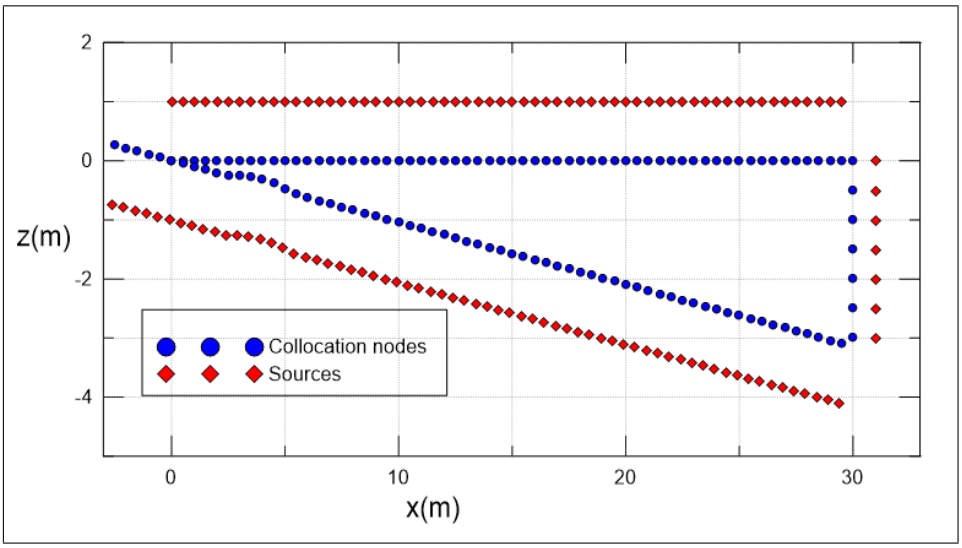

Figure 5.8. Illustration of the initial node placement for the numerical submarine landslide experiment of Lynett and Liu. The circles represents collocation nodes and the rotated square stands for the sources.

In the study of Lynett and Liu, the landslide is simulated with the FNWDB model and the fully nonlinear and dispersive BEM (FNDBEM) model of Grilli and Watts [37]. The free surface profiles obtained by both models are given at four different time levels in Figure 5.9 along with the profiles captured by the present FNLFLD model.

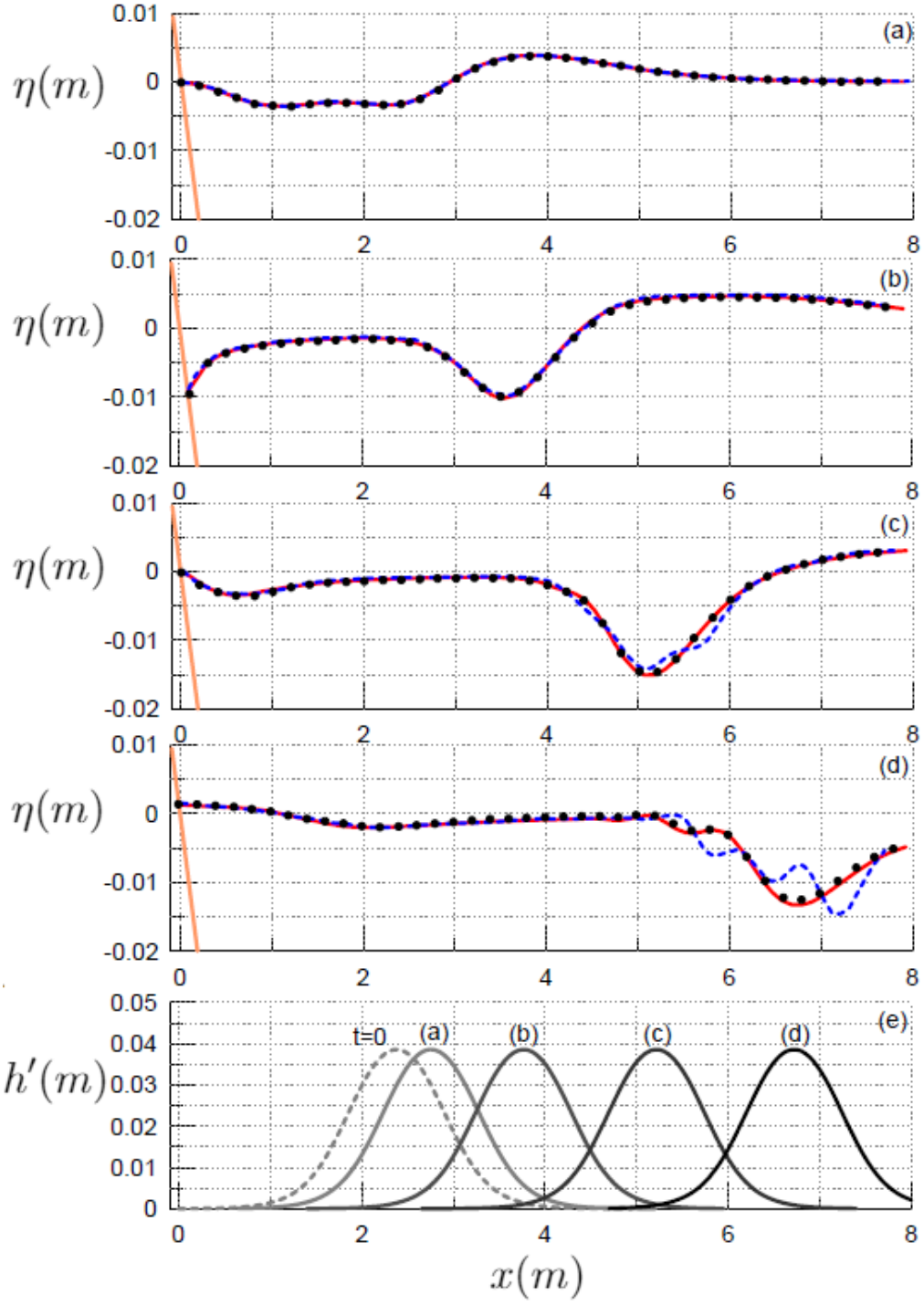

Figure 5.9. The free surface profiles obtained using the FNLFLD model (solid line), using the FNDBEM model of Grilli and Watts (dots) [37] and using the FNWDB model of Lynett and Liu (dashed line) [41] at (a) t=1.51 s,(b) t=3.00 s,(c) t=4.51 s and (d) t=5.86 s. (e) The horizontal position of the sliding mass at (a),(b),(c) and (d).

In Figures 5.9 a and 5.9 b, the results of the three models match properly. The results of the FNDBEM model and the FNLFLD model agree well at later times as can be seen in the Figures 5.9 c and 5.9 d. However, the free surface elevations obtained from the FNWDB model deviates from those obtained from the other two models at (c) $t = 4.51\,s$ and (d) $t = 5.86\,s$ above the sliding mass whose horizontal position is given in Figure 5.9 e. According to Lynett and Liu [41], these deviations are associated with the incapability of the depth integrated model to simulate horizontal flow motion that is generated by the horizontal movement of the land slide. On the other hand, this case could be reproduced accurately by the FNHDB model of Fuhrman and Madsen [43] which has impoved dispersion characteristics.

5.3. The Landslide Experiment of Watts *et al.*

Watts *et al.* performed a laboratory experiment to examine the water waves generated by the motion of a sliding semi-ellipse on a uniform slope [38]. The experiment was carried out at 1:1000 scale using the geometry that is depicted in Figure 5.10. The detailed explanation of the tank and utilized apparatus can be found in [38]. The semi-ellipse with a length B has a maximum thickness T located on a slope of θ angle. The center of the ellipse is intially placed at $x = x_0$ and the initial submergence is equal to d_0. The x_g stands for the initial horizontal position of the midpoint of the ellipse on its surface. Once the ellipse starts its motion on the slope, time series of the free surface elevations were collected at four different wave gauges that were placed at $x = x_g$, $x = x_g + 300\,m$, $x = x_g + 600\,m$ and $x = x_g + 900\,m$ in the prototype scale .

The initial horizontal position of the ellipse center can be found as

$$x_0 = \frac{d_0 + T\cos\theta}{\sin\theta} \tag{5.9}$$

The initial position of the ellipse midpoint can be given as

$$x_g = x_0 + T\sin\theta \tag{5.10}$$

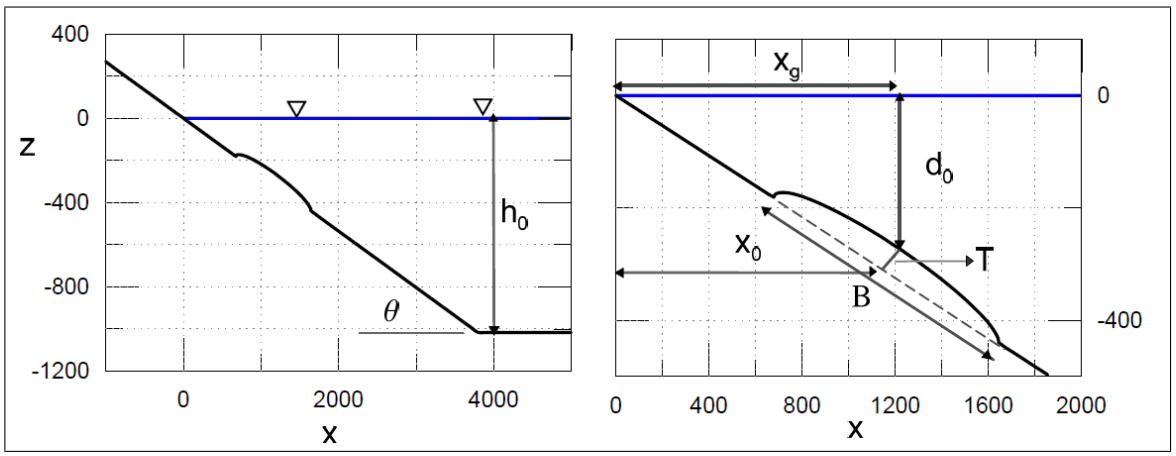

Figure 5.10. The initial set up of the submarine landslide experiment of Watts *et al.* in prototype scale [38]. (b) zoomed version of (a).

The motion of the slide parallel to the slope is again described by

$$S(t) = S_0 \ln\left(\cosh\left(\frac{t}{t_0}\right)\right) \tag{5.8}$$

The velocity of the sliding mass parallel to the slope read

$$\dot{S}(t) = u_t \tanh\left(\frac{t}{t_0}\right) \tag{5.11}$$

where u_t is the terminal velocity that the sliding mass can reach.

5.3.1. The Numerical Simulation of Grilli *et al.*

The experiment detailed in the previous section was simulated using the FNDBEM model of Grilli and Watts [37] using the computational domain that is given in Figure 5.11 [39]. Note that an additional shelf exists as part of the domain whereas it does not in the experiment. The water depth over the shelf is set to $h_1 = 0.075h_0$ with a length of $l_1 = h_1/(2\tan(\theta))$ so that the water volume over the shelf is equal to the water volume in the triangular section that exists in the laboratory experiment. At the left extremity of the computational domain where the shelf is located, Grilli *et al.*

applied the no-flux boundary condition. Additionally, a snake absorbing piston was added to the right end of the domain ($x = x_{end}$) to absorb the waves that propagate in x-direction [39].

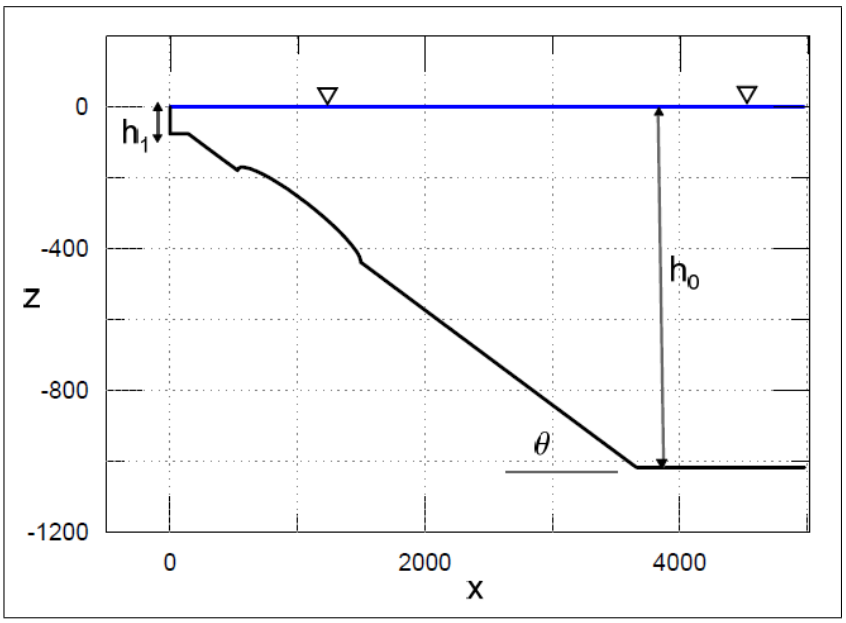

Figure 5.11. The computational domain utilized by Grilli *et al.* [39] for the simulation of the experiment of Watts *et al.* [38].

Grilli *et al.* utilized a sech^2 curve to describe the sliding ellipse to eliminate the singularities that are created in the BEM model at the corners where the ellipse and the slope intersect. This is given as [39]

$$\xi = \frac{T}{1-\epsilon}\left(\text{sech}^2(\kappa x) - \epsilon\right) \tag{5.12}$$

where the ξ represents the perpendicular distance of the shape to the slope and ϵ is the parameter that determines the spreading of the sech^2 curve. κ is found from

$$\kappa = \frac{1}{x_{l0}}\text{acosh}\frac{1}{\sqrt{\epsilon}} \tag{5.13}$$

and the x_{l0} is determined by

$$x_{l0} = \frac{b}{2} = \frac{B}{2} \frac{C\sqrt{1-\epsilon}}{\left(3\left(C\sqrt{1-\epsilon} - \ln\frac{1}{\sqrt{\epsilon}} - \frac{\epsilon}{2}C^2\right)\right)^{0.5}} \tag{5.14}$$

where the b is the length of the curve as illustrated in Figure 5.12 and the C is equal to

$$C = \kappa\, x_{l0} = \operatorname{acosh}\frac{1}{\sqrt{\epsilon}} \tag{5.15}$$

The dimensions of the computational domain were given as $h_0 = 1018.3\,m$, $h_1 = 76.37\,m$, $l_1 = 142.51\,m$, $x_g = 1025.8\,m$, $x_0 = 1012.3\,m$ and $x_{end} = 4051\,m$. The parameters for the motion of the sliding mass were stated as $S_0 = 3673\,m$, $u_t = 45.91\,m/s$ and $t_0 = 80\,s$. In addition to the sliding mass kinematics which are described by the Equations 5.8 and 5.11, a ramp-up function was used to initiate the motion of the landslide in the model between the time level $t = 0$ and $t = t_0/20$ [39]. In the FNDBEM model, Equation 5.12 was utilized with the $\epsilon = 0.5$ to describe the geometry of the sliding body which has a thickness of $T = 52\,m$ and a length of $B = 1000\,m$. The resultant curve is illustrated in Figure 5.12 along with the corresponding ellipse. Inserting the $\epsilon = 0.5$ and the $B = 1000\,m$ into Equations 5.15 and 5.14 lead to $b = 1299\,m$ which is the length of the sech^2 curve.

This experiment is also simulated by the FNLFLD model using the computational domain and the sliding mass geometry which were given by Grilli *et al.* [39]. In the FNLFLD model, a fully reflecting wall is located at $x = 20000\,m$ instead of the absorbing piston and the simulations are stopped before any reflection from the wall take place. The vertical nodal spacing on the wall and the horizontal nodal spacing both on the free surface and the bottom are taken as $40\,m$. The source points are placed in the same way as in the previous numerical landslide experiment. The free surface boundary conditions in FLD are integrated with the finite difference formulation of Wu

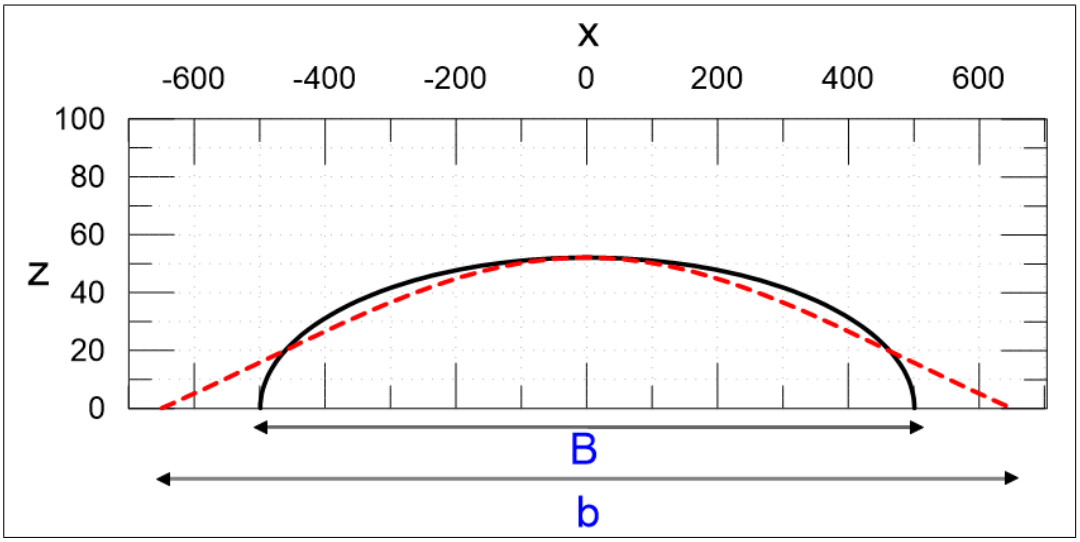

Figure 5.12. The geometry of the ellipse (solid line) and the sech^2 curve (dashed line).

et al.. using a time step $dt = 0.1\,s$. The free surface elevations are given as time series at four different wave gauges in Figure 5.13 along with the time series obtained from the BEM model and the scaled experiment measurements.

The details of the ramp-up function used to initiate the model is not given by Grilli *et al.*, but the non-dimensional kinematics of the landslide is given for the experiment in their fifth Figure [39] (see Figure D.3). In the study of Watts *et al.* [38], it is expressed that the initial acceleration a_0 of the sliding body has a powerful effect on the amplitude of generated waves, therefore the kinematics is digitized from the Figure D.3 that is given by Grilli *et al.*. Gaussian interpolation is utilized to find the information needed regarding the kinematics at specific time levels. The interpolation procedure is the same as was done for the interpolation of the free surface (see Appendix C.1). Grilli *et al.* [39] emphasized that the applied landslide kinematics with Equations 5.8, 5.11 and the ramp-up function is almost identical with the kinematics that is given in Figure D.3 [39]. In addition to the modification of the landslide kinematics, the sech^2 geometry was trimmed by Grilli *et al.* to have a shape that resembles the shape of the semi-ellipse. In the present model, the sech^2 shape is trimmed where the elevation of the sech^2 curve is less than $0.1T$.

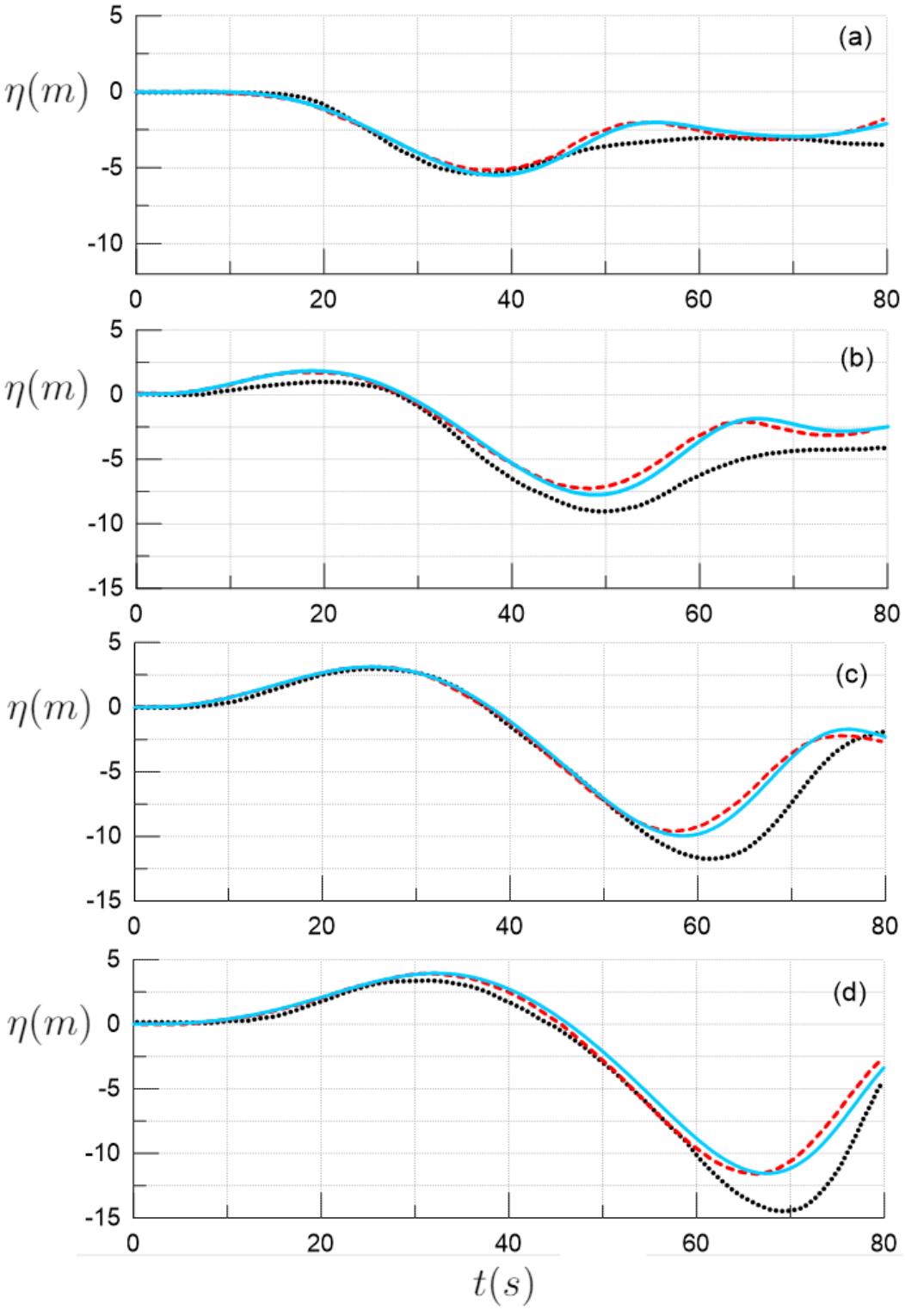

Figure 5.13. The time series of the free surface elevations obtained from the FNLFLD model (solid line), the FNDBEM model (dashed line) and the experimental measurement (dotted line) at (a) x_g, (b) $x_g + 300\,m$,(c) $x_g + 600\,m$ and (d) $x_g + 900\,m$

The results of the FNLFLD model and the FNDBEM model agree well as can be seen in the Figures 5.13 except for a time shift that starts around the 50th second. This may be the results of the small deviations between the landslide kinematics that are applied by the two models. In addition, the generated waves are very sensitive to the details of the bottom geometry so that any difference in the extent of the truncation of the geometry may be another reason for these deviations. The discrepancies between the results of the models and the masurements of the experiment may be associated with the friction created on the laboratory wave tank sidewalls [39] that were used for the Quasi-2D experiment. In general, both models produce consistent results with the measurements despite the fact there are factors that are not taken into account in the both models like surface tension, effects of viscosity, original shape of the sliding body and wave tank. It has to be underlined that the results are very sensitive to the nodal spacing especially to the spacing on the bottom. Thus changing the nodal spacing on the bottom may lead to the variation of the present results.

5.3.2. The Numerical Simulation of Fuhrman and Madsen

In the study of Fuhrman and Madsen, the experiment of Watts *et al.* was simulated by the fully nonlinear, highly dispersive Boussinesq-type (FNHDB) model [43] using the original tank geometry illustrated in Figure 5.10. A $h(x,t)$ function was formulated by Fuhrman and Madsen to model the bottom deformation using the depth intergrated equations. The vertical elevation of the sliding ellipse is given as [67]

$$z_b = \frac{-1}{4(b^2\cos\theta^2 + 4T^2\sin\theta^2)}\Bigg[$$

$$-2\sqrt{2}\sqrt{b^2T^2\big(b^2+4(T^2-2(x-x_c)^2)+(b^2-4T^2)\cos 2\theta\big)}$$

$$+(b^2-4T^2)x\sec\theta\sin 3\theta + b^2x\tan\theta - 4T^2x\tan\theta + 16T^2x_c\tan\theta\Bigg] \qquad (5.16)$$

where the horizontal location of body x_c can be found from Equation 5.7. Equation 5.8 is used for the determination of $S(t)$. The water depth as a function of time and space can be given as [67]

$$h(x,t) = x\tan\theta - \mathcal{H}(\frac{b}{2}\cos\theta - \mid x - x_c \mid)(x\tan\theta + z_b) \tag{5.17}$$

The shape of the sliding body that is obtained from Equation 5.17 matches perfectly with shape of the semi-ellipse. This case with the bottom deformation given in Equation 5.17 is also simulated using the FNLFLD model. The parameters S_0, u_t and t_0 are the same as in the simulation of Grilli *et al.*. The initial submergence d_0 was erroneously given by Fuhrman and Madsen as $161\,m$ [43] which should be $261\,m$. The nodal spacing on the free surface and the bottom is set to $20\,m$ which is the nodal spacing used by Fuhrman and Madsen in their model. A fully reflecting wall located at $x = 20000\,m$ is used again as a no-flux boundary condition. The FSBCs in FLD are integrated with a time step of $dt = 0.2\,s$ using the finite difference formulation of Wu *et al.*.

The time series of the free surface elevations found using the FNLFLD model and the FNHDB model of Fuhrman and Madsen [43] are shown in Figure 5.14 together with the experimental measurements of Watts *et al.*. The agreement between the results of the two models is perfect at first two wave gauges as can be seen in Figures 5.14 a and b. At the third and fourth wave gauges, the FNLFLD model produces closer results to the measurements specifically when the wave trough, which moves above the sliding body as in the previous experiment, passes through these gauges. The discrepancy between two model in the modeling of the wave trough may be related to the findings of Lynett and Liu who stated that they may fail to model the horizontal fluid motion created by SMFs [41]. With increasing depth, the role of the horizontal motion of the landslide in tsunami generation may become more important than its vertical motion.

It should be emphasized that the time series results of the FNHDB model undulates as can be noticed in Figure 5.14 and more clearly in the Figure 9c of the study of Fuhrman and Madsen [43](see Figure D.4). The reason behind these undulations are the fluctuations occurring in the derivative of the water depth given in Equation

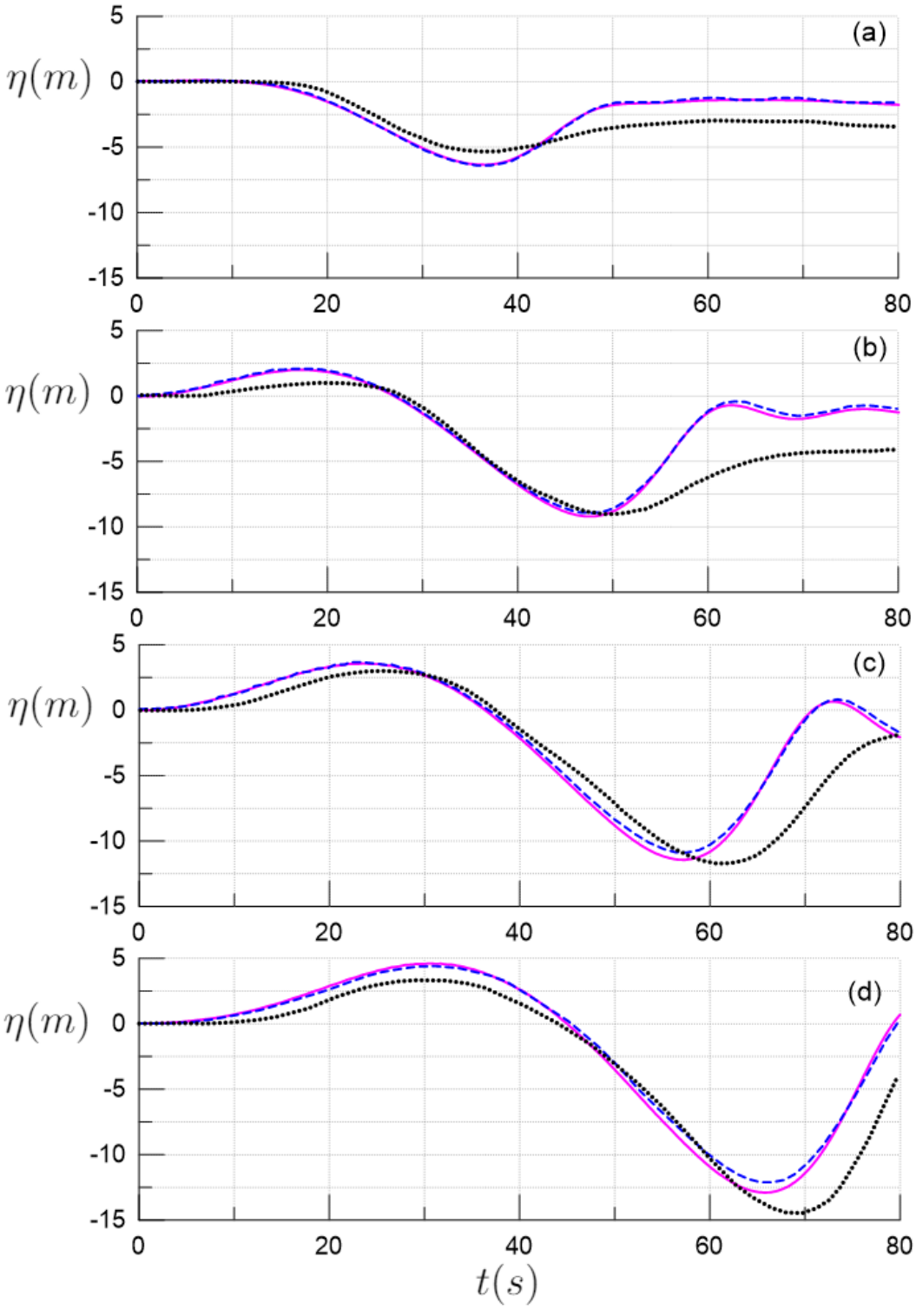

Figure 5.14. The time series of the free surface elevations obtained from the FNLFLD model (solid line), the FNHDB model (dashed line) and the experimental measurement (dotted line) at (a) x_g, (b) $x_g + 300\,m$,(c) $x_g + 600\,m$ and (d) $x_g + 900\,m$

5.17 for the collocation nodes located close to the corner points of the ellipse. These fluctuations are shown for four different instants in Figure 5.15 where the derivatives of water depth with respect to time and space are given for the front face of the sliding ellipse. Since the semi-ellipse has sharp corners as depicted in Figure 5.12, the derivatives at collocation nodes located in the vicinity of these corners deviates at each time level depending on their position. Maximum values of derivatives occur if a collocation node coincides with the corner of the semi-ellipse.

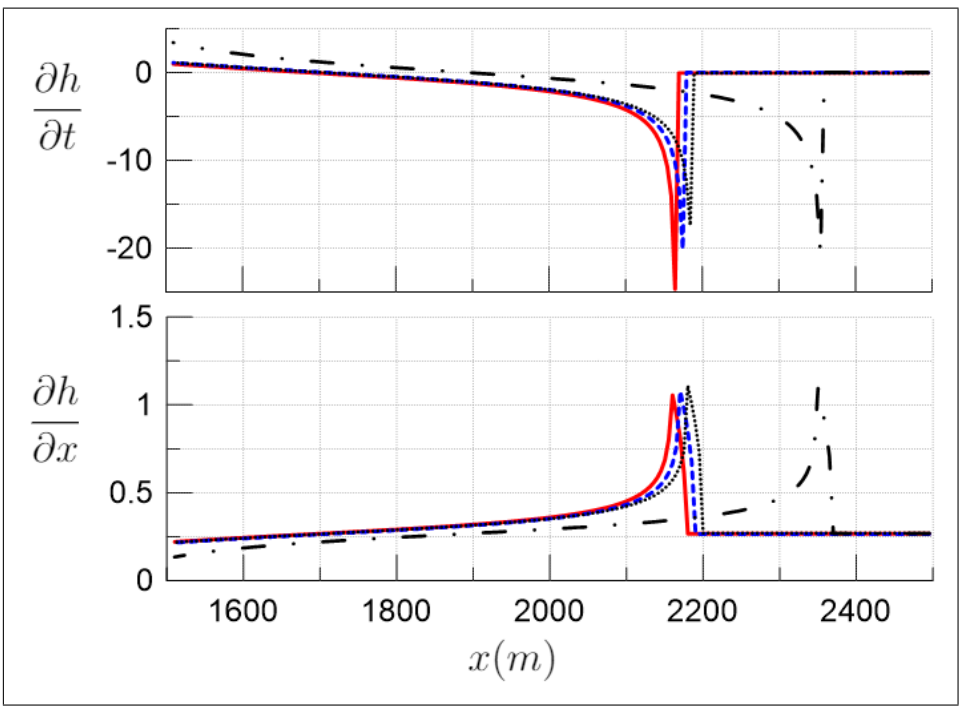

Figure 5.15. The Derivatives of the Water Depth Function given in Equation 5.17 at $t = 44.5\,s$ (solid line), $t = 45\,s$ (dashed line), $t = 45.5\,s$ (dotted line) and $t = 52.5\,s$ (dashed and dotted line)

In order to obtain smoother results, the BBC

$$\vec{\nabla}\phi \cdot \vec{n} = \vec{V}_b \cdot \vec{n} \tag{3.18}$$

is utilized in the model instead of the BBC in terms of the water depth although the information of bottom deformation is obtained from Equation 5.17. The spatial derivative of the bottom geometry is determined using the Gaussian RBF before finding the

unit normal vectors located on the ellipse. The determination of the spatial derivative with the Gaussian RBF is given in the Appendix C.2. The shape parameter selected in the Gaussian RBF is equal to the nodal spacing on the bottom because of the sharp corners where the slope changes dramatically. For the RHS of the BBC, the velocity of the landslide is found using Equation 5.11. The use of the BBC given in Equation 3.18 enables the numerical model to produce smoother time series of free surface elevation. Equivalent results can be obtained using the BBC in terms of water depth but with fluctuations whose frequency can vary depending on the nodal spacing on the bottom.

5.4. The Run-up Experiment of Synolakis

Starting from the nonlinear shallow water equations, Synolakis derived an integral solution for the free surface profile of an arbitrary wave type that runs up a sloping beach [32]. As the initial condition, he used the solitary wave whose profile is given by Equation 5.3 to examine the behaviour of the solitary wave during run-up. The solution domain that Synolakis utilized is given in Figure 5.16. A solitary wave that is located at x_0 starts to propagate from constant depth h_0 towards sloping shore that starts at x_1 with an angle θ. A laboratory experiment was caried out by Synolakis to validate his analytical findings [32]. The detailed descriptions of the tank and the experimental apparatus are given in his PhD Thesis [68].

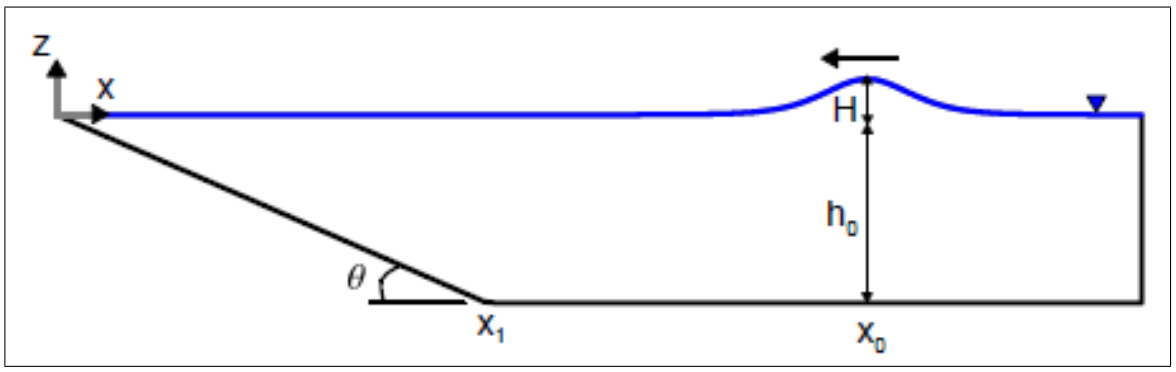

Figure 5.16. The sketch of the solution domain utilized by Synolakis [32, 68]

The experiment is simulated by the FNLFLD model using the computational domain that is illustrated in Figure 5.17 with the collocation nodes and the source

points. The model uses the free surface profile and the horizontal velocity of the solitary wave as input. The solitary wave profile is given as [67]

$$\eta = H\,\mathrm{sech}^2\left(\sqrt{\frac{3H}{4h_0^3}}(x - x_0)\right) \tag{5.3}$$

The horizontal velocities on the free surface for the left going solitary wave are given by

$$u = -\frac{c\,\eta}{h_0 + \eta} \tag{5.18}$$

where the celerity is found by

$$c = \sqrt{g(h_0 + H)} \tag{5.19}$$

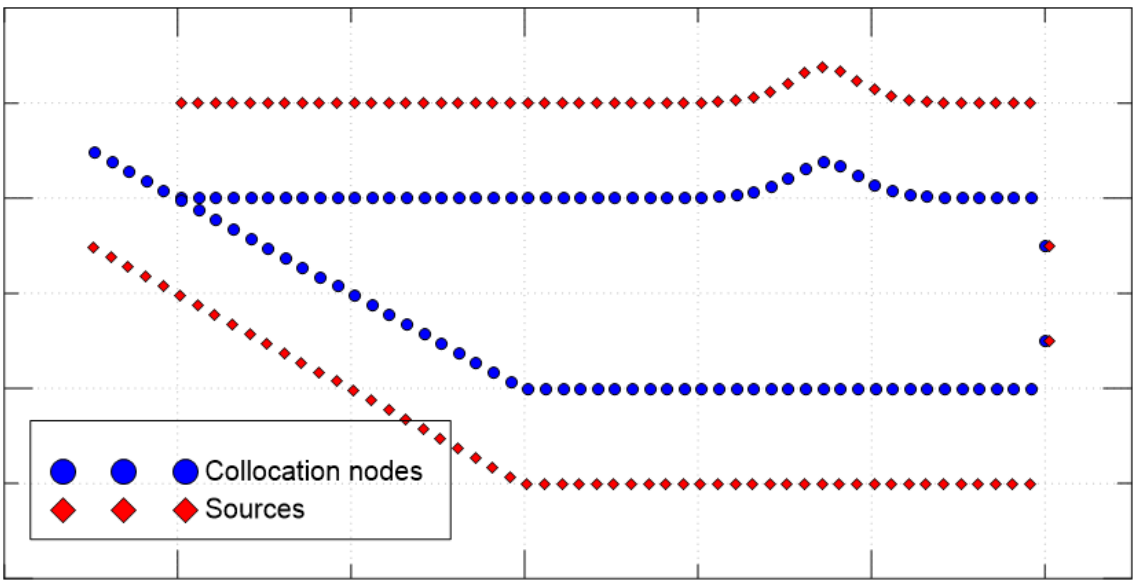

Figure 5.17. Illustration of the initial nodal distribution in the computational domain for the run-up experiment of Synolakis.

Before initiating the model, last step is to set up a BVP to find the vertical velocities as well as the velocity potentials on the free surface. The collocation nodes

on the free surface are located according to Equation 5.3. But this BVP has the flux boundary condition on the free surface, since the horizontal velocities on the free surface are known rather than the velocity potentials. After finding the vertical velocities and the velocity potentials on the free surface collocation nodes, the model can be initiated.

5.4.1. The Free Surface Profile of a Climbing Solitary Wave

The results of the case that has undisturbed water level $h_0 = 1\,m$ and the solitary wave height $H = 0.019\,m$ are reproduced using the present model. The solitary wave is initially located at $x_0 = 37.35\,m$ and the slope starts at $x_1 = 19.85\,m$. A fully reflecting wall at the right end of the domain is located at $x = 75\,m$ and the simulation is stopped before any reflection occurs. The RK O(4)is used for the numerical integration of the surface. The vertical spacing on the wall dz and the horizontal spacing on both the surface and the bottom dx are chosen to be $0.2\,m$. Time step dt is taken as $0.01\,s$. The first collocation node of the free surface is initially located on the sloping bottom on which it slides during simulations.

The free surface profiles obtained from the analytical solution of Synolakis and from the FNLFLD model are given for the 10 different time levels in Figures 5.18, 5.19 and 5.20. The measurements that were taken during different laboratory realizations with the same parameters are also included in the Figures. It is should be emphasized that the solitary waves in laboratory were generated with the motion of a horizontal wave pedal. The location of the pedal corresponds to the right end of the domain which is illustrated in Figure 5.16. Synolakis utilized the algorithm of Goring [23] for the description of the pedal motion which produced solitary waves that nearly match the profile given by Equation 5.3.

The free surface profiles captured by the FNLFLD numerical model are in good agreement with the profiles generated by the solution of Synolakis for the 10 different time levels as shown in Figures 5.18, 5.19 and 5.20. The results of both the FNLFLD model and the analytical solution resemble the profiles obtained in the laboratory with minor time shifts that can arise from the effects of the viscosity. Since the propagation

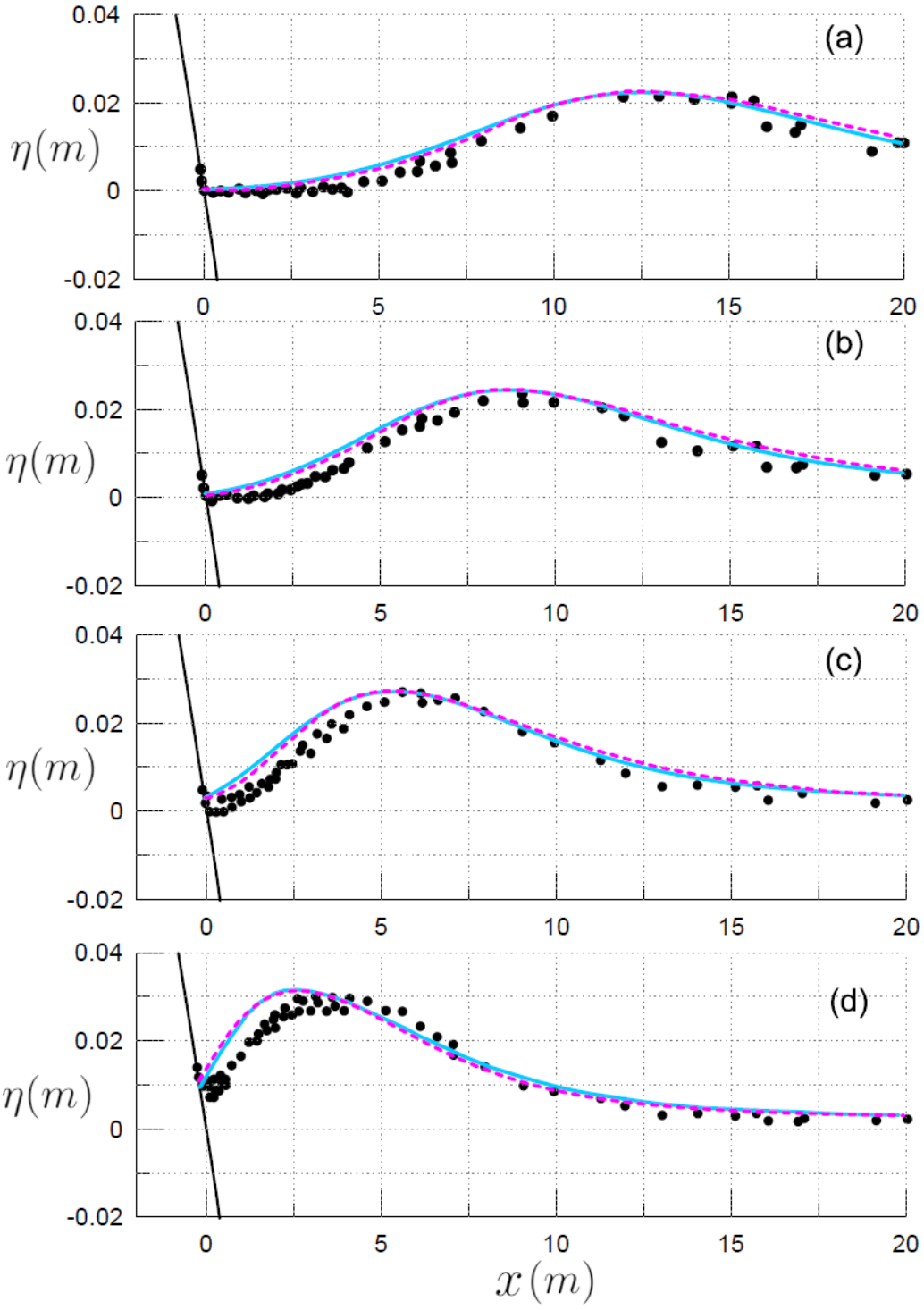

Figure 5.18. The free surface profiles of a climbing solitary wave obtained from the FNLFLD model (solid line), the solution of Synolakis [32] (dashed line) and the experiment (dots): $t\sqrt{g/h_0}$= 25(a), 30(b), 35(c) and 40(d).

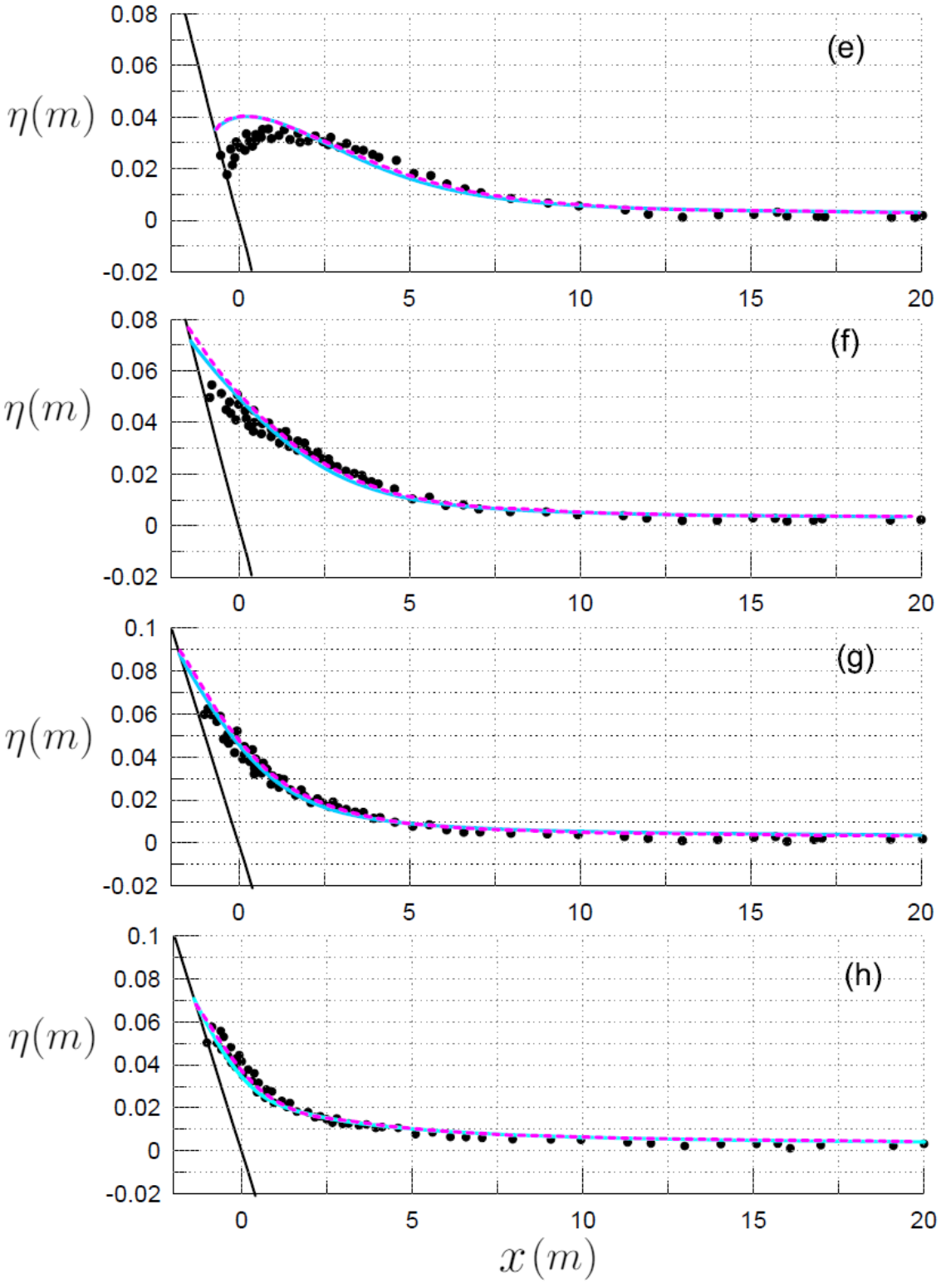

Figure 5.19. The free surface profiles of a climbing solitary wave obtained from the FNLFLD model (solid line), the solution of Synolakis [32] (dashed line) and the experiment (dots): $t\sqrt{g/h_0}$= 45(e), 50(f), 55(g) and 60(h).

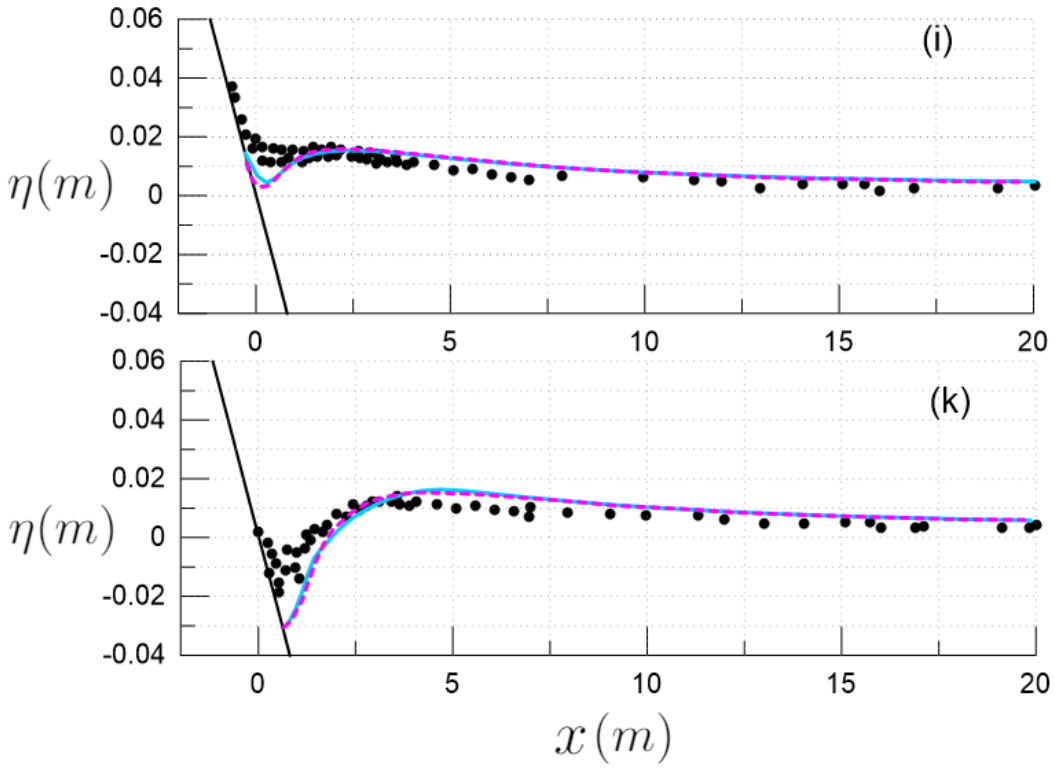

Figure 5.20. The free surface profiles of a climbing solitary wave obtained from the FNLFLD model (solid line), the solution of Synolakis [32] (dashed line) and the experiment (dots): $t\sqrt{g/h_0}$= 65(i) and 70(k).

distance is small, energy dissipation does not shorten the wave height towards the shore as can be seen in the Figures 5.18 a, 5.18 b, 5.18 c and 5.18 d. However, because of the boundary layer that is created on the slope, the maximum run-up is less than than predicted by the model and the analytical solution.

It has to be underlined that the solitary wave ($H/h_0 = 0.019$) whose free surface profiles are given in the Figures 5.18, 5.19 and 5.20 breaks between the time level $t\sqrt{g/h_0}$=65 and $t\sqrt{g/h_0}$=70 during backwash in the numerical model. The limit for the solitary wave breaking during run-down can be given as [69],

$$\frac{H}{h_0} > 0.479\,(\cot\theta)^{-\frac{10}{9}} \tag{5.20}$$

For the slope of the simulated case ($\cot\theta = 19.85$), the limiting wave height to water depth ratio (H/h_0) is found as 0.0173 which is smaller than 0.019. The findings of the numerical model are in agreement with the limit given in Equation 5.20. Before reaching the instance $t\sqrt{g/h_0}$=70, the part of the wave in which the first collocation node is located breaks in the numerical model. But breaking does not reach the second collocation node, thus the exclusion of the first collocation node that is located on the slope enables the model to produce the free surface profile given in Figure 5.20 k.

5.4.2. The Maximum Run-up

In addition to his integral solution, Synolakis derived a run-up law [32] that relates the maximum run-up of a solitary wave to its wave height and the angle of the slope on which it climbs. The run-up law is given by Synolakis as follows

$$\frac{R}{h_0} = 2.831\sqrt{\cot\theta}\left(\frac{H}{h_0}\right)^{1.25} \tag{5.21}$$

where R is the maximum run-up that is calculated as the maximum elevation of the intersection point of the free surface and the slope with respect to still water level. Note that the first collocation node of the free surface that is located on the slope stands for this intersection point. The maximum run-up values found by the numerical model are given in Table 5.1 with the maximum run-up values that were obtained in the experiments and from the run-up law [32].

For small amplitude solitary waves, the present model produced very accurate results, whereas the difference between the values obtained in the experiment and computed by the FNLFLD model increases as the wave height increases. This increase can be associated with viscosity whose effects grows as the wave propagates further on the slope as in Figure 5.19 g. The boundary layer created on the sloping bottom is greater for the larger waves. The run-ups obtained by the run-up law agree well with the numerical model especially for small amplitude waves. However as the wave height increases the model produce more accurate results compared to the run-up law.

Table 5.1. The maximum run-ups of solitary waves on a 1:19.85 slope

H/h0	**Experiment R/h0**	**Run-up Law R/h0**	**Model R/h0**
0.005	0.019	0.0168	0.0176
0.006	0.022	0.0211	0.0220
0.007	0.026	0.0255	0.0265
0.009	0.036	0.0349	0.0359
0.014	0.052	0.0607	0.0612
0.019	0.077	0.0889	0.0882
0.022	0.098	0.1068	0.1049
0.028	0.123	0.1444	0.1393
0.034	0.144	0.1841	0.1747

5.5. Summary of the Results

The results presented in this study are summarized in Table 5.2

Table 5.2. Summary of the Results. PA, GA and MA stand for perfect, good and moderate agreement, respectively.

Experiments	\Model Simulation \	**(A)** FNLFLD RK O(4)	**(B)** FNLFLD FD (2) & CN	**(C)** FNLSLD AB O(4)
Experiments of Hammack	Impulsive Up-thrust	-in PA w/ B & C -in GA w/ the measurements	-in PA w/ A & C -in GA w/ the measurements	-in PA w/ A & B -in GA w/ the measurements
	Impulsive Down-thrust	-in PA w/ B & C -in GA w/ the measurements	-in PA w/ A & C -in GA w/ the measurements	-in PA w/ A & B -in GA w/ the measurements
	Long Distance Propagation	-in PA w/ C -in PA w/ a published result	-failed to model	-in PA w/ A -in PA w/ a published result
Experiment of Lynett & Liu	Experiment of Lynett & Liu	-not tested	-in PA w/ a published result	-not applicable
Experiment of Watts et al.	Simulation of Grilli et al.	-not tested	-in GA w/ a published result -in MA w/ the measurements	-not tested
	Simulation of Fuhrman & Madsen	-not tested	-in PA w/ a published result -in MA w/ the measurements	-not applicable
Experiments of Synolakis	Free Surface Profiles	-in PA w/ the solution -in GA w/ the measurements	-not tested	-not applicable
	Maximum Run-up	-in PA w/ the run-up law -in GA w/ the measurements	-not tested	-not applicable

6. CONCLUSION AND RECOMMENDATIONS

The numerical model is based on potential flow theory in which the fluid is assumed to be ideal. Thus water is considered to be an inviscid, irrotational and incompressible fluid in the numerical model as in the other numerical models that are used for comparison in the present study. Most of the developers of these models attributed the deviations of the model results from the experimental measurements to the effects of the viscosity. This is a reasonable argument considering that the experiments are conducted in wave tanks in which the water interacts with side walls and the bottom over which viscous boundary layers form and retard the flow. When modeling real tsunami events, the effects of viscosity may be not as significant as in the experiments conducted in laboratory wave flumes. If viscous effects are to be included, the Navier-Stokes equations would have to be solved. As the fundamental solution of these equations is not known, the MFS cannot be used. Instead, as a meshless modelling method one could consider the RBFCM. However, this method requires that nodes be placed in the solution domain. Considering the expanse of oceans and the depths over which tsunamis propagate the size of the resulting system matrix would so large as to inhibit efficient solutions.

In the experiment of Hammack, where the wave generation mechanism is analogous to the tsunami generation mechanism of the motion of the tectonic plates in normal and thrust faults, the generated waves consist of dispersive and non-dispersive water waves. The non-dispersive waves are the leading waves whose non-linearity increases even during constant depth propagation. The trailing non-dispersive waves are relatively smaller in height. Thus, nonlinear, weakly dispersive or non-dispersive depth-integrated and depth-averaged models can be utilized for the modeling of tsunamis that are generated by the vertical motion of the bottom, since the leading non-disperive waves appear to be of major importance for possible coastal hazards. On the other hand, submarine landslide generated water waves are expected to be dispersive. In the results of the submarine landslide experiment simulations, it is observed that the weakly dispersive model deviates from the dispersive model as the submergence of the

landslide increases. Moreover, nonlinearties may become important depending on the geometry of the landslide. Consequently, the numerical models that are fully nonlinear and dispersive are more favoured in the modeling of the tsunami generation and propagation that occur due to any type of seabed deformation.

The numerical model presented in this study solves the classical wave boundary value problem with the fully nonlinear FSBCs which are applied on the time dependent deforming free surface. Therefore, it is a fully nonlinear, dispersive model which is valid at all depths without any constraint on the wave height and wave length for nonbreaking waves. In addition to the ease of modeling the deforming free surface, given bottom deformations are also easily implemented in the numerical model in which two different forms of the no-flux BBC can be used. The implementation of such deforming boundaries would be highly complex while using numerical models which necessitate a prescribed mesh arrangement. Overall the utilization of a meshless numerical model facilitates the implementation of deforming boundaries and their boundary conditions.

Bottom deformations which may occur at large depths of oceans generate water waves that propagate over large distances. As a results, the solution domain of the classical wave boundary value problem can be quite large. The resultant system matrices, which have to be updated and solved at each time step, may be quite large when a domain type numerical method is used for the solution of the problem. For the present numerical model, a boundary-only numerical method, namely the MFS, is utilized. The fundamental solution of the 2D Laplace equation is used as approximating function, thus, the classical wave BVP could be solved only with collocation nodes that are located on the boundaries. Consequently, the use of the MFS enabled the present numerical model to solve the classical wave BVP on larger domains with the existing computational facilities.

The MFS is a collocation method, in which the approximating function is singular when the sources (RBF centers) and the collocation nodes are at same geometrical positions. Therefore, the method requires fictitious boundaries on which the sources are located. Theoretically, the accuracy of the method increases with the increasing

distance between the sources and the collocation nodes. But the increase of the distance leads to a higher condition number which decreases the solvability of the matrix. On the other hand, when the sources are located too close to the collocation nodes, then the fundamental solution is close to being singular, thus numerical instability occurs. The positions of the sources which affect the accuracy of the method are an active research area. In the present numerical model, the sources are located parallel to the collocation nodes and their positions are updated at each time level according to the positions of the collocation nodes that move with the physical boundaries to prevent the sources from being close to the collocation nodes. Before the simulation is started in the numerical model, it is a good idea to check the initial condition number of the resultant system matrix and to see whether the linear system of the equations can be solved within the acceptable precision with the existing solvers. Since the source to collocation point distances are preserved as the surface boundary deforms, it is expected that condition numbers similar to the initial condition number will result at each time step.

The original form of the FSBCs includes local derivatives that give the change of the velocity potential and the free surface elevation with respect to time at a point where the free surface instanly located. This form is not useful for the time integration considering that the integration of the DFSBC in this form would give the velocity potential at next time level at the point where the free surface occupied at previous time level. Therefore, two different descriptions, which are more proper in the context of the time integration than the original form of the FSBC, are utilized in the numerical model. For both descriptions, the FSBCs are modified to keep track of water particles (collocation nodes in the model) on the surface and their corresponding velocity potentials. The main difference between two descriptions is that the motion of the water particles is limited to the vertical direction in the SLD, whereas the water particles are free to move in all directions in the FLD.

The use of the FLD of the free surface enables the model to simulate the wave run-up and run-down in addition to wave overturning until breaking, thus all the experiments presented in this study could be simulated using the FLD. The run-up

experiment of Synolakis in which the run-ups of the solitary waves were investigated can be reproduced by the numerical model using the FLD of the free surface with a high degree of precision. Although the applicability of the analytical and experimental findings of Synolakis to the run-ups of tsunamis is questioned in literature [26], his integral solution and run-up law are commonly used along with his experimental measurements to validate models.

In addition to the FLD, the SLD is also used for the integration of the FSBCs, however its application is limited due to the fact that the horizontal motion of the water particles is neglected. The accuracy of the SLD of the free surface is tested by simulations of the Hammack experiments. The results obtained from the two descriptions of the free surface at the wave gauges are in perfect agreement. The only discrepancy between the results of the two descriptions is observed at the leading waves with an amplitude difference of 2 percent of the wave height after the 2500 water depths of propagation of the wave system that is created by the impulsive bed up-thrust (see Figure B.3). Therefore, the use of the SLD is recommended for the numerical models which require uniform spacing on its boundaries considering that the horizontal positions of the free surface collocation nodes are fixed while using the SLD of the free surface. Additional techniques have to be developed for the calculation of the wave run-up and run-down if the SLD of the free surface is to be employed. In general, utilizing the FLD is strongly recommended for the models, which do not necessitate the horizontal positions of the free surface collocation nodes to be fixed as the present model thanks to the meshless nature of the MFS.

In the simulation of the Hammack's experiments, the FSBCs in FLD are integrated using two different time integration techniques which are the finite difference formulation of Wu *et al.* and the RK O(4). The finite difference formulation of Wu *et al.* by which the BVP has to be solved once for each time step requires a smaller step size than the RK O(4) which necessitates that the BVP has to be solved four times at each time step. Using identical nodal configurations and Wu's integrator with a time step that is one tenth of the time step used for the RK O(4), the results obtained from the two techniques were found to be in perfect agreement at all stations of the

experiment. After 2500 water depths of propagation in the case of the positive bottom deformation, the free surface profile obtained using the Wu's integrator does not resemble the free surface profile obtained using the RK (4) and captured by the other numerical model used for comparison. Thus, the use of this finite difference formulation is not recommended for the modeling of the waves that propagate over long distances. The accumulation of the numerical error may cause deviations in the obtained results. To decrease the numerical error produced at each time level, an additional BVP can be solved to find the new velocities at the positions modified using the Crank-Nicolson formula. Another remedy can be decreasing the timestep further which may lead to more accurate results but the procedure won't be as computationally efficient as the RK O(4).

The nature of the SLD necessitates the timestep to be small due to the fact that the horizontal motions of the water particles on the free surface are neglected whereas their horizontal velocities are not. Keeping the timestep small by the implementation of the RK O(4) would not be computatinally efficient due to the fact that RK O(4) requires the BVP to be solved four times at each time level. Thus the AB O(4) with a smaller time step is prefered for the integration of the free surface in SLD rather than RK O(4).

In the present study, a 2D numerical modal was developed for the modeling of the three phases of the tsunami life cycle, namely the generation, propagation and run-up. Its performance is tested through the simulations of the four benchmark problems which are commonly used in the literature for the validations of numerical models. Three benchmark problems for tsunami generation are simulated using the present numerical model which produces comparable results with other well-known numerical models. In addition, the wave run-up and run-down can be modeled by the model with a high degree of precision. Both BBCs utilized in the model are no-flux boundary conditions and can be applied depending on the given information of bottom deformation.

Due to the meshless nature of the MFS, other benchmark problems that have complex geometries and deformations can be easily modeled using the presented model.

Moreover, the MFS is a boundary-only method, thus, 3D version of the model can be developed to simulate 3D problems with large domains using the computational facilities available at the time of this study.

REFERENCES

1. Segur, H., "Waves in shallow water, with emphasis on the tsunami of 2004", A. Kundu (Editor), *Tsunami and Nonlinear Waves*, pp. 3–29, Springer, Springer Verlag, Berlin, 2007.

2. Lay, T., C. J. Ammon, H. Kanamor, L. Xue and M. J. Kim, "Possible large near-trench slip during the 2011 Mw 9.0 off the Pacific coast of Tohoku Earthquake", *Earth Planets Space*, Vol. 63, p. 687–692, 2011.

3. *U. S. Geological Survey*, `https://www.usgs.gov`, accessed in May 2019.

4. Rabinovich, A., E. A. Kulikov and I. V. Fine, "The Kuril Earthquakes and tsunamis of November 15, 2006, and January 13, 2007: Observations, analysis, and numerical modeling", *Oceanology*, Vol. 49(2), pp. 166–181, 2009.

5. Lay, T., H. Kanamori, C. J. Ammon, A. R. Hutko, K. Furlong and L. Rivera, "The 2006–2007 Kuril Islands great earthquake sequence", *Journal of Geophysical Research*, Vol. 114, 2009.

6. Synolakis, C. E., J.-P. Bardet, J. C. Borrero, H. L. Davies, E. A. Okal, E. A. Silver, S. Sweet and D. R. Tappin, "The slump origin of the 1998 Papua New Guinea Tsunami", *Proceedings of The Royal Society A Mathematical Physical and Engineering*, Vol. 458, pp. 763–789, 2002.

7. Lynett, P. J., J. C. Borrero, P. L. Liu and C. E. Synolakis, "Field Survey and Numerical Simulations: A Review of the 1998 Papua New Guinea Tsunami", *Pure and Applied Geophysics*, Vol. 160, p. 2119–2146, 2003.

8. Tappin, D. R., S. T. Grilli, J. C. Harris, R. J. Geller, T. Masterlark, J. T. Kirby, F. Shi, G. Ma, K. Thingbaijam and P. M. Mai, "Did a submarine landslide contribute to the 2011 Tohoku tsunami?", *Marine Geology*, Vol. 357, pp. 344–361,

2014.

9. Synolakis, C. E. and E. Okal, "A Theoretical Comparison of Tsunamis from Dislocations and Landslides", *Pure and Applied Geophysics*, Vol. 160(10), pp. 2177–2188, 2003.

10. Dias, F., D. Dutykh, L. O'Brien, E. Renzi and T. Stefanakis, "On the Modelling of Tsunami Generation and Tsunami Inundation", *Mechanics for the World: Proceedings of the 23rd International Congress of Theoretical and Applied Mechanics*, Vol. 10, pp. 338–355, 2014.

11. Enet, F., S. T. Grilli and P. Watts, "Laboratory Experiments for Tsunamis Generated by Underwater Landslides: Comparison with Numerical Modeling", *Proceedings of The Thirteenth (2003) International Offshore and Polar Engineering Conference*, 2003.

12. Talling, P., M. Clare, M. Urlaub, E. Pope, J. Hunt and S. Watt, "Large Submarine Landslides on Continental Slopes: Geohazards, Methane Release, and Climate Change", *Oceanography*, Vol. 27 (2), pp. 32–45, 2014.

13. Harbitz, C. B., F. Løvholt, G. Pedersen and D. G. Masson, "Mechanisms of tsunami generation by submarine landslides: a short review", *Norsk Geologisk Tidsskrift*, Vol. 86(3), pp. 255–264, 2006.

14. Grilli, S. T. and P. Watts, "Tsunami Generation by Submarine Mass Failure. I: Modeling, Experimental Validation, and Sensitivity Analyses", *Journal of Waterway, Port, Coastal, and Ocean Engineering*, Vol. 131, p. 283–297, 2005.

15. Bryant, E., *Tsunami: The Underrated Hazard*, Springer, 2 edn., 2008.

16. Dean, R. G. and R. A. Dalrymple, *Water Wave Mechanics for Engineers and Scientists*, World Scientific, Singapore, 1991.

17. Synolakis, C., "Tsunami and Seiche", W.-F. Chen and C. Scawthorn (Editors), *Earthquake Engineering Handbook*, chap. 9, pp. 9.91–9.90, CRC Press LLC, 2003.

18. Tappin, D. R., "Tsunamis from submarine landslides", *Geology Today*, Vol. 33, pp. 190–200, 2017.

19. Okal, E. A., "Normal Mode Energetics for Far-field Tsunamis Generated by Dislocations and Landslides", *Pure and Applied Geophysics*, Vol. 160, p. 2189–2221, 2003.

20. Geist, E. L., "Local Tsunamis and Earthqauke Source Parameters", *Advances In Geophysics*, Vol. 39, 1997.

21. Okal, E. and C. E. Synolakis, "Source discriminants for near-field tsunamis", *Geophysical Journal International*, Vol. 158(3), p. 899–912, 2004.

22. Yeh, H., P. Liu, M. Briggs and C. Synolakis, "Propagation and amplification of tsunamis at coastal boundaries", *Nature*, Vol. 372, pp. 353–355, 1994.

23. Goring, D. G., *Tsunamis:The Propagation of Long Waves onto a Shelf*, Ph.D. Thesis, California Institute of Technology, 1979.

24. Lamb, K. G. and V. T. Nguyen, "Calculating Energy Flux in Internal Solitary Waves with an Application to Reflectance", *Journal of Physical Oceanography*, Vol. 39(3), 2009.

25. Hammack, J. L. and H. Segur, "The Korteweg-de Vries equation and water waves. Part 2. Comparison with experiments", *Journal of Fluid Mechanics*, Vol. 65 (2), pp. 289–314, 1974.

26. Fuhrman, D. R., P. A. Madsen and H. A. Schäffer, "On the solitary wave paradigm for tsunamis", *Journal of Geophysical Research Atmospheres*, Vol. 113(C12), 2008.

27. Tadepalli, S. and C. E. Synolakis, "The run-up of N-waves on sloping beaches",

Proceedings: Mathematical and Physical Sciences, Vol. 445, 1994.

28. Tadepalli, S. and C. E. Synolakis, "Model for the Leading Waves of Tsunamis", *Physical review letters*, Vol. 77(10), 1996.

29. Pelinovsky, E. N. and R. K. Mazova, "Exact Analytical Solutions of Nonlinear Problems of Tsunami Wave Run-up on Slopes with Different Profiles", *Natural Hazards*, Vol. 6, pp. 227–249, 1992.

30. Hammack, J., "A note on tsunamis: their generation and propagation in an ocean of uniform depth", *Journal of Fluid Mechanics*, Vol. 60(4), 1973.

31. Hammack, J. L. and H. Segur, "The Korteweg-de Vries equation and water waves. Part 3. Oscillatory waves", *Journal of Fluid Mechanics*, Vol. 84 (2), pp. 337–358, 1978.

32. Synolakis, C. E., "The Runup of Solitary Waves", *Journal of Fluid Mechanics*, Vol. 185, 1987.

33. Synolakis, C. E., M. K. Deb and J. E. Skjelbreia, "The anomalous behavior of the runup of cnoidal waves", *Physics of Fluids*, Vol. 31(3), 1988.

34. Titov, V. V. and C. E. Synolakis, "Modeling of Breaking and Nonbreaking Long-Wave Evolution and Runup Using VTCS-2", *Journal of Waterway, Port, Coastal, and Ocean Engineering*, Vol. 121(6), 1995.

35. Carrier, G. F., T. T. Wu and H. Yeh, "Tsunami run-up and draw-down on a plane beach", *Journal of Fluid Mechanics*, Vol. 475, pp. 79–99, 2003.

36. Klettner, C., S. Balasubramanian, J. Hunt, H. J. S. Fernando, S. Voropayev and I. Eames, "Draw-down and run-up of tsunami waves on sloping beaches", *Engineering and Computational Mechanics*, Vol. 165(2), pp. 119–129, 2012.

37. Grilli, S. T. and P. Watts, "Modeling of waves generated by a moving submerged

body. Applications to underwater landslides", *Engineering Analysis with Boundary Elements*, Vol. 23(8), pp. 645–656, 1999.

38. Watts, P., F. Imamura and S. T. Grilli, "Comparing model simulations of three benchmark tsunami generation cases", *Science of Tsunami Hazards*, Vol. 18(2), pp. 107–124, 2000.

39. Grilli, S. T., S. Vogelmann and P. Watts, "Development of a 3D Numerical Wave Tank for modeling tsunami generation by underwater landslides", *Engineering Analysis with Boundary Elements*, Vol. 26, pp. 301–313, 2002.

40. Enet, F. and S. T. Grilli, "Experimental Study of Tsunami Generation by Three-Dimensional Rigid Underwater Landslides", *Journal of Waterway, Port, Coastal, and Ocean Engineering*, Vol. 133, p. 442–454, 2007.

41. Lynett, P. J. and P. L. Liu, "A numerical study of submarine-landslide-generated waves and run-up", *Proceedings of The Royal Society A Mathematical Physical and Engineering Sciences*, Vol. 458(2028), pp. 2885–2910, 2002.

42. Lynett, P. J. and P. L. Liu, "A numerical study of the run-up generated by three-dimensional landslides", *Journal of Geophysical Research*, Vol. 110, 2005.

43. Fuhrman, D. R. and P. A. Madsen, "Tsunami generation, propagation, and run-up with a high-order Boussinesq model", *Coastal Engineering*, Vol. 56(7), pp. 747–758, 2009.

44. Pudjaprasetya, S. R. and S. S. Tjandra, "A Hydrodynamic Model for Dispersive Waves Generated by Bottom Motion", J. Fuhrmann, M. Ohlberger and C. Rohde (Editors), *Finite Volumes for Complex Applications VII-Methods and Theoretical Aspects*, pp. 449–456, Springer, Springer Verlag, Berlin, 2014.

45. Tjandra, S. S. and S. R. Pudjaprasetya, "A non-hydrostatic numerical scheme for dispersive waves generated by bottom motion", *Wave Motion*, Vol. 57, pp. 245–

256, 2015.

46. Imamura, F., A. C. Yalciner and G. Ozyurt, "Tsunami Modelling Manual", *UNESCO IOC international training course on Tsunami Numerical Modelling*, 2006.

47. Liu, P. L.-F., C. Synolakis, T.-R. Wu, F. Raichlen and J. C. Borrero, "Runup and rundown generated by three-dimensional sliding masses", *Journal of Fluid Mechanics*, Vol. 536(1), pp. 107–144, 2005.

48. Maa, G., J. T. Kirby and F. Shi, "Numerical simulation of tsunami waves generated by deformable submarine landslides", *Ocean Modelling*, Vol. 69(13), pp. 146–165, 2013.

49. Rzadkiewicz, S. A., C. Mariotti and P. Heinrich, "Numerical simulation of submarine landslides and their hydraulic effects", *Journal of Waterway, Port, Coastal and Ocean Engineering*, Vol. 123(4), pp. 149–157, 1997.

50. Smith, R. C., J. Hill, G. S. Collins, M. D. Piggott, S. C. Kramer, S. D. Parkinson and C. Wilson, "Comparing approaches for numerical modelling of tsunami generation by deformable submarine slides", *Ocean Modelling*, Vol. 100, pp. 125–140, 2016.

51. Løvholt, F., G. Pedersen, C. B. Harbitz, S. Glimsdal and J. Kim, "On the characteristics of landslide tsunamis", *Philos Trans A Math Phys Eng Sci.*, Vol. 373(2053), 2015.

52. Qiu, L.-C., F. Jin, P.-Z. Lin, Y. Liu and Y. Han, "Numerical simulation of submarine landslide tsunamis using particle based methods", *Journal of Hydrodynamics, Ser. B*, Vol. 29(4), pp. 542–551, 2017.

53. Tsung, W.-S., S.-C. Hsiao, T.-Y. Huang and N.-J. Wu, "Simulation of propagation and run-up of landslide-induced waves using meshless method", *Journal of Coastal Research*, Vol. 65, pp. 404–409, 2013.

54. Hsiao, S.-C., T.-Y. Huang and N.-J. Wu, "Nonlinear wave propagation and run-up generated by subaerial landslides modeled using meshless method", *Comput Mech*, Vol. 53, pp. 203–214, 2014.

55. Longuet-Higgins, M. S., F.R.S. and E. D. Cokelet, "The deformation of steep surface waves on water I. A numerical method of computation", *Proceedings of the Royal Society of London*, Vol. 250, 1976.

56. Kennedy, A. B. and J. D. Fenton, "A fully-nonlinear computational method for wave propagation over topography", *Coastal Engineering*, Vol. 32, 1997.

57. Kupradze, V. and M. Aleksidze, "A method for the approximate solution of limiting problems in mathematical physics", *U.S.S.R. Computational Mathematics and Mathematical Physics*, Vol. 4, 1964.

58. Kupradze, V. and M. Aleksidze, "The method of functional equations for the approximate solution of certain boundary value problems", *U.S.S.R. Computational Mathematics and Mathematical Physics*, Vol. 4, 1964.

59. Bôcher, M., "Singular points of functions which satisfy partial differential equations of the elliptic type", *Bull. Amer. Math. Soc*, Vol. 9, 1903.

60. Kythe, P. K., *Fundamental Solutions for Differential Operators and Applications*, Birkhäuser, Boston, USA, 1996.

61. Bogomolny, A., "Fundamental Solutions Method for Elliptic Boundary Value Problems", *SIAM Journal on Numerical Analysis*, Vol. 22(4), 1985.

62. Chen, C., Y. Hon and R. Schaback, *Scientific Computing with Radial Basis Functions*, University of Southern Mississippi, Mississippi, USA.

63. Wu, N.-J., T.-K. Tsay and D. L. Young, "Meshless numerical simulation for fully nonlinear water waves", *International Journal for Numerical Methods in Fluids*,

Vol. 50, 2006.

64. Wu, N.-J., T.-K. Tsay and D. L. Young, "Computation of Nonlinear Free-Surface Flows by a Meshless Numerical Method", *Journal of Waterway, Port, Coastal, and Ocean Engineering*, Vol. 134(2), 2008.

65. Wu, N.-J., and K.-A. Chang, "Simulation of free-surface waves in liquid sloshing using a domain-type meshless method", *International Journal for Numerical Methods in Fluids*, Vol. 67, 2011.

66. Dingemans, M. W., *Water Wave Propagation Over Uneven Bottoms : Part 2*, World Scientific, 596224 Singapore, 1997.

67. Boussinesq, J. V., "Théorie des ondes et des remous qui se propagent le long d'un canal rectangulaire horizontal, en communiquant au liquide contenu dans ce canal des vitesses sensiblement pareilles de la surface au fond", *Journal de Mathématiques Pures et Appliquées*, Vol. 17, p. 55–108, 1872.

68. Synolakis, C. E., *The Runup of Long Waves*, Ph.D. Thesis, California Institute of Technology, 1986.

69. Gjevik, B. and G. P. q, "Run-up of long waves on an inclined plane", *Preprint Series Inst. of Math*, 1981.

APPENDIX A: THE RESULTS OBTAINED IN THE SIMULATIONS OF HAMMACK'S EXPERIMENTS USING THE FORMULATION OF WU *et al.*

The case that has a still water level $h_0 = 0.5\,m$ is simulated using the finite difference formulation of Wu *et al.* for the integration of the FSBCs. The horizontal spacing on the free surface and the bottom is set to $dx = 0.5m$. The vertical spacing on the vertical walls is $dz = 0.05\,m$. The time step is chosen to be $dt = 0.001\,s$. The results obtained using the formulation are given in Figures A.1 and A.2 for the impulsive bed down-thrust and the impulsive bed upthrust, respectively.

The time series obtained using the RK O(4) are also included in Figures. The nodal spacings utilized in RK O(4) are same as utilized in the formulation of Wu *et al.* But the time step is chosen to be $dt = 0.01\,s$. The agreement between the results obtained by both time integration techniques is perfect.

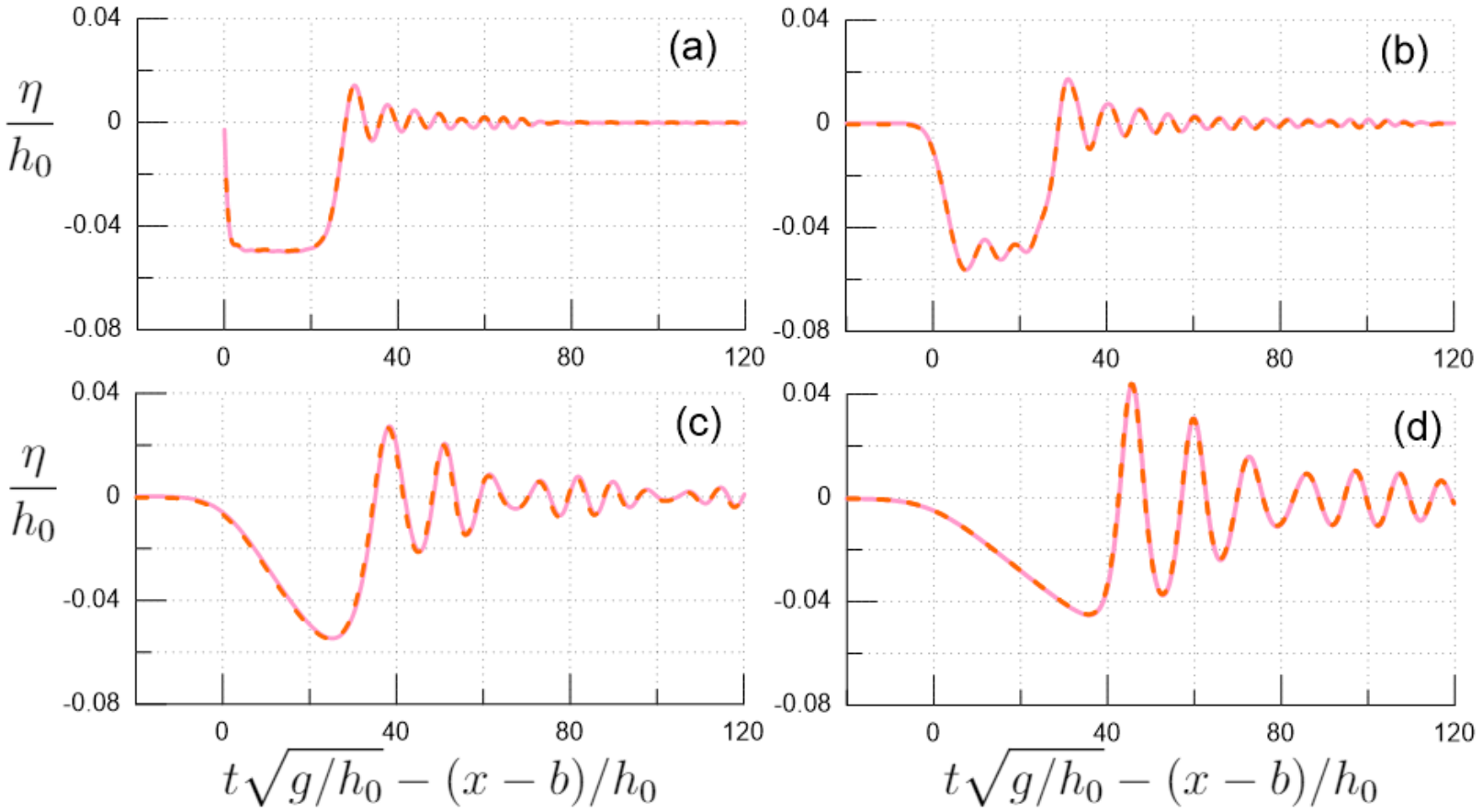

Figure A.1. Time series of the free surface elevations obtained in the simulation of the bed down-thrust using the formulation of Wu *et al.* (solid line) and using the RK O(4) (dashed line) at gauges (a)$(x-b)/h_0 = 0$, (b)$(x-b)/h_0 = 20$, (c)$(x-b)/h_0 = 180$ and (d)$(x-b)/h_0 = 400$.

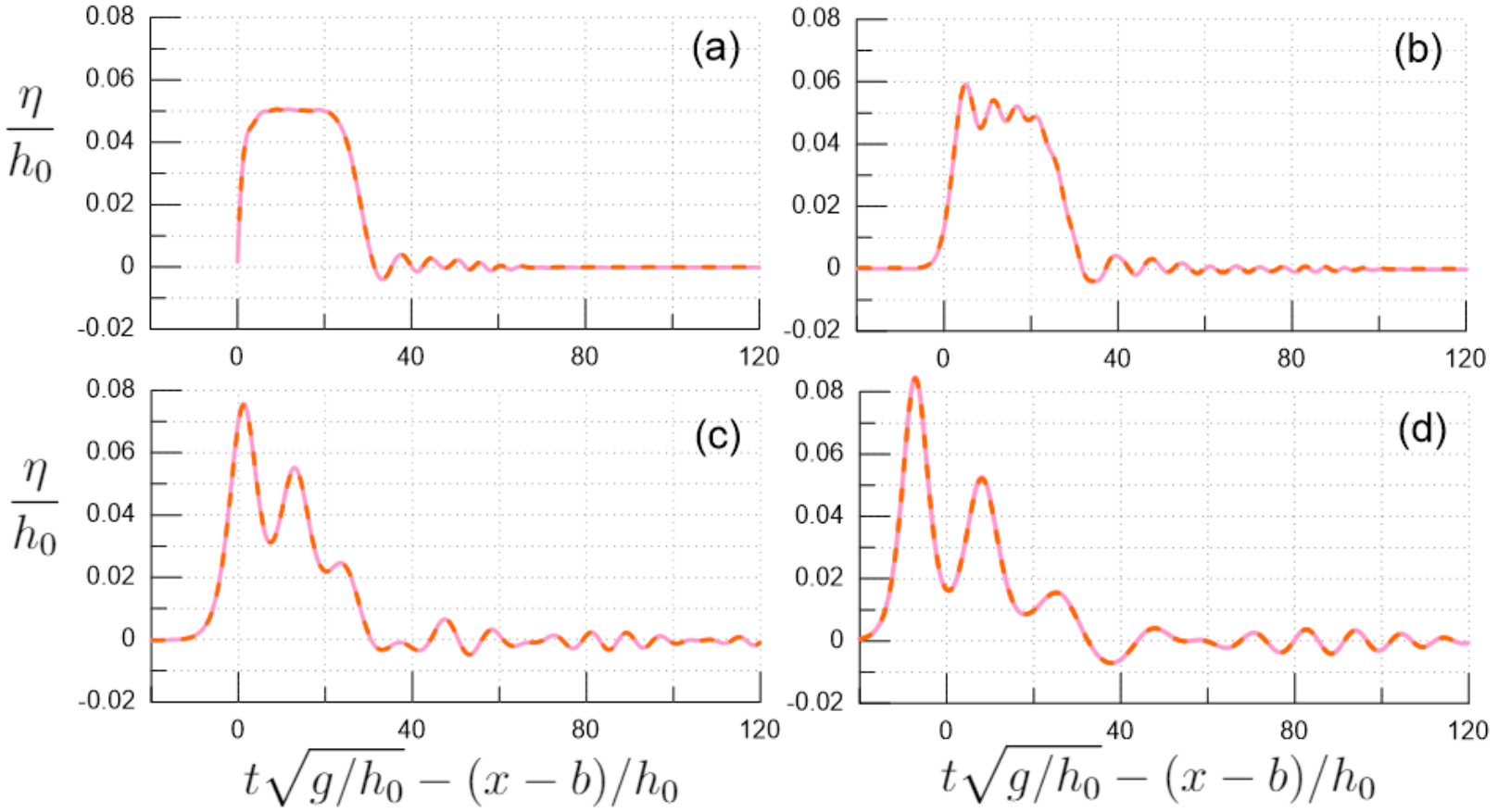

Figure A.2. Time series of the free surface elevations obtained in the simulation of the bed up-thrust using the formulation of Wu *et al.* (solid line) and using the RK O(4) (dashed line) at gauges (a)$(x-b)/h_0 = 0$, (b)$(x-b)/h_0 = 20$, (c)$(x-b)/h_0 = 180$ and (d)$(x-b)/h_0 = 400$.

APPENDIX B: THE RESULTS OBTAINED IN THE SIMULATION OF HAMMACK'S EXPERIMENTS USING THE SLD OF THE FREE SURFACE

The case that has an undisturbed water level $h_0 = 0.05\,m$ is modeled using the SLD of the free surface. The horizontal spacing on the free surface and the bottom is equal to $dx = 0.05m$, while the vertical spacing on both ends of the wave flume is set to $dz = 0.005\,m$. The time increament dt is set as $0.001\,s$. The results attained using the SLD of the free surface are given in Figures B.1 and B.2 for the impulsive bed down-thrust and the impulsive bed upthrust, respectively.

The results obtained using the RK O(4) for the integration of the free surface in FLD are also presented in Figures B.1 and B.2. The utilized undisturbed water depth, the nodal spacings and the time-step are same as presented in the subsections 5.1.1 and 5.1.2. The results obtained using the SLD of the free surface are in perfect agreement with those of the FLD of the free surface.

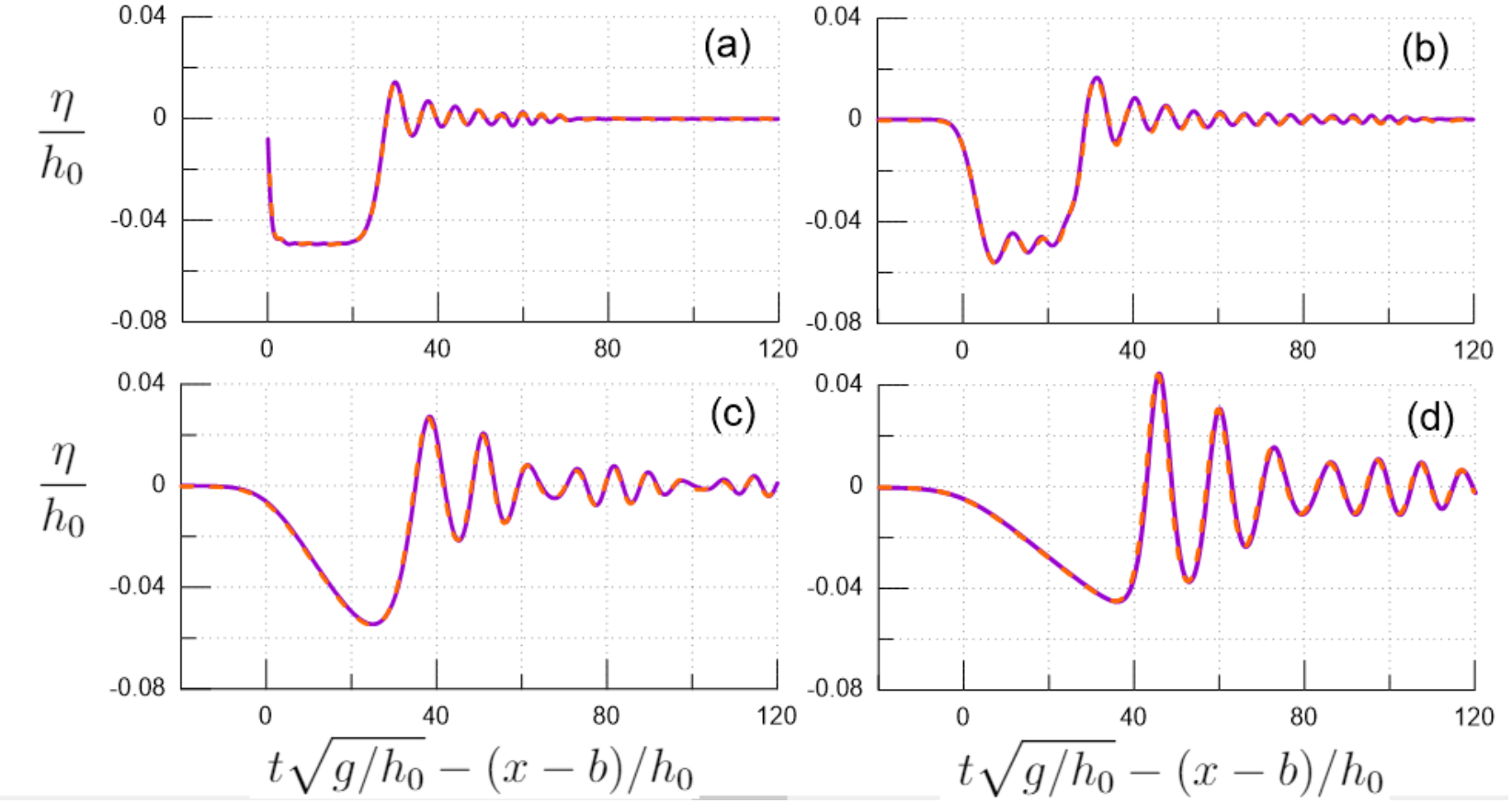

Figure B.1. Time series of the free surface elevations obtained in the simulation of the bed down-thrust using the SLD of the free surface (AB(4))(solid line) and using the FLD of the free surface (RK(4)) (dashed line) at gauges (a)$(x-b)/h_0 = 0$, (b)$(x-b)/h_0 = 20$, (c)$(x-b)/h_0 = 180$ and (d)$(x-b)/h_0 = 400$.

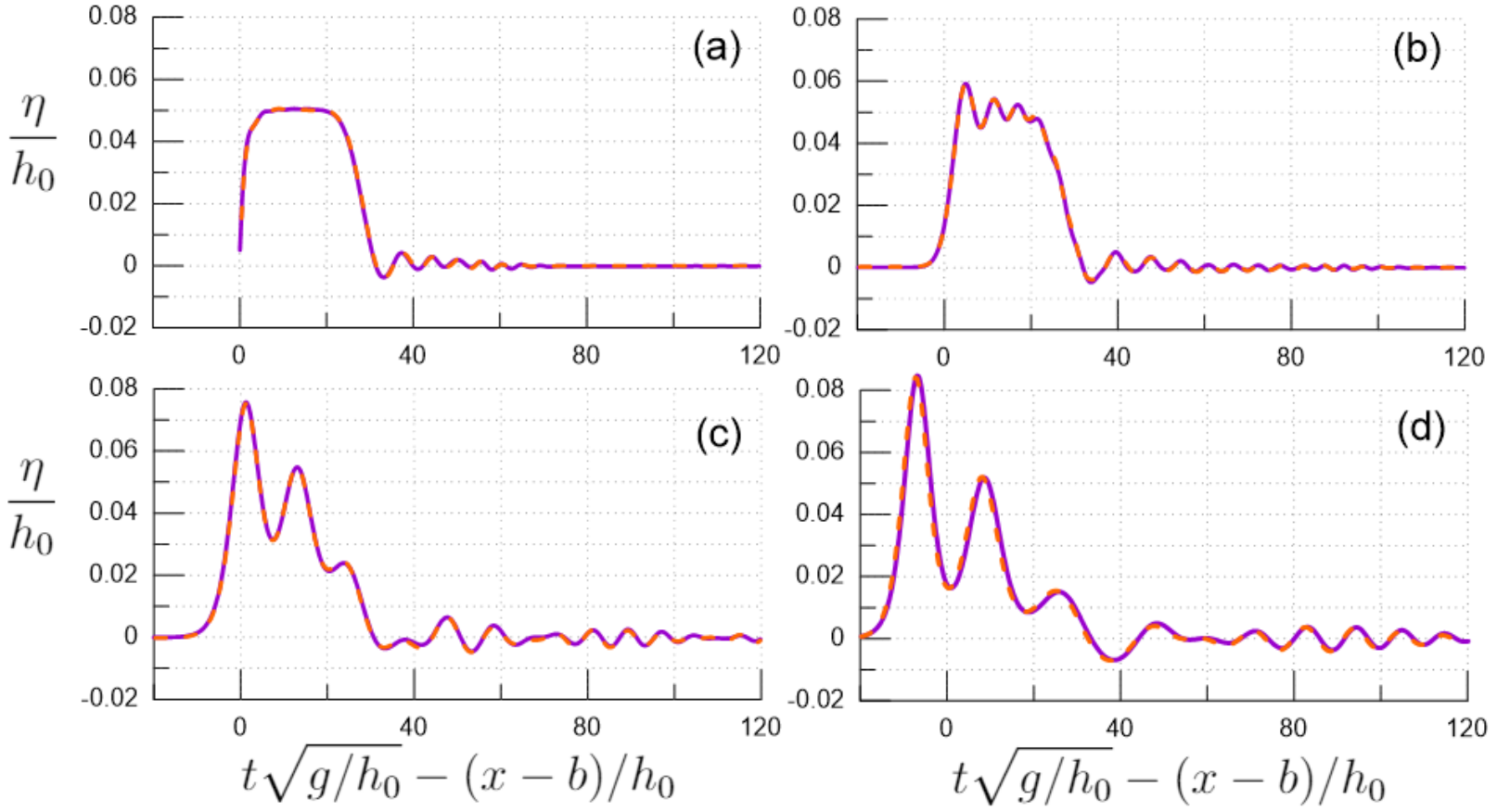

Figure B.2. Time series of the free surface elevations obtained in the simulation of the bed up-thrust using the SLD of the free surface (AB(4))(solid line) and using the FLD of the free surface (RK(4)) (dashed line) at gauges (a)$(x-b)/h_0 = 0$, (b)$(x-b)/h_0 = 20$, (c)$(x-b)/h_0 = 180$ and (d)$(x-b)/h_0 = 400$.

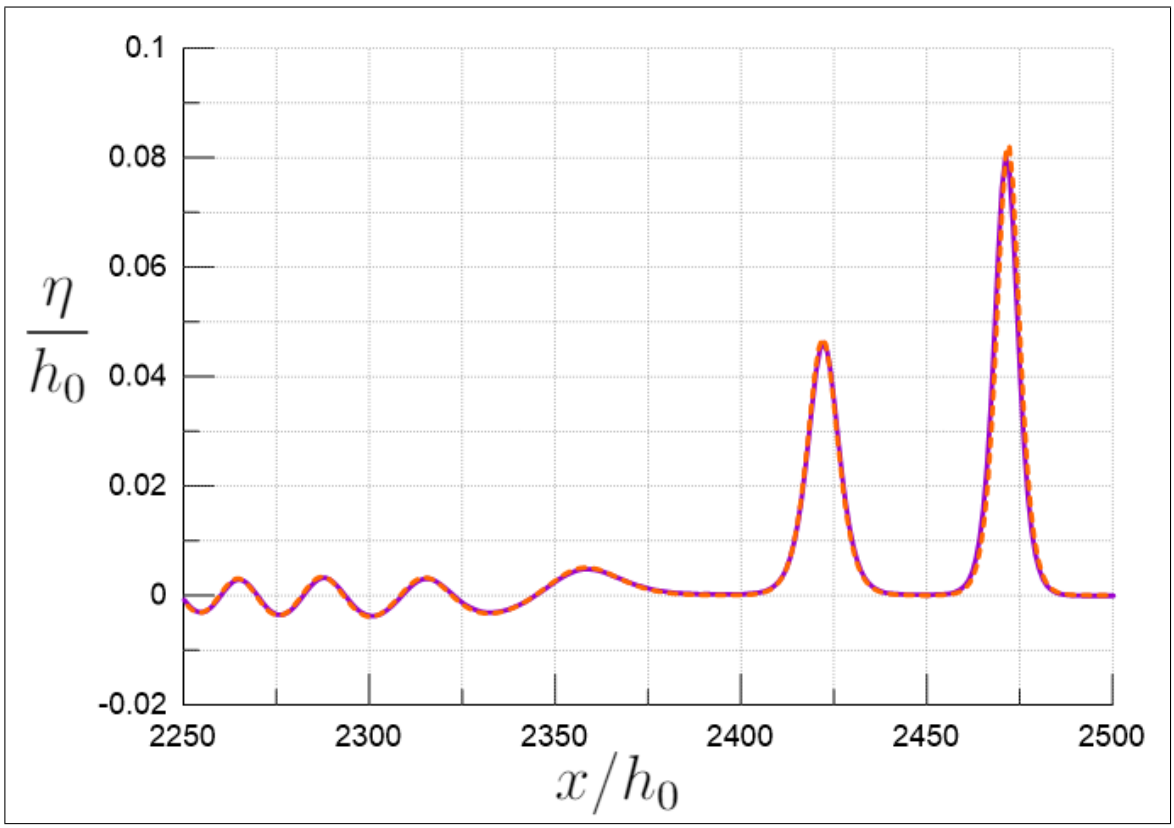

Figure B.3. The free surface profiles obtained in the simulation of the bed up-thrust using the SLD of the free surface (AB(4))(solid line) and using the SLD of the free surface (RK(4))(dashed line) at $t\sqrt{g/h_0} = 2375$.

APPENDIX C: THE UTILIZATION OF THE GAUSSIAN RBF

C.1. Interpolation of the Free Surface Elevation at the Gauges

The free surface collocation nodes are free to move in x-direction while using the FLD of the free surface, therefore the RBF interpolation in 1D is used to determine the free surface elevations at the gauges. The Gaussian RBF is preferred for the interpolation, because its effective radius can be controlled by the shape parameter. The Gaussian RBF is given as

$$f = \exp(-r^2/\sigma^2) \tag{C.1}$$

where the σ is the shape parameter which determines the range of influence of the Gaussian RBF [64]. In the numerical model, the shape parameter is chosen to be three times the initial nodal spacing of the free surface collocation nodes. The vertical position of the ith collocation node can be written as the linear combination of M Gaussian RBFs,

$$z_i = \sum_{j=1}^{M} \alpha_j \exp(-r_{ij}^2/\sigma^2) \qquad \text{where} \quad r = \sqrt{(x_i - x_j)^2} \tag{C.2}$$

or in open form,

$$f_{i1}\alpha_1 \;+\; f_{i2}\alpha_2 \;+\; f_{i3}\alpha_3 \;+\; \cdots \;+\; f_{iM}\alpha_M \;= z_i \tag{C.3}$$

In the present model, the number of RBF centers is chosen equal to the number of the free surface collocation nodes N_{FS}. When Equation C.3 is applied for all free surface collocation nodes, the following linear system of equations can be obtained,

$$\mathbf{F}_{N_{FS}\times N_{FS}}\, \boldsymbol{\alpha}_{N_{FS}\times 1} = \mathbf{z}_{N_{FS}\times 1} \tag{C.4}$$

where $\mathbf{z}$ is the vector whose elements are z-coordinates of the collocation nodes and the $\mathbf{F}$ is the coefficient matrix. After solving Equation C.4 for the coefficient vector $\boldsymbol{\alpha}$, the free surface elevation at the gauge located at x_{gauge} can be found by

$$\eta_{gauge} = \sum_{j=1}^{N_{FS}} \exp\big(-(x_{gauge} - x_j)/\sigma^2\big)\alpha_j \tag{C.5}$$

As the Gaussian RBF is non-singular, the RBF centers could be chosen same as the free surface collocation nodes in the numerical model. The derivative of the Gaussian RBF can be found using the relation given in Equation 4.4 as,

$$f^x = -\frac{2(x - x_j)}{\sigma^2} f = -\frac{2(x - x_j)}{\sigma^2} \exp(-r^2/\sigma^2) \tag{C.6}$$

Thus, $\partial\eta/\partial x$ at the ith collocation node can be determined using

$$\left(\frac{\partial \eta}{\partial x}\right)_i = -\sum_{j=1}^{N_{FS}} \alpha_j \frac{2(x_i - x_j)}{\sigma^2} \exp(-r^2/\sigma^2) \tag{C.7}$$

where

$$r = \sqrt{(x_i - x_j)^2}$$

C.2. Finding the Spatial Derivative of the Water Depth

The water depth at the ith collocation node can be written as in the previous section,

$$h_i = \sum_{j=1}^{M} \alpha_j \exp(-r_{ij}^2/\sigma^2) \qquad \text{where} \quad r = \sqrt{(x_i - x_j)^2} \tag{C.8}$$

The linear system of equations is obtained as

$$\mathbf{F}_{N_B \times N_B}\, \boldsymbol{\alpha}_{N_B \times 1} = \mathbf{h}_{N_B \times 1} \tag{C.9}$$

where N_B is the number of the bottom collocation nodes and the RBF centers are the same as the collocation nodes. The RHS vector $\mathbf{h}$ has elements that are the water depths at the collocation nodes. When the spatial derivative of the water depth function changes rapidly like in the vicinity of the corners of the sliding semi-ellipse on a sloping bottom, the shape parameter is selected to be equal to the nodal spacing of the bottom collocation nodes. After obtaining coefficient vector $\boldsymbol{\alpha}$, the bottom slope $\partial h/\partial x$ at the ith collocation node can be found using

$$\left(\frac{\partial h}{\partial x}\right)_i = -\sum_{j=1}^{N_B} \alpha_j \frac{2(x_i - x_j)}{\sigma^2} \exp(-r^2/\sigma^2) \tag{C.10}$$

where

$$r = \sqrt{(x_i - x_j)^2}$$

APPENDIX D: THE FIGURES FROM OTHER STUDIES

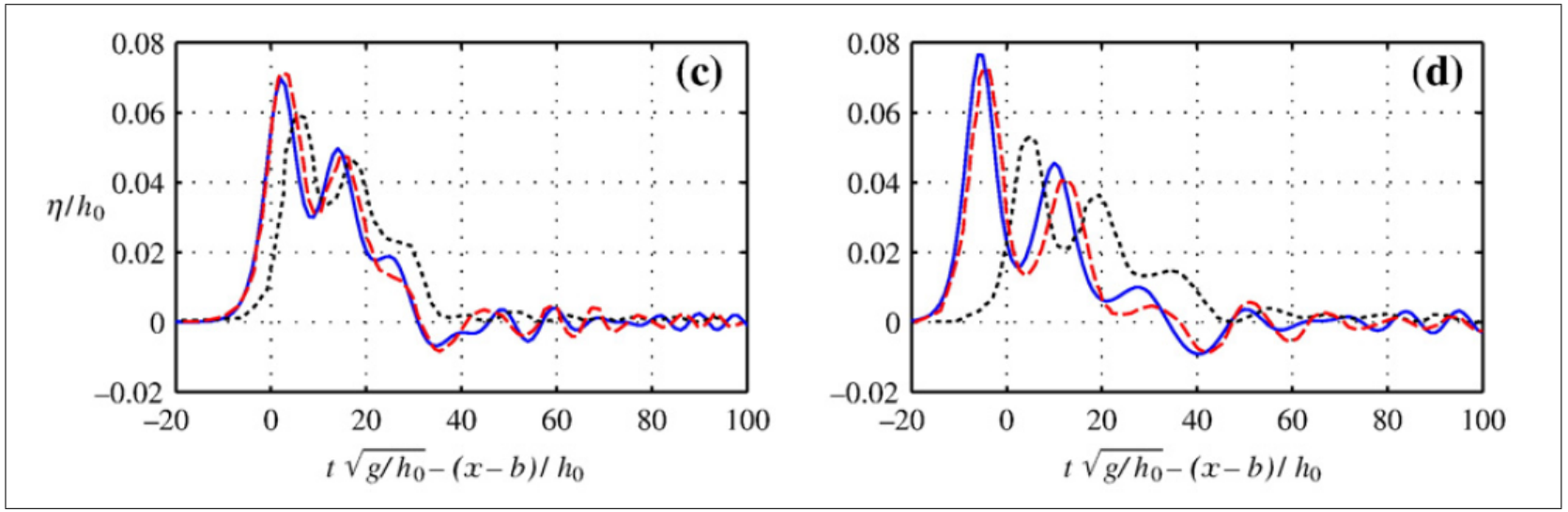

Figure D.1. The time series of the free surface elevations from the Boussinesq-type model of Fuhrman and Madsen (solid line), from the PBBM model of Hammack (dashed line) and from the measurements taken in the experiment of Hammack (dotted line) for the impulsive positive bed up-thrust [43] at (c) $(x-b)/h_0 = 180$ and (d)$(x-b)/h_0 = 400$.

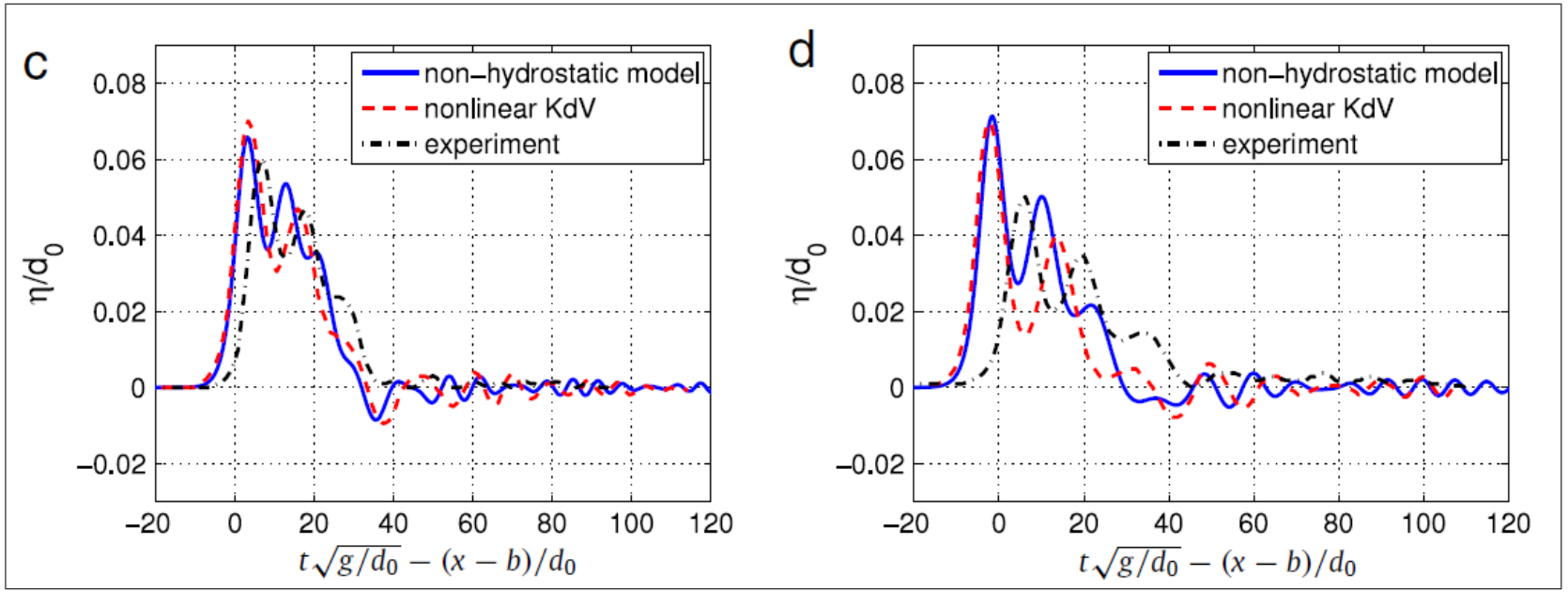

Figure D.2. The time series of the free surface elevations from the model of Tijandra and Pudjaprasetya (solid line), from the PBBM model of Hammack (dashed line) and from the measurements taken in the experiment of Hammack (dashed and dotted line) for the impulsive positive bed up-thrust [45] at (c) $(x-b)/h_0 = 180$ and (d)$(x-b)/h_0 = 400$.

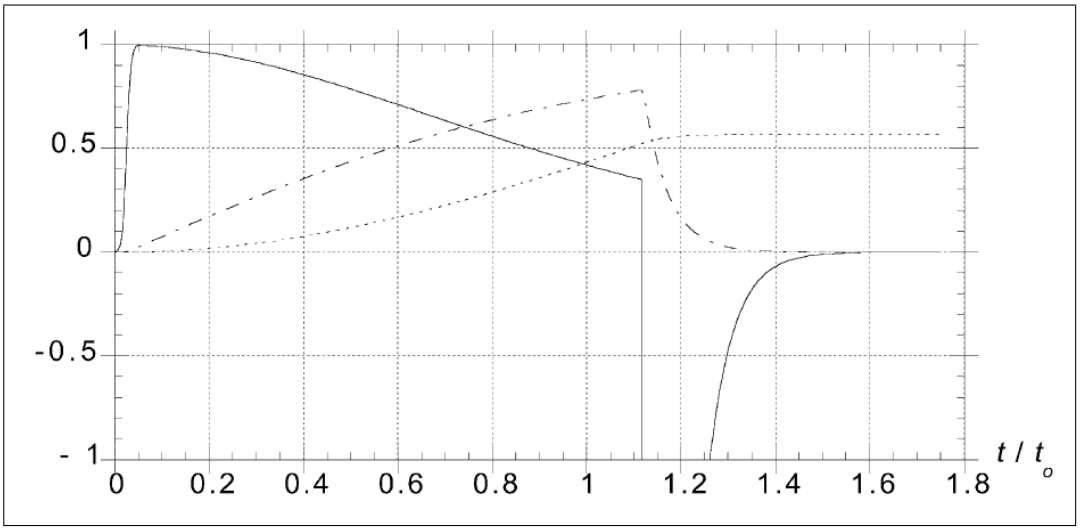

Figure D.3. The non-dimensional landslide kinematics given by Grilli *et al.* [39] for the experiment of Watts *et al.* [38]: S/S_0 (dotted),$\dot{S}/u_t$ (dashed and dotted) and $\ddot{S}/a_0$ (solid) [39]

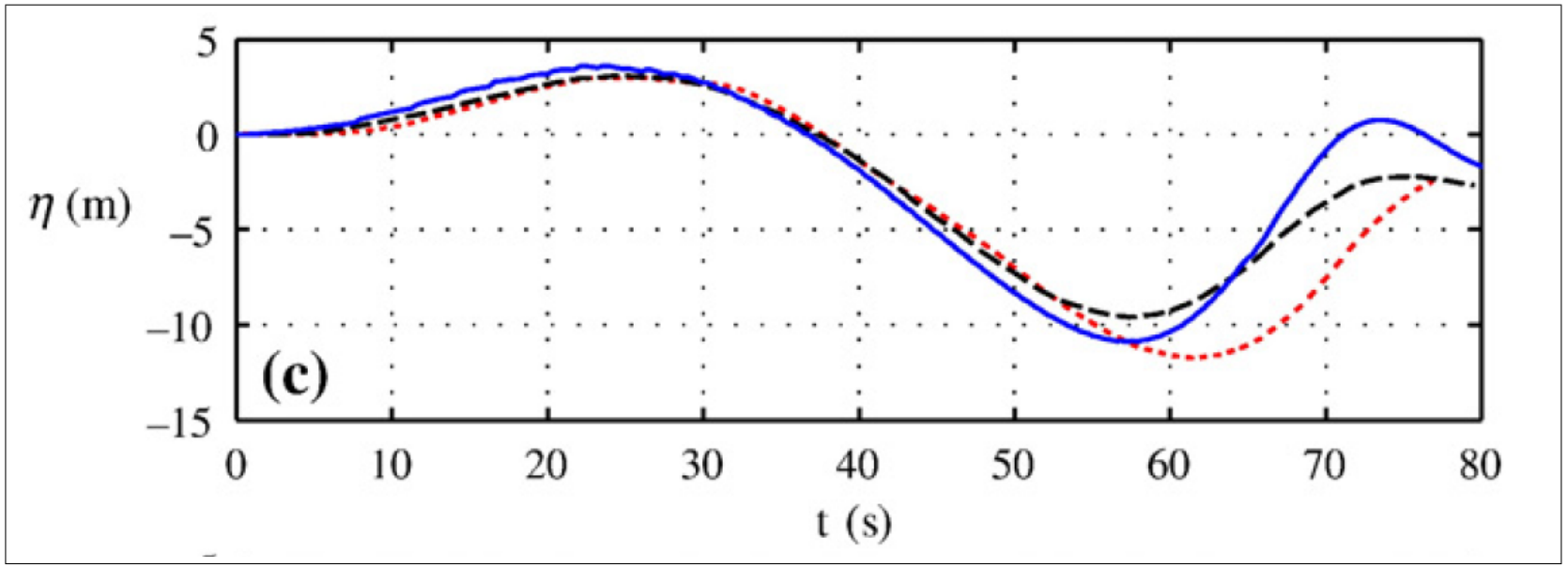

Figure D.4. The time series of the free surface elevations from the Boussinesq-type model of Fuhrman and Madsen (solid line), from the BEM model of Grilli *et al.* and from the measurements taken in the experiment of Watts *et al.* [43] at $x = 1775m$.